2018

Low-volume liquid handling and transport microsystems with applications to microbiology and point-of-care diagnostics

Taejoon Kong
Iowa State University

Low-volume liquid handling and transport microsystems with applications to microbiology and point-of-care diagnostics

by

Taejoon Kong

A dissertation submitted to the graduate faculty

in partial fulfillment of the requirements for the degree of

DOCTOR OF PHILOSOPHY

Major: Electrical Engineering

Program of Study Committee:
Santosh Pandey, Major Professor
Jaeyoun Kim
Long Que
Meng Lu
Jiming Song

The student author, whose presentation of the scholarship herein was approved by the program of study committee, is solely responsible for the content of this dissertation. The Graduate College will ensure this dissertation is globally accessible and will not permit alterations after a degree is conferred.

Iowa State University

Ames, Iowa

2018

TABLE OF CONTENTS

Page

LIST OF FIGURES

Page

LIST OF TABLES

Page

ACKNOWLEDGMENTS

First of all, I would like to express my sincerest gratitude to my advisor Professor Santosh Pandey for giving me wonderful guidance and support over the past five years. I appreciate his patience, enthusiasm, consideration, understanding, and dedication to my career. I feel I am very fortunate to have him as my advisor and I would like to attribute most of my research achievements to him. I would like to thank my Ph.D. committee members: Dr. Jaeyoun Kim, Dr. Long Que, Dr. Meng Lu, and Dr. Jiming Song for their suggestions regarding my research. Their insightful comments and constructive feedback have helped with my success.

In addition, I would like to thank my fellow graduate students, collaborators, research technicians and our undergraduate student workers at Iowa State University for their contribution to this research. I learnt numerous experimental techniques from Dr. Greg Phillips, Dr. Greg Tylka, and Nicholas Backes. I would like to especially thank Upender Kalwa and Chris Legner, for their help and support. I also am thankful to my friends and colleagues: Dr. Jungwook Paek, Dr. Youngwon Kim, Dr. Kyuho Lee, and Dr. Zach Njus. I would also like to extend my thanks to my friend, Minwoo Shin, for always being there for me throughout this adventure.

Last but not least, I would like to thank my parents with all my heart for their unwavering support, selfless sacrifices, and continuous love. If not for them this opportunity never would have been possible for me. This research was partially funded by Defense Threat Reduction Agency (HDTRA1-15-1-0053) and U.S. National Science Foundation (NSF IDBR-1556370). Permission for use in my dissertation has been granted by *Lab on a Chip*.

ABSTRACT

The healthcare industry is witnessing a growing demand for portable, field-ready diagnostic platforms which can test a number of disease biomarkers from collected samples such as saliva, urine, and blood. To democratize such diagnostic platforms, it is beneficial to employ techniques that are power efficient and low-cost while maintaining the standards of accuracy and throughput. With these goals, novel methods are presented here for liquid handling and transport with applications in point-of-care diagnostics and microbiology. Specifically, a motorized actuation system is developed to manipulate discrete liquid droplets and perform operations such as dispensing, movement, mixing, merging, and disposal in a remote-controlled manner. A paper-based cantilever device is demonstrated to enable the flow of fluids between two or more paper strips that can be incorporated in lateral flow diagnostic assays. Both the abovementioned platforms have been used as colorimetric assays to detect the presence of common analytes in fluids. In addition, a fluid-flow chip design is illustrated where the chip is fabricated from double-sided tape and agarose membrane, along with options to create and maintain gradients of chemicals over long time periods. The microfluidic chip has been used to grow colonies of *E. coli* bacteria and observe their phenotypic changes in response to the applied antibiotics. The microfluidic chip provided a suitable platform to test the efficacy of gene-editing experiments by monitoring the morphological changes in the bacterial cells. Each of the presented methods is tailored for a specific biological experiment, and thus highlight the importance of adapting and customizing engineering technologies for applied research.

CHAPTER 1.

INTRODUCTION

Research Motivations

In this thesis, the research focused on the development of low-volume and user-friendly liquid handling and transport microsystems for lab-on-a-chip applications, specifically for droplet microfluidics, paper-based point-of-care diagnostics and bacterial microbiology. Liquid handling and transport is a primary objective in several chemical and biological experiments where there is scope to improve the throughput and speed of various operations. An example of such an instrument is the robotic micro-pipetting system that can automatically load and dispense microscale volumes of reagents with great spatial and temporal resolution. To obtain the reliable result, the accuracy and precision of micro-volume liquid handling are crucial while performing the experiments. Today, there is significant thrust towards laboratory automation that can provide better efficiency, fewer errors, fast response time, and higher throughput. For this reason, microfluidics has gained visibility where microscale devices can be fabricated and applied to emerging areas of healthcare such as point-of-care diagnostics and microbiology.

However, most robotic-based liquid handling systems are cost prohibitive and has very limited scope of customization. On the other hand, microfluidic-based liquid handling systems are highly customizable but are difficult for mass manufacturing. Microfluidics still involves considerable complex fabrication steps and skilled personnel to operate the lab-on-a-chip system. The high cost barrier makes it problematic for microfluidics to be deployed in field settings or low resource settings. Thus, there is genuine need for liquid handling systems that

are cost-effective, easy-to-use, and easy-to-fabricate while embracing the performance benefits of conventional systems.

In order to build innovative technologies for biological applications, it is worthwhile to explore the novelty of proposed systems both from the perspectives of engineering and life sciences. Through our collaboration with biologists, we investigated experimental procedures in the veterinary microbiology laboratory in ISU to recognize the specific steps where the need for a novel liquid handling system could be rationalized. Besides, through designing conventional microfluidic systems that employed silicon fabrication steps, we devised alternative ways to fabricate devices from low-cost materials and without the use of micromachining steps. This thesis discusses new liquid handling systems that have definite benefits over conventional systems, along with testing their performance using target analytes and bacterial micro-organisms.

Literature Review

In bioengineering, the precise control of liquid handling is a crucial step for point-of-care diagnostics and high-throughput cell analysis [1,2]. Recently, a number of low volume liquid handling device have been developed and commercialized in many clinical laboratories [1]. In this section, various conventional liquid handling microsystems are reviewed to understand the strengths and shortcomings of existing techniques.

Recently, there is a growing interest in droplet microfluidics where discrete droplets are employed to conduct a large range of experiments in chemistry and biology such as polymerase chain reaction [3], chemical and enzymatic reactions, immunoassays [4-7], DNA sequencing [8-10], and cell biology [11-14]. Experiments based on droplet microfluidics require on-chip forces to move droplets in definite paths to accomplish a series of events. The existing methods of droplet transport can be classified as two broad groups: electrical and non-

electrical methods. The electrical or electrowetting-on-dielectric (EWOD) method uses the electric field to modify the surface tension between the liquid droplet and the substrate to manipulate the movement of discrete droplets on the hydrophobic surface [15-18]. This method is commonly used in digital microfluidic platform to perform the droplet operations such as transporting, mixing, dispensing, merging and splitting. A bottom substrate contains the array of actuation electrodes and hydrophobic dielectric layer [15]. Electro-wetting requires a very high voltage of the order of 100 V and control circuitry to digitize and apply the voltage on specific electrodes (Figure 1.1).

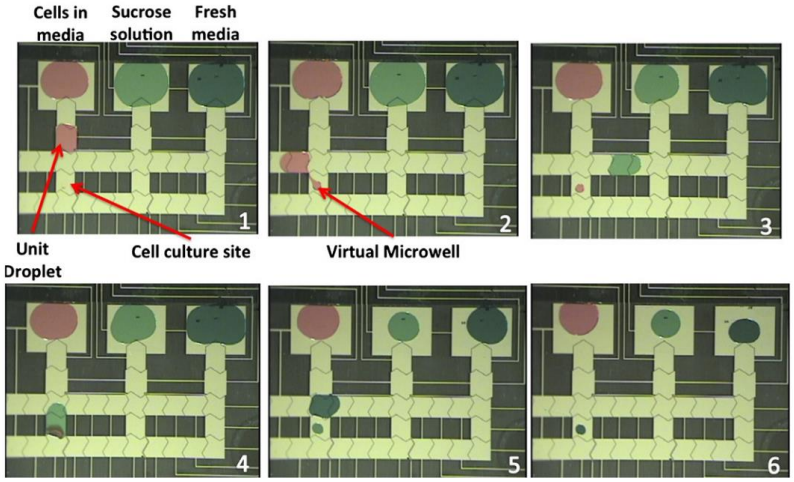

Figure 1.1 Pictures of typical experiment steps of digital microfluidic device ([15]).

To prevent an excessive power consumption and detrimental effects on the microorganisms or biomolecules within the liquid droplets, non-electrical methods have been investigated using the magnetic, mechanical acoustic or gravitational forces to control the droplet movement [19-23]. The 'textured ratchet' micro structures were fabricated in the silicon substrate and an electrical motor vibrated the entire system (Figure 1.2). The droplet repeated the advancing and receding motion, which caused it to experience the differential wetting and to be transported in a pre-specified direction.

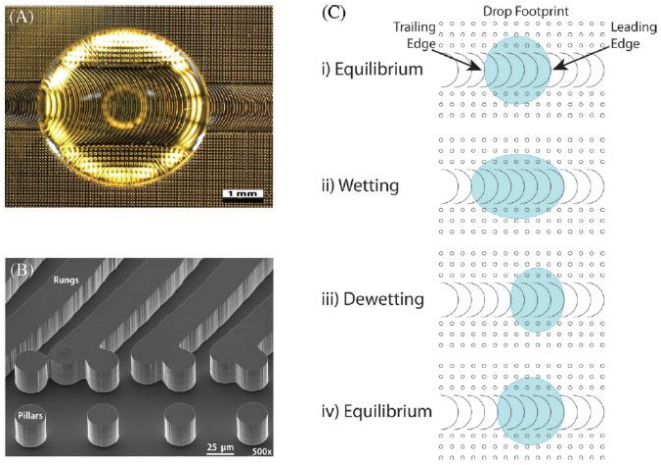

Figure 1.2 The principle of texture ratchet microfluidic device. (a) Snapshot of 20 µL volume droplet positioned on the patterned silicon wafer (b) The pattern of texture ratchet viewed with a scanning electron microscope (c) Different steps involved in transporting droplet on the ratchet subjected to vibrations ([19]).

The droplet movement was also achieved by employing shallow superhydrophobic grooves on zinc or silicon substrates [19].

Besides the use of hydrophobic substrates to manipulate droplets, chromatography paper has also been proposed as a low-cost, disposable substrate for liquid manipulation. Paper-based devices hold promise for a range of diagnostic tests, particularly in resource-limited regions of the world [24, 25]. The paper-based lateral flow assay or the dipstick is the most common technique [26] for rapid diagnostic assays in healthcare [27], environmental monitoring [28], veterinary medicine [29] and food safety [30]. While single tests can easily be handled with simple paper substrates coated with specific biomarkers, it is challenging to conduct diagnostic tests where a sequence of steps are needed to be performed. In such sequential tests, there is a need to regulate and switch the fluid flow in the multiple channels to control the delay time, so that a fluid can dwell in a certain location for a chemical reaction before moves to another region [31-33]. One interesting approach to create delays in fluid flow within paper substrates is by incorporating dissolvable chemicals [34]. The delay time of fluid

flow can be regulated by using a dissolvable chemical as a bridge which connects and disconnects the two paper channels. The dissolvable sugar bridge delivered specific range of liquid volumes and dissolves to the off-switches, which stops the fluid flow permanently [34]. Another method to control the fluid flow involved the incorporation of magnetized paper cantilever valve which is driven by an external electromagnet. The electromagnet circuit was triggered by an ionic resistor, which pulls the magnet cantilever to connect the two paper channels (Figure 1.3). Other types of switches in paper microfluidics have been demonstrated that use folding cards, 3D slip pad, or paper-based push buttons [36-38].

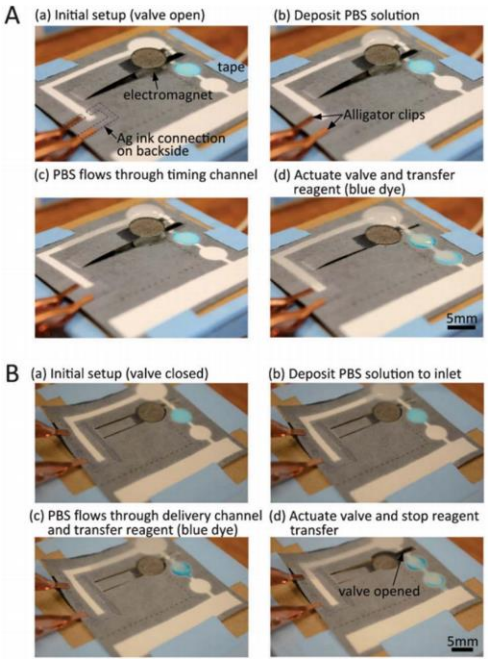

Figure 1.3 The operation of magnetized paper cantilever valves. (a) a paper channel is disconnected initially (b) a paper channel is connected initially ([35]).

The abovementioned review covered the general methods of manipulating droplets which has then been applied to actual chemical and biological experiments. One such application is in the field of microbiology where liquid droplets can be used to incubate bacteria and test their behavior in response to various antibiotics. The ability to characterize the efficacy of antibiotics on contaminated samples in a rapid manner is of utmost importance to the

healthcare industry. According to public health and awareness organizations, antimicrobial resistance (AMR) is an increasing threat to global public safety [39]. In general, antimicrobial resistance is the ability of microbes to keep growing, and not being incapacitated, in the presence of the antibiotics. The emergence of resistance in nature is an inevitable phenomenon [40], and the mere observation of acquired resistance helps researchers to identify modes of resistance and find ways to combat the emergence of resistance researchers. As the scientific community is unraveling mechanisms by which bacterial cells acquire resistance and developing new toolbox to edit related genes to inhibit the propagation of antimicrobial resistance, the technologies for observing bacterial behavior need to evolve at a greater pace [41-44]. Plate assays are available to detect antimicrobial resistance in bacterial colonies and measure the minimum inhibitory concentration of bacterial cells, which require considerably long time periods with significant amount of chemical and biological resources [45-46]. To complement plate assays, several microfluidic systems have been introduced to perform tests on antibiotic susceptibility or resistance. To obtain the time-lapse image of single cell division, microfluidic devices have been used to immobilize the bacterial cell and to provide drug solutions [47-50]. The agarose-based PDMS microfluidic device is introduced to perform antibiotic susceptibility test (Figure 1.4). The bacterial cells were mixed with liquid agarose solutions and the mixtures were injected into the microfluidic chip. Antibiotic solutions were supplied through the fluidic channel and slowly diffused into the agarose membrane. Then, bacterial growth was monitored under the microscope to observe the abnormal behavior.

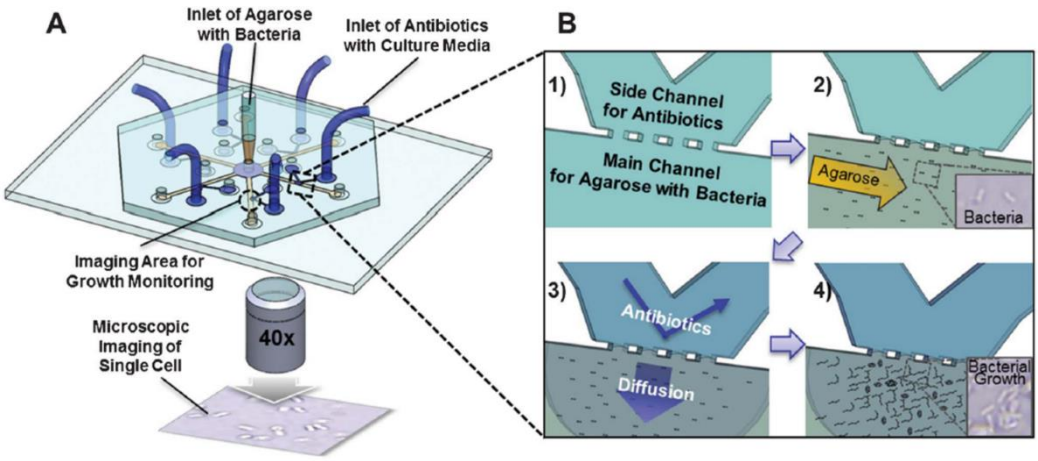

Figure 1.4 A schematic image of rapid antibiotic susceptibility test system. (a) The multichannel PDMS microfluidic device contains the inlet of agarose solution and several inlets of antibiotic solution. (b) The procedure to determine antibiotic susceptibility of bacterial cells employing microfluidic agarose channels ([50]).

Dissertation Organization

This thesis presents novel low-volume liquid handling and transport microsystems that can be used as assays for portable diagnostics and antimicrobial resistance testing.

Chapter 2 discusses a motorized actuation system to remotely manipulate the multiple droplets simultaneously on the plastic sheet. Unlike conventional liquid handling systems, our device can perform the various droplet operations without requiring any external equipment which increases the operational costs. The actuation system, powered by two stepper motors, can control the movement of multiple droplets by manipulating the two axis rotation of the plastic sheet. The mathematical model is developed to characterize the droplet movement based upon the physical forces and system parameters. Our system is employed to measure the glucose concentration in sheep serum using a colorimetric enzymatic test. This chapter is modified from the journal article, “Motorized actuation system to perform droplet operations on printed plastic sheets” published in Lab on a Chip, 16, 1861-1872, 2016.

Chapter 3 describes a method to switch and regulate the liquid transport between multiple layers of paper for use in point-of-care diagnostic assays. Our origami-based flow switch has benefits such as easy preparation steps, very fast actuator response time, different switch configurations, and ability to test multiple actuators without any external instrumentation. We showed various reconfigurable switch operations by wetting the folded area of the paper-based actuator. We developed a colorimetric assay to detect the presence of glucose, protein and nitrite from artificial saliva simultaneously. Delay timer strip is used in the assay to automatically activate multiple actuators and to observe distinct color changes produced from the chemical reactions. This chapter is modified from the journal article, "A fast, reconfigurable flow switch for paper microfluidics based on selective wetting of folded paper actuator strips" published in Lab on a Chip, 17, 3621-3633, 2017.

Chapter 4 demonstrates a non-polymeric microfluidic device to observe the behavior of bacterial cells exposed to the antibiotic solution and to visualize changes in their morphology as modulated by gene expression. The device can continuously supply the solutions and generate the chemical gradients in a thin layer of agarose membrane where bacterial cells are cultured. An autofocusing feature is integrated with the imaging system to enable the capture of high quality images of bacterial growth for prolonged time periods. To show the potential of the device for microbiology experiments, we conducted tests on antibiotic susceptibility to uncover phenotypes in *E. coli* that result from incremental expression of specific genes.

Chapter 5 summarizes the key conclusions of the thesis.

References

1 D. Mark, S. Haeberle, G. Roth, F. Stetten and R. Zengerle, Chem. Soc. Rev., 2010, 39, 1153-1182.

2 G. A. Posthuma-Trumpie, J. Korf and A. van Amerongen, Anal. Bioanal. Chem., 2009, 393, 569-582.

3 Y. H. Chang, G. B. Lee, F. C. Huang, Y. Y. Chen and J. L. Lin, Biomedical Microdevices, 2006, 8, 215-225.

4 D. Chatterjee, B. Hetayothin, A. R. Wheeler, D. J. Kong and R. L. Garrell, Lab Chip, 2006, 6, 199-206.

5 T. Taniguchi, T. Torii and T. Higuchi, Lab Chip, 2002, 2, 19-23.

6. V. Srinivasan, V. K. Pamula and R. B. Fair, Anal. Chim. Acta., 2004, 507, 145-150.

7 V. Srinivasan, V. K. Pamula and R. B. Fair, Lab Chip, 2004, 4, 310-315.

8 M. Abdelgawad, S. L. Freire, H. Yang and A. R. Wheeler, Lab Chip, 2008, 8, 672-677.

9 R. Sista, Z. Hua, P. Thwar, A. Sudarsan, V. Srinivasan, A. Eckhardt, M. Pollack and V. Pamula, Lab Chip, 2008, 8, 898-906.

10 Y. J. Liu, D. J. Yao, H.C. Lin, W. Y. Chang and H. Y. Chang, J. Micromech. Microeng., 2008, 18, 045017.

11 I. Barbulovic-Nad, H. Yang, P. S. Park and A. R. Wheeler, Lab Chip, 2008, 8, 519-526.

12 S. H. Au, S. C. C. Shih and A. R. Wheeler, Biomed. Microdevices, 2011, 13, 14-50.

13 S. K. Fan, P. W. Huang, T. T. Wang and Y. H. Peng, Lab Chip, 2008, 8, 1325-1331.

14 S. Park, P. A. Wijethunga, H. Moon and B. Han, Lab Chip, 2011, 11, 2212-2221.

15 S. C. C. Shih, I. Barbulovic-Nad, X. Yang, R. Fobel and A. R. Wheeler, Biosensors and Bioelectronics, 2013, 42, 314-320.

16 M. J. Jebrail, M. S. Bartsch and K. D. Patel, Lab Chip, 2012, 12, 2452-2463.

17 K. Choi, A. H. C. Ng, R. Fobel and A. R. Wheeler, Annu. Rev. Anal. Chem., 2012, 5, 413-440.

18 W. C. Nelson and C. –J. Kim, J. Adhes. Sci. Technol., 2012, 26, 1747-1771.

19 T. A. Duncombe, E. Y. Erdem, A. Shastry, R. Baskaran and K. F. Bohringer, Adv. Mater., 2012, 24, 1545-1550.

20 A. Ghosh, R. Ganguly, T. M. Schutzius and C. M. Megaridis, Lab Chip, 2014, 14, 1538-1550.

21 J. Seo, S. Lee, J. Lee and T. Lee, ACS Appl. Mater. Interfaces, 2011, 3, 4722-4729.

22 Z. Wang and J. Zhe, Lab Chip, 2011, 11, 1280-1285.

23 H. Mertaniemi, V. Jokinen, L. Sainiemi, S. Franssila, A. Marmur, O. Ikkala and R. H. Ras, Adv. Mater., 2011, 23, 2911-2914.

24 World Urbanization Prospects – The 2011 Revision, Department of Economic and Social Affairs, Population Division, UN, New York, 2012.

25 K. Tontisirin, G. Nantel and L. Bhattacharjee, Proc. Nutr. Soc., 2002, 61, 243-250.

26 A. H. Free, E. C. Adams, M. L. Kercher, H. M. Free and M. H. Cook, Clin. Chem., 1957, 3, 163-168.

27 T. Acharya, A. S. Daar, E. Dowdeswell, P. A. Singer and H. Thorsteinsdottir, Genomics and Global Health, University of Toronto Joint Centre for Bioethics, Toronto, Ontario, Canada, 2004.

28 Water Quality for Ecosystem and Human Health, GEMS/Water Programme Office, UN, Burlington, Ontario, Canada, 2008.

29 E. A. M. Bokkers, Farming for Health: Green-Care Farming Across Europe and the United States of America, Springer, 2006, 13, pp. 31–41.

30 Global Strategy for Food Safety: Safer Food for Better Health, F. S. Department, Food Safety Department, WHO, Geneva, Switzerland, 2002.

31 X. Li, J. Tian, T. Nguyen and W. Shen, Anal. Chem., 2008, 80(23), 9131–9134.

32 E. Fu and C. Downs, Lab chip, 2017, 17, 614-628.

33 B. J. Toley, J. A. Wang, M. Gupta, J. R. Buser, L. K. Lafleur, B. R. Lutz, E. Fu and P. Yager, Lab Chip, 2015, 15, 1432-1444.

34 B. Lutz, T. Liang, E. Fu, S. Ramachandran, P. Kauffman and P. Yager, Lab Chip, 2013, 13, 2840-2847.

35 X. Li, P. Zwanenburg and X. Liu, Lab Chip, 2013, 13, 2609-2614.

36 E. Fu, T. Liang, P. Spicar-Mihalic, J. Houghtaling, S. Ramachandran and P. Yager, Anal. Chem., 2012, 84, 4574-4579.

37 K. H. Han, J. S. Choi and J. Kwon, Sci. Rep., 2016, 6, 25710.

38 W. Martinez, S. T. Phillips and G. M. Whitesides, Proc. Natl. Acad. Sci. U. S. A., 2008, 105, 19606-19611.

39 A. Towse and P. Sharma, Int. J. Econ. Bus., 2011, 18, 331-350.

40 Z. Liu, N. Banaei and K. Ren, Trends Biotechnol., 2017, 35, 1129-1139.

41 B. B. Aldridge, M. Fernandez-Suarez, D. Heller, V. Ambravaneswaran, D. Irimia, M. Toner and S. M. Fortune, Science, 2012, 335, 100-104.

42 S. Jang, B. Lee, H. Jeong, S. Jin, S. Jang, S. Kim, G. Jung and C. Lee, Lab Chip, 2016, 16, 1909-1916.

43 X. Sun, W. D. Weinlandt, H. Patel, M. Wu and C. J. Hernandez, Lab Chip, 2014, 14, 2491-2498.

44 N. Q. Balaban, J. Merrin, R. Chait, L. Kowalik and S. Leibler, Science 2004, 305, 1622-1625.

45 A. Tirella, M. Marano, F. Vozzi and A. Ahluwalia, Toxicol. In Vitro, 2008, 22, 1957, 1964.

46 N. Ye, J. Qin, W. Shi, X. Liu and B. Lin, Lab Chip, 2007, 7, 1696-1704.

47 I. Wong, S. Atsumi, W. Huang, T. Wu, T. Hanai, M. Lam, P. Tang, J. Yang, J. C. Liao and C. Ho, Lab Chip, 2010, 10, 2710-2719.

48 B. Li, Y. Qiu, A. Glidle, D. McIlvenna, Q. Luo, J. Cooper, H. Shi and H. Yin, Anal. Chem, 2014, 86, 3131-3137.

49 S. L. Faley, M. Copland, D. Wlodkowic, W. Kolch, K. T. Seale, J. P. Wikswo and J. M. Cooper, Lab Chip, 2009, 9, 2659-2664.

50 J. Choi, Y. Jung, J. Kim, S. Kim, Y. Jung, H. Na and S. Kwon, Lab Chip, 2013, 13, 280-287.

CHAPTER 2.

MOTORIZED ACTUATION SYSTEM TO PERFORM DROPLET OPERATIONS ON PRINTED PLASTIC SHEETS

Modified from our journal article, "Motorized actuation system to perform droplet operations on printed plastic sheets", Lab on a Chip, 16, 1861-1872, 2016.
Taejoon Kong,* Riley Brien,* Zach Njus, Upender Kalwa and Santosh Pandey
** Joint first authors*

Abstract

We developed an open microfluidic system to dispense and manipulate discrete droplets on planar plastic sheets. Here, a superhydrophobic material is spray-coated on commercially-available plastic sheets followed by the printing of hydrophilic symbols using an inkjet printer. The patterned plastic sheets are taped to a two-axis tilting platform, powered by stepper motors, that provides mechanical agitation for droplet transport. We demonstrate the following droplet operations: transport of droplets of different sizes, parallel transport of multiple droplets, merging and mixing of multiple droplets, dispensing of smaller droplets from a large droplet or a fluid reservoir, and one-directional transport of droplets. As a proof-of-concept, a colorimetric assay is implemented to measure the glucose concentration in sheep serum. Compared to silicon-based digital microfluidics, we believe that the presented system is appealing for various biological experiments because of the ease of altering design layouts of hydrophilic symbols, relatively faster turnaround time in printing plastic sheets, larger area to accommodate more tests, and lower operational costs by using off-the-shelf products.

Introduction

Generally speaking, microfluidic platforms consist of closed-channel networks where liquid flow is controlled by mechanical, pneumatic or electrokinetic means. Today, with emphasis on higher experimental throughput, microfluidic platforms incorporate several on-chip components (e.g. microvalves, micropumps, and microelectrodes) that increase the complexity in fabricating the different layers, integrating the micro- and macroscale components, and controlling the individual sensing or actuation parts [1,2]. In contrast to closed-channel microfluidics, open microfluidic platforms obviate the use of polymeric channels and continuous liquid flow; thereby relaxing the fabrication process, easing the system integration to fewer components, and promising a cheaper alternative to robotic micro-handling systems [3,4]. In open microfluidics, liquid is dispensed from a reservoir as discretized droplets and transported to desired locations for further manipulation. Typical operations to be performed with discrete droplets may include transport of a single or multiple droplets, merging and mixing of two droplets, incubation and affinity binding within droplets, extraction of solid particles from the liquid phase, and removal of waste droplets [3,5]. These droplet operations are often conceptualized from test tube experiments performed in a wet chemistry laboratory, and the sequence of operations can be easily altered depending on the actual experiment being performed.

The general strategy of producing and actuating discrete droplets on open surfaces relies on methods to modulate the surface tension between the liquid droplet and the solid surface it rests on. The current literature on this topic can be grouped into two categories – methods that employ electrical fields to modulate the wettability of droplets [3-6] and non-

electrical methods that employ mechanical, magnetic, acoustic or gravitational forces to generate directional movement of droplets [7-15].

The electrical or 'electrowetting-on-dielectric' method of droplet actuation has gained popularity in the last decade primarily because of the ease of programmability and portability [16,17]. Here, the conductive liquid droplet sits on patterned electrodes coated with a hydrophobic dielectric layer. An electric field applied to the target electrode increases the contact angle of the droplet placed over it, and thus alters the wettability of the liquid surface to the solid surface. This electrowetting phenomenon can be scaled up to move and control multiple droplets over an array of electrodes, thereby performing any desired sequence of operations including transport, merging, mixing, splitting, and dispensing. Analogous to digital microelectronics where pockets of electrons are transferred between devices (e.g. in charged coupled devices), several groups have realized electrowetting-based 'digital microfluidic platforms' having electrodes of precisely-controlled geometry, on-chip control electronics to energize individual electrodes, and software programs to automate the droplet operations [3,18,19].

Even though the electrowetting method is widely accepted as the gold standard for droplet handling systems, it is restrained by the need for high electrical voltages (in the range of 100 volts to 400 volts) that have unknown effects on the biomolecules or cells within droplets [18-20]. For instance, the electric actuation force can interfere with the adsorption of biomolecules on a surface [21]. Furthermore, droplet actuation is dependent on the conductivity of the droplet and the dielectric properties of the insulating layers (e.g. Teflon and Paralyne) that are expensive for large-scale deposition. Because each electrode is electrically addressed, there are only a finite number of electrodes that can be addressed on a digital

microfluidics platform [22]. To get around this last issue, it has been shown that the electrodes can be optically stimulated (and thereby producing on-demand optical interconnects) by incorporating photoconductive and high dielectric constant layers underneath the Teflon coating [8,23]. Active matrix arrays of Thin Film Transistor (TFTs) have also been demonstrated as an alternate digital microfluidic testbed where many thousand individually addressable electrodes could sense, monitor, and manipulate droplets [22]. Similarly, electrodes can be selectively energized to reposition water volumes in an otherwise liquid paraffin medium to create reconfigurable, continuous-flow microfluidic channels [24]. As these innovations in digital microfluidics technology extend the functionalities to newer arenas of portable diagnostics, much of the fabrication protocol still requires access of industrial-grade microelectronics foundry and is thus limited to select users.

To eliminate some of the limitations of electrowetting mentioned above, non-electrical methods of droplet actuation have been pursued [9,11-15]. In the 'textured ratchet' method, movement of liquid droplets is achieved on textured microstructures (i.e. ratchets) fabricated in silicon or elastomeric substrates [15]. The textured ratchets are placed on a level stage that is vertically vibrated using a linear motor. At the resonant frequency of vertical oscillations, the liquid droplet is able to advance or recede on the textured ratchets. The movement of different droplets can be individually controlled, both in linear and closed tracks, by manipulating the volume and viscosity of droplets. In the 'superhydrophobic tracks' method, shallow grooves are cut in zinc plates or silicon substrates [14]. This is followed by a superhydrophobic coating step by depositing silver and fluorinated thiol surfactant on metal plates or a fluoropolymer on silicon substrates. The produced superhydrophobic tracks are able to confine liquid droplets and guide their movement in trajectories defined by the tracks. In the

'surface acoustic waves (SAW)' method, a high frequency source connected to interdigitated gold electrodes generates acoustic waves that is able to transport fluid droplets on a piezoelectric substrate [25]. Recently, pneumatic suction through a PDMS membrane has been used to activate and move droplets in two dimensions on a superhydrophobic surface without any interference from an external energy (e.g. heat, light, electricity) [21].

While the above non-electrical methods demonstrate that mechanical machining the substrate can passively move droplets, more results are needed to match the level of droplet handling operations achieved in digital microfluidic platforms [3]. To gauge the maturity of digital microfluidics, an exciting example is a multi-functional digital microfluidic cartridge by Advanced Liquid Logic that can perform multiplexed real-time PCR, immunoassays and sample preparation [26]. A group at Sandia National Laboratories has developed a digital microfluidic distribution hub for next generation sequencing that is capable of executing sample preparation protocols and quantitative capillary electrophoresis for size-based quality control of the DNA library [27]. With growing demand of lab on chip systems in medicine, digital microfluidics has been used to extract DNA from whole blood samples [28], quantify the levels of steroid hormones from breast tissue homogenates [29], and screen for metabolic disorders and lysosomal storage diseases from newborn dried blood spots [30-34]. These examples highlight the fact that digital microfluidics is revolutionizing the field of portable medical diagnostics, and any rival technology needs to achieve the basic standards of droplet handling set by digital microfluidics.

In an attempt to emulate the droplet operations performed in digital microfluidics without the use of high electrical voltages or micromachining steps, we present a system where droplets are manipulated on a superhydrophobic surface (created on plastic sheets) by

gravitational forces and mechanical agitation. The superhydrophobic plastic sheets are further printed with unique symbols using a hydrophilic ink. A microcontroller controls the direction and timing of two stepper motors which, in turn, provide mechanical agitation for droplet transport. Droplets remain confined to the hydrophilic symbols, and are able to 'hop' to neighbouring symbols by gravity when the surface is agitated and tilted to a certain degree. Using this basic principle, we illustrate the following droplet operations: transport of single and multiple droplets, transport of larger-volume droplets, merging and mixing of multiple droplets, dispensing of fixed-volume droplets from a large droplet or liquid reservoir, and one-directional movement of droplets. As a proof-of-concept, we show the application of the system as a colorimetric assay to detect the concentration of glucose in sheep serum.

Experimental

Design of the droplet actuation system

The motorized actuation system consists of a two-axis tilting platform to manipulate movement of discrete liquid droplets on hydrophilic symbols printed on a superhydrophobic surface. Figure 2.1a shows the system configuration, including the three structural components: base, vertical column, and upper stage. The dimensions of these components are as follows: base (20 cm × 20 cm × 0.5 cm); vertical column (1 cm × 1 cm × 10 cm); upper stage (9 cm × 9 cm × 1.3 cm). The entire three-dimensional structure is designed in AutoCAD (Autodesk^{TM}) and the separate components are machined in acrylic glass (Plexiglas^{TM}). The stage is connected to the column by a universal joint that enables two-axis rotation about a central pivot. Two stepper motors (NEMA-17^{TM}, 200 steps per revolution, 12 volts, 350 milliamperes, bipolar mode) are connected with individual timing belts to the stage and mounted to the base. Each stepper motor controls one axis of rotation of the stage through an Arduino microcontroller (Adafruit Industries^{TM}).

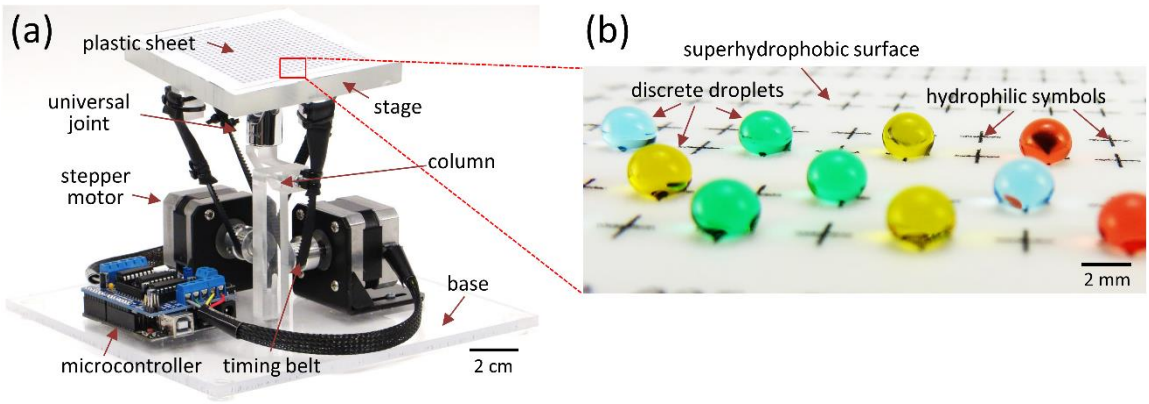

Figure 2.1 The droplet actuation system (a) The system comprises three structural components: base, column, and stage with plastic sheet. The base is physically screwed to the column. A universal joint connects the column to the stage. A microcontroller interfaces with two stepper motors (attached with individual timing belts) and controls the mechanical tilting of the stage. The plastic sheet is taped on the top of the stage. Scale bar = 2 cm. (b) A plastic sheet is spray-coated with a superhydrophobic chemical and printed with hydrophilic symbols using an inkjet printer. The image shows discrete droplets, each coloured with food dyes for visual illustration, resting on the hydrophilic symbols. Scale bar = 2 mm.

Single commands to tilt the stage up or down, left or right, and any sequence of such commands are programmed in a computer workstation and transmitted through a universal serial bus (USB) connection to the Arduino microcontroller. A graphical user interface (GUI) is designed for remote access to the droplet actuation system using a standard computer workstation. For image recording and characterization of droplet operations, a webcam (Logitech C920^{TM}) is positioned above the stage to monitor and record the simultaneous movement of multiple droplets.

Preparation of plastic sheets

After assembling the structural components of the droplet actuation system, we prepare the surface of plastic sheets that will serve as an open microfluidic arena to hold and move discrete droplets (Figure 2.1b). Initially, letter-sized transparency films (Staples Inc.^{TM}) are rinsed with distilled water and spray-coated with a commercially available superhydrophobic coating (Rust-Oleum NeverWet^{TM}). The coating procedure is a two-step process that involves

depositing a base coat and a top coat provided by the supplier. The base coat is applied by spraying on the surface of the transparency film. Three applications of the base coat are performed with a wait time of two minutes between successive applications. After drying for one hour, four applications of the top coat are performed in a similar fashion. The superhydrophobically-coated plastic sheet is dried for 12 hours at room temperature. Thereafter, hydrophilic symbols are printed on the plastic sheet by ink-jet printing. For this step, the plastic sheet is loaded into the document feeder of a commercial ink-jet printer (Epson WF-2540^{TM}). The layout of the desired symbols is drawn in Adobe Illustrator, saved on the computer, and printed using a black ink cartridge (Epson T200120^{TM}). After printing, the plastic sheet is dried for 12 hours at room temperature. Using the above procedure, a single letter-sized transparency film can produce six printed templates (9 cm × 9 cm) in one run.

Chemicals

Glucose Assay Kit (Sigma-Aldrich^{TM}, GAGO20) is composed of the following chemicals: glucose oxidase/peroxidase (Sigma-Aldrich^{TM}, G3660), and o-Dianisidine reagent (Sigma-Aldrich^{TM}, D2679). Glucose standard (Sigma-Aldrich^{TM}, G6918) and sheep serum (Sigma-Aldrich^{TM}, S3772) are also used. The glucose oxidase/peroxidase reagent is dissolved in 39.2 mL of deionized water. Next, o-Dianisidine reagent is added in 1 mL of deionized water. The assay reagent is prepared by adding 0.8 mL of the o-Dianisidine solution to the 39.2 mL of the glucose oxidase/peroxidase solution and mixing the solution thoroughly. The glucose standard solution is diluted to create 0.7 mg/mL, 0.6 mg/mL, 0.5 mg/mL, 0.4 mg/mL, 0.3 mg/mL, 0.2 mg/mL, and 0.1 mg/mL standards in deionized water. For control experiments, deionized water and black food dye (ACH Food Companies Inc.) are used.

Remote control and GUI Software

A graphical user interface (GUI) software is developed in Matlab to remotely access and control the mechanical movement of the droplet actuation system. The Adafruit Motor Shield v1 communicates with the Arduino microcontroller through theI2C (Inter IC) protocol and controls each of the stepper motors. The Arduino is further controlled from a computer workstation using the Arduino Integrated Development Environment™. The GUI enables commands to be easily sent to the Arduino microcontroller. The script accepts inputs to set the speed and number of steps taken by the motors, which, in turn, controls the angular movement of the stage about the central pivot. The GUI has options to control motor parameters, such as the number of steps, speed of rotation, and direction of rotation which eventually control the angular movement of the stage about the central pivot. In the default state, the position of the stage is assumed horizontal and is calibrated using a bubble level (Camco Manufacturing Inc.™). When the GUI software is first run, the connection to the Arduino microcontroller is established automatically by searching active COM ports. Once the Arduino COM port is confirmed to be connected, the user can enter the sequence of mechanical operations to be performed. In the GUI window, pressing the double arrows increases the stage's angle of rotation in the corresponding direction. The single arrow button rapidly tilts the stage to a specified angle, and then returns it to the default horizontal position. In addition, the GUI software communicates with a webcam to display a live preview of the top surface and record images or videos of droplet actuation.

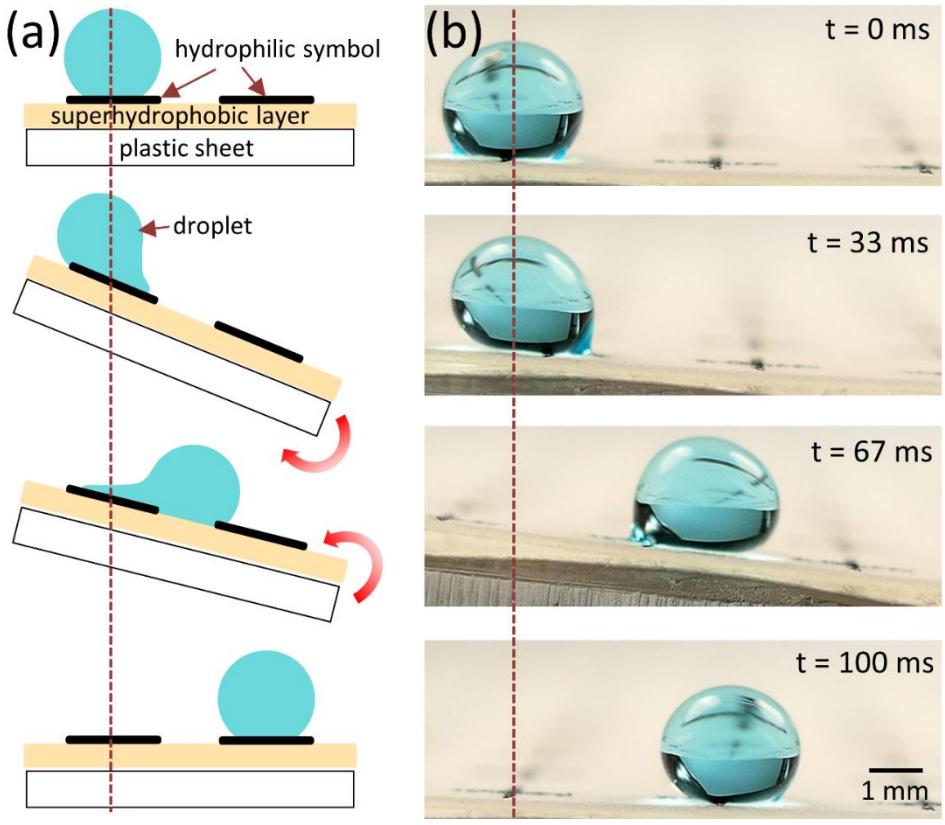

Figure 2.2 Transport mechanism of a single droplet. (a) In the cartoon, a droplet is initially positioned on the left hydrophilic symbol printed on the superhydrophobic surface of a plastic sheet. The stage is tilted clockwise and then anti-clockwise to return to its default horizontal position (depicted by red block arrows). This rapid tilting action enables the droplet to move to the right hydrophilic symbol. (b) Time-lapsed images of an actual droplet show how the droplet is transported from the left symbol to the right symbol by the tilting action of the stage. The vertical dotted lines represent the starting position of the droplet. Scale bar = 1 mm.

Result and Discussion

Transport of a single droplet

Figure 2.2a shows the side-view of a single droplet placed on a hydrophilic symbol (left-side) printed on a superhydrophobic layer. As the stage is tilted clockwise, the droplet remains on the hydrophilic symbol. But, as the stage is quickly tilted anti-clockwise to the default horizontal position, the droplet slides down the superhydrophobic surface and rests on the neighbouring hydrophilic symbol (right-side). In Figure 2.2b, side-view images of a single droplet are shown as it slides from the left symbol to the right one. The time for transporting a

single 10 µL droplet between two consecutive symbols is approximately 100 milliseconds. The stage is tilted at 100 revolutions per minute (r.p.m.) and the number of steps is 14.

The basic principle of droplet transport thus relies on positioning a droplet on a hydrophilic symbol and providing a rapid tilting action (i.e. tilting the stage clockwise (or anti-clockwise) to a specific angle followed by tilting the stage anti-clockwise (or clockwise) to the horizontal position). The rapid tilting action allows us to use small tilting angles (3°–5°) with acceleration and deceleration of a droplet. Alternatively, a single droplet can be transported by slowly tilting the stage in one direction which, however, requires a larger tilting angle (9°–20°) and provides no control on stopping the accelerated droplet.

We found that droplet transport can be controlled by a series of hydrophilic symbols printed at regular intervals. Based on initial tests, we chose to use 'plus (+)' symbols to demonstrate single droplet transport. Other symmetric symbols can also be used for this purpose. We printed plus symbols of different line widths and inter-symbol spacings. The transport of single droplets on the different symbols is recorded, and an average displacement error is measured in each case. Negative displacement error occurs when a droplet fails to detach from the initial symbol. Conversely, positive displacement error occurs when the droplet travels beyond the neighbouring symbol. In all cases, the droplet volume is 10 µL, tilting speed is 100 r.p.m., and number of steps is 14. The results indicate that symbols with thicker line widths produce negative displacement error as they have more surface area to hold the droplet in its original position. On the other hand, symbols with thinner line widths produce positive displacement error as they have insufficient surface area to hold or capture a sliding droplet. The optimal line width is 0.02 cm and the inter-symbol spacing is 0.335 cm, which produces a negligible displacement error of 0.005 cm. We also found that, using this optimal

dimension of the plus symbol, we can transport single droplets having a minimum and maximum water volume of 8 µL and 38 µL, respectively.

Physical model for droplet detachment from a hydrophilic symbol

Following the force balance analysis of Extrand and Gent [35], we assume the contact region of a liquid droplet on the superhydrophobic surface is circular with a radius *R*. The droplet is about to detach from the hydrophilic symbol and travel downwards as the stage is tilted from its horizontal position to a critical angle α. If the angular speed of the stage is ω revolutions per minute (r.p.m.) and the time for rotation is Δt minutes, then the critical angle $\alpha = 2\pi\omega\Delta t$ radians. The parameter Δt can be further expressed as $\Delta t = Nt_1$ minutes where *N* is the number of steps of the motor and t_1 is the time for one step rotation. The 'advancing edge' and 'receding edge' are labelled. For the plus symbol, the hydrophilic line width is *w* and the length is 2*R*. The liquid droplet has a surface tension γ, contact angle θ, viscosity η, density ρ, volume *V*, radius *r* (such that $V = (4/3)\pi r^3$), and linear velocity ν (such that $\nu = \omega\zeta$, where ζ = 3 cm is the distance from the pivot to the center of stage). The azimuthal angle ϕ circumnavigates the perimeter of the contact region between a value of $\phi = 0$ at the rear end of the droplet to a value to $\phi = \pi/2$ at the advancing side of the droplet.

There are three forces acting on the droplet as the stage is tilted: surface tension F_{ST}, gravitation force F_G, and viscous force F_V. At the critical angle α of the stage, the individual forces balance as:

$$F_{ST} + F_V = F_G \tag{2.1}$$

In eqn (2.1), the surface tension force F_{ST} can be divided into two components: force F_r acting on the rear of the droplet and force F_a acting on the advancing front of the droplet. Plugging in

the expressions for the gravitational force F_G acting parallel to the stage and the viscous force F_V, we get:

$$(F_r - F_a) + 6\pi\eta r v = \rho V g \sin\alpha \tag{2.2}$$

To compute the surface tension force, its component f per unit length of the contact perimeter varies along the perimeter as [35]:

$$f = \gamma \cos\theta \cos\phi \tag{2.3}$$

To simplify the calculation, we assume that $\cos\theta$ varies linearly around the perimeter of the contact region between a receding value of $\cos\theta_r$ at the rear end of the droplet (where $\phi = 0$) to an advancing value of $\cos\theta_a$ at the advancing side of the droplet (where $\phi = \pi/2$). For the case of a droplet on a homogeneous superhydrophobic surface, the expression for the contact angle is given by [35]:

$$\cos\theta = \frac{\phi}{\pi/2}\cos\theta_a + \left(1 - \frac{\phi}{\pi/2}\right)\cos\theta_r \tag{2.4}$$

Upon integration of eqn (2.3) and using eqn (2.4), the force acting on the rear of the drop F_r can be evaluated as:

$$F_r = 2\int_0^{\pi/2} f R d\phi = 2R\gamma \int_0^{\pi/2} \cos\theta \cos\phi d\phi \tag{2.5}$$

In our design with plus symbols, we modify eqn (2.4) to accommodate the role of hydrophilic symbol on the surface tension acting on the droplet. In other words, the hydrophilic symbol produces an inhomogeneity in the surface tension which is accounted for by splitting the force contributions of the hydrophilic ink and the superhydrophobic surface [36]. We denote the advancing and receding contact angles on the hydrophilic ink as $\cos\theta_{a,ink}$ and $\cos\theta_{r,ink}$, respectively. Similarly, the advancing and receding contact angles on the superhydrophobic surface are denoted as $\cos\theta_{a,sub}$ and $\cos\theta_{r,sub}$, respectively.

The parameter ϕ_1 indicates the azimuthal angle ϕ where the hydrophilic ink region changes to the superhydrophobic surface in the contact region, and is given by $\phi_1 = \sin^{-1}[w/(2R)]$.

Following from eqn (2.5), the force F_r acting on the rear of the droplet can be written as a sum of three forces:

$$F_r = 2R\gamma \left[\int_0^{\phi_1} \cos\theta_1 \cos\phi \, d\phi + \int_{\phi_1}^{\frac{\pi}{2}-\phi_1} \cos\theta_2 \cos\phi \, d\phi + \int_{\frac{\pi}{2}-\phi_1}^{\frac{\pi}{2}} \cos\theta_3 \cos\phi \, d\phi \right] \tag{2.6}$$

where

$$\cos\theta_1 = \frac{\phi}{\phi_1}\cos\theta_{r,sub} + \left(1 - \frac{\phi}{\phi_1}\right)\cos\theta_{r,ink} \tag{2.7}$$

$$\cos\theta_2 = \frac{\phi - \phi_1}{\frac{\pi}{2} - 2\phi_1}\cos\theta_{r,ink} + \frac{\frac{\pi}{2} - \phi_1 - \phi}{\frac{\pi}{2} - 2\phi_1}\cos\theta_{r,sub} \tag{2.8}$$

$$\cos\theta_3 = \frac{\phi - \frac{\pi}{2} + \phi_1}{\phi_1}\cos\theta_{a,ink} + \frac{\frac{\pi}{2} - \phi}{\phi_1}\cos\theta_{r,ink} \tag{2.9}$$

Similarly, the force F_a acting on the advancing front of the droplet can be written as a sum of three forces [36]:

$$F_a = 2R\gamma \left[\cos\theta_{a,ink} \int_0^{\phi_1} \cos\phi \, d\phi + \cos\theta_{a,sub} \int_{\phi_1}^{\frac{\pi}{2}-\phi_1} \cos\phi \, d\phi + \cos\theta_{a,ink} \int_{\frac{\pi}{2}-\phi_1}^{\frac{\pi}{2}} \cos\phi \, d\phi \right] \tag{2.10}$$

Substituting eqn (2.6) and eqn (2.10) into eqn (2.2), we can compute the critical angle α of the inclined stage where the gravitational force balances the surface tension and the viscous forces; thereby allowing the droplet to detach from the hydrophilic symbol and slide down the superhydrophobic surface.

To validate the physical model, experiments are conducted with water (density ρ = 1 g/cm^3, viscosity η = 0.001 Pa·sec, surface tension γ_w = 72.8 mN/m) and ethylene glycol (density ρ = 1.11 g/cm^3, viscosity η = 0.0162 Pa·sec, surface tension γ_{EG} = 47.7 mN/m) at temperature T = 20°C. We measured the advancing and receding contact angles of the two liquids as: (a) water: $\theta_{a,ink}$ = 147°, $\theta_{r,ink}$ = 81°, $\theta_{a,sub}$ = 157°, and $\theta_{r,sub}$ = 142° and (b) ethylene glycol: $\theta_{a,ink}$ = 134°, $\theta_{r,ink}$ = 73°, $\theta_{a,sub}$ = 140°, and $\theta_{r,sub}$ = 126°. The radius of the contact region is R = 0.12 mm. Table 2.1 shows the predicted and experimentally measured values of the critical angle α. The number of experiments (n) for each combination of line width and droplet volume is 10. In all cases, the predicted values lie within one standard deviation of the measured values.

It is worth noting that the viscosity of the liquid droplet is dependent on the concentration of dissolved electrolytes or sugars. The concentration-dependent viscosity of various sugar solutions can be modelled as [37]:

$$\eta = \eta_0 \, a \exp(EX) \tag{2.11}$$

where η_0 is the viscosity of pure water (in centiPoise), X is the mole fraction in the solution, E is the free energy, and a is a constant. The parameters a and E are numerically estimated from experiments. In the case of glucose solutions, the values of the parameters are a = 0.954 and E = 27.93 for up to 60% maximum concentration at temperature T = 20°C [37].

Table 2.1 Critical sliding angle α of a droplet (water and ethylene glycol) is predicted from the physical model and compared from experiments on the actuation system. Three droplet volumes are tested (20 µL, 30 µL, and 40 µL); each droplet volume is tested on plus symbols having three different line widths (0.152 mm, 0.178 mm, and 0.203 mm). Every combination of droplet volume and line width is tested 10 times.

Water

Droplet volume (µL)	Line width (mm)	Predicted α	Measured α
20	0.152	26.27°	24.1° ± 1.81°
	0.178	26.40°	26.2° ± 1.94°
	0.203	26.53°	28.5° ± 1.69°
30	0.152	17.19°	15.7° ± 1.18°
	0.178	17.28°	17.3° ± 1.62°
	0.203	17.36°	18.2° ± 1.16°
40	0.152	12.83°	11.7° ± 1.04°
	0.178	12.89°	12.7° ± 1.34°
	0.203	12.95°	13.4° ± 1.37°

Ethylene Glycol

Droplet volume (µL)	Line width (mm)	Predicted α	Measured α
20	0.152	20.99°	19.6° ± 1.36°
	0.178	21.06°	20.9° ± 1.70°
	0.203	21.13°	22.1° ± 1.42°
30	0.152	14.32°	13.3° ± 0.93°
	0.178	14.37°	14.8° ± 0.79°
	0.203	14.41°	15.5° ± 0.81°
40	0.152	10.99°	10.5° ± 0.81°
	0.178	11.02°	10.9° ± 0.81°
	0.203	11.05°	11.5° ± 0.72°

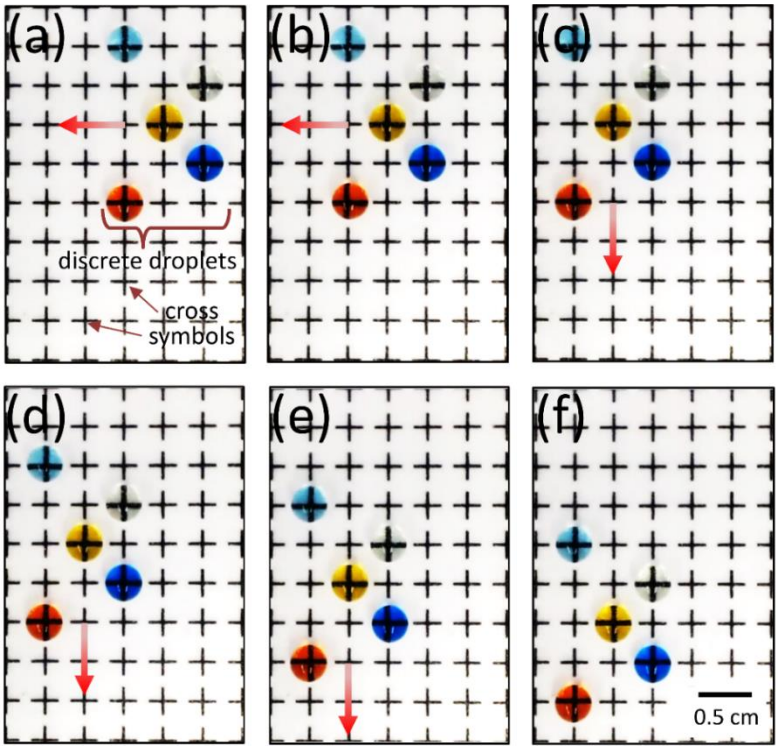

Figure 2.3 Transport of multiple droplets:A series of images are taken to illustrate the movement of multiple droplets on an arrangement of plus symbols. The volume of each droplet is 10 µL and they are uniquely coloured with a food dye for visual illustration. The motor speed is 100 r.p.m. and the number of steps is 14. The direction of tilting the stage at every step is denoted by a red arrow. The stage is rapidly tilted twice in left direction (a,b) and three times in the downward direction(c-e). The final positions of all droplets are shown in (f). This demonstration shows that multiple droplets can be simultaneously moved in the same direction without any risk of cross-contamination. Scale bar = 0.5 cm.

Transport of multiple droplets and large-volume droplets

Using the abovementioned principle, the droplet actuation system can be used to transport multiple discrete droplets. As shown in Figure 2.3, four droplets (each having 10 µL volume and coloured with different food dyes for visual illustration) are initially placed on separate plus symbols. For each symbol, the line width is 0.02 cm, line length is 0.24 cm, and inter-symbol spacing is 0.335 cm. The motor speed is 100 r.p.m. and the number of steps is 14. The red arrows in the figure indicate the direction of tilting the stage at each step. The stage is tilted to the right two times (Figure 2.3 a-b) and then downwards for three times (Figure 2.3 c-e). The final positions of the four droplets are shown in Figure 2.3f. The images indicate that

discrete droplets can be transported on a two-dimensional arrangement of plus symbols with virtually no risk of cross-contamination between droplets.

To address the challenge of transporting droplets having volumes greater than 38 µL, we designed arrays of plus symbols. Figure 2.4a shows images of the 80 µL droplet being transported using a 2×2 array of plus symbols (line width is 0.0178 cm, line length is 0.24 cm, and inter-array spacing is 0.68 cm). Reducing the speed and increasing the number of steps of the motor (80 r.p.m., 20 steps) allows transport of the 80 µL droplet. Here, the stage is tilted once to the right (Figure 2.4a i-ii), once downwards (Figure 2.4a-iii), and once to the left as depicted by the red arrows. The final position of the droplet is shown in Figure 2.4a-iv. Using a similar approach, Figure 2.4b shows images of the 300 µL droplet being moved using a 3×3 array of plus symbols (line width is 0.0178 cm, line length is 0.24 cm, and inter-array spacing is 0.94 cm). The motor speed is further reduced and the number of steps is increased to move this large droplet (60 r.p.m., 25 steps). Here, the stage is tilted to the left and the droplet settles on the neighbouring array of 3×3 symbols. Even though larger droplet volume can be transported by changing the design layout, we feel that the droplet volume of 300 µL adequately represents the maximum threshold needed for portable diagnostic testbeds [29-33].

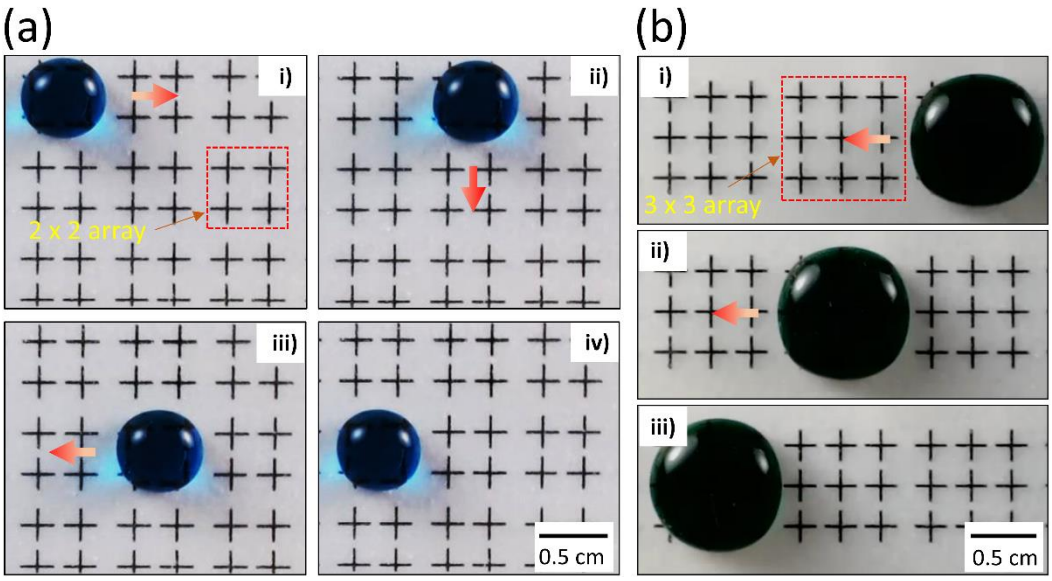

Figure 2.4 Transport of large droplets: (a) A large blue droplet (volume = 80 µL) is moved using a 2×2 array of plus symbols (line width is 0.0178 cm, line length is 0.24 cm, and inter-array spacing is 0.68 cm). Compared to Figure 2.3 where 10 µL droplets were moved, here the motor speed is decreased and the number of steps is increased ((80 r.p.m., 20 steps) to move the 80 µL droplet. (b) A large green droplet (volume = 300 µL) is being transported to the neighbouring pattern using a 3×3 array of plus symbols. As in (a), the motor speed is decreased and the number of steps is increased (60 r.p.m., 25 steps) compared to those in Figure 2.3. By using the same scheme and adjusting the parameters of stepper motors, up to 1 mL droplets have been transported. Scale bar = 0.5 cm.

Merging and mixing of multiple droplets

The ability to bring two droplets together, merge and mix them, and repeat these steps sequentially with a finite number of discrete droplets is important for realizing on-chip chemical reactions. To achieve this ability, it is required that some droplets remain stationary while other droplets are being transported, merged or mixed together. This is accomplished by using plus symbols of different line widths, where symbols with thicker line widths have more holding force than symbols with thinner line widths. Figure 2.5 shows images of a two-step merging and mixing performed on three droplets. The line widths of the plus symbols are thinnest in the left two columns (i.e. 0.015 cm holding the yellow droplet), medium thickness in the middle two columns (i.e. 0.02 cm holding the red droplet), and thickest in the right two

columns (i.e. 0.025 cm holding the blue droplet). For all symbols, the line length is 0.24 cm and inter-symbol spacing is 0.37 cm. The intent here is to merge the yellow droplet with the red one, and subsequently merge their product with the blue droplet. The stage is tilted in the following sequence: downwards, right, right, downwards, and right (Figure 2.5 a-e). The red arrows indicate the direction of tilting the stage. The final product formed after merging all the three droplets is shown in Figure 2.5f. It is interesting to note that the red and blue droplets are stationary when the yellow droplet is moved and merged with the red one (Figure 2.5 a-b), and the blue droplet is immobile throughout all the tilting operations. Thus, by adjusting the line widths of the plus symbols, we can selectively move one or more droplets to accomplish sequential merging operations. Post-merging, the mixing of two droplets is demonstrated in Figure 2.5c and Figure 2.5f by letting the merged product stay put on the symbol for some time (depending on the incubation time). This way of mixing by passive diffusion is satisfactory in case of droplets having soluble compounds. For droplets having immiscible or water-insoluble compounds, one can mix the droplets by agitating the stage (i.e. rapidly tilting the stage in alternate right and left directions in small angles) or moving the droplet in a circular pattern on neighbouring symbols.

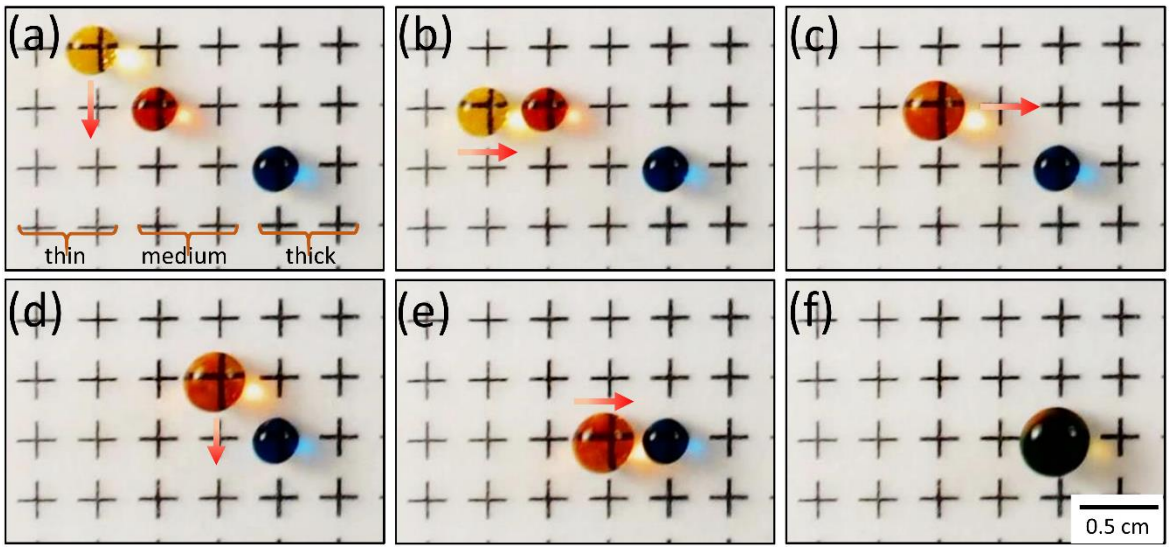

Figure 2.5 Merging and mixing of multiple droplets. (a) A two-dimensional arrangement of plus symbols is shown where the line width is thinnest in the left two columns, medium thickness in the middle two columns, and thickest in the right two columns. Three droplets (yellow, red, and blue) are placed on the plus symbols. The red arrow indicates the direction of tilting the stage and the stage is tilted in the following sequence: downwards, right, right, downwards, and right. The yellow droplet is moved to and merged with the red droplet (a-c). This merged droplet is now moved and merged with the blue droplet (d-e) and the final product after merging all droplets is shown in (f). After the merging step, the stage can be agitated to mix the combined droplets. Scale bar = 0.5 cm.

One-directional transport of droplets

While the plus symbols allow us to move droplets in two dimensions (i.e. left and right, upwards and downwards) on the plastic sheet, there is also interest to control droplet transport in only one direction (i.e. left or right only, upwards or downwards only). Previously, this transport mechanism was demonstrated on a texture ratchet where vibrations at the resonance frequency produced directed motion of droplets [15]. To accomplish this task in our system, we used a 'greater-than (>)' symbol that allows us to move a droplet only to the right side (i.e. converging side of the symbol) upon tilting the stage in that direction. For each symbol, the line width is 0.023 cm and the length of each line is 0.33 cm. The acute angle between the two lines of the greater-than symbol is 28°. Figure 2.6a shows images of two droplets; one placed

on a greater-than symbol and the other on a plus symbol. The stage is tilted in the following sequence: right, left, right, and left. The droplet on the row of plus symbols follows the direction of stage tilting, and eventually returns to its original position. In comparison, the droplet on the greater-than symbol is held at its original position when the stage is tilted to the left but moves to the right when the stage is tilted to the right. Figure 2.6b shows the dynamics of the droplet on the greater-than symbol during the left or right tilting of the stage. During the left tilting, the droplet is still held in its original position due to the asymmetry of the greater-than symbol (on its left side compared to its right side). During the right tilting, the droplet volume concentrates to the narrow point of the symbol (on its right side) and is able to slide to the neighbouring symbol. Figure 2.6c shows images of a droplet placed at the center of three converging greater-than symbols. Here the line width is 0.023 cm, length of each line is 0.33 cm, and the acute angle of each greater-symbol is 28°. Similar to Figure 2.6 a-b, this symbol also allows movement of droplets only to the right side but is able to hold the droplet on its central position even when the stage is tilted left, up or down. Thus one greater-than symbol prevents droplet movement in the left direction while the three converging greater-than symbols prevent droplet movement in the left, up, and down directions.

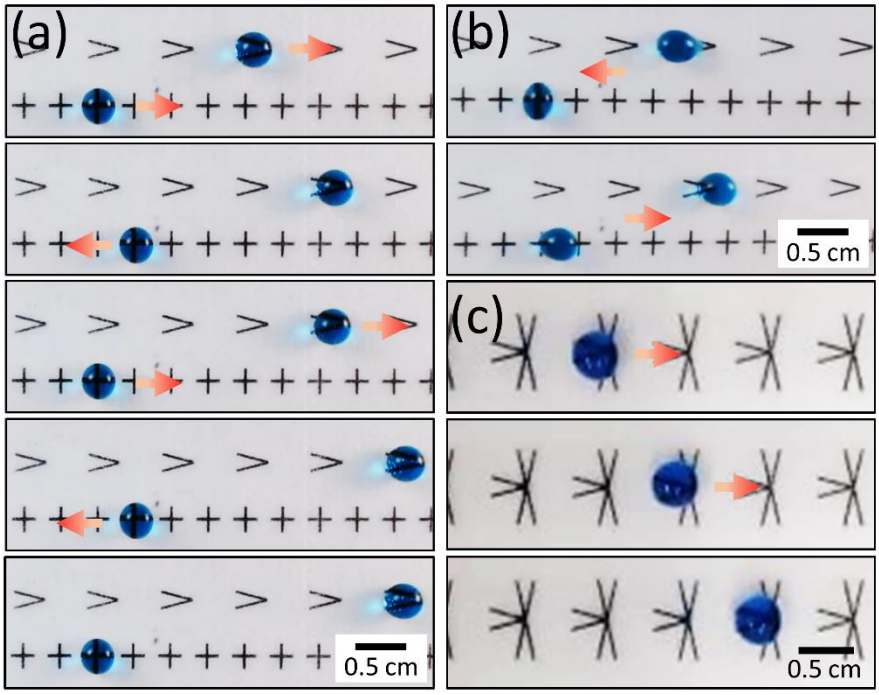

Figure 2.6 One-directional transport (a) Each droplet is placed on two different symbols (plus and greater-than sign). The droplet on the plus symbol moves to the left when rapidly tilted to the left, but the droplet on the greater-than symbol does not move. When the substrate rapidly tilts to the right, both droplets on the plus symbol and the greater-than symbol move to the right. The acute point of the greater-than symbol has less hydrophilic area to attract the droplet. (b) Slow motion images showing different configurations of the droplet when the stage rapidly tilts to the left and right directions. When the stage tilts left, the two diagonal lines attached to the large area of the droplet prevent it from moving to next symbol. When the stage tilts right, a sharp point (where two diagonal lines meet) attaches to a small area of the droplet and the droplet is released to the next symbol. (c) One directional movement: The droplet only moves to the right due to the pattern of three converging greater-than symbols pointing to the center.

Dispensing smaller droplets from a large droplet

In wet chemistry experiments, it is often desired to pipette small volumes of reagents or samples repeatedly for multiple tests. As such, there is a need to generate equal volumes of smaller droplets from a large droplet (which may be a reagent or test sample). Typically, this is achieved in devices based on electrowetting [16-21] or by using a superhydrophobic blade to split a large droplet [14]. We accomplish this task by moving the large droplet over a series of circular dot symbols. Figure 2.7a shows the side-view of a large red droplet moving over four dot symbols, and leaving behind a small droplet over each traversed symbol. Besides

circular dot symbols, we can use rectangular or diamond-shaped symbols for dispensing small droplets, as shown in Figure 2.7b and Figure 2.7c, respectively (in all cases, the symbol area is 0.0097 cm^2). In Figure 2.7d, we show how dispensing and mixing are performed sequentially. Here, a large red droplet moves over a row of dot symbols, leaving behind small droplets over each symbol (Figure 2.7 d-i-iii). Afterwards, a water droplet is moved over the same set of dot symbols, thereby mixing the previously-left behind red droplets with water (Figure 2.7 d-iv-vi). We conducted experiments to measure the actual volume of small droplets left behind as a 10 µL water droplet travels over plus symbols and different-sized dot symbols. In addition to the fluid properties, the volume of droplets dispensed on the dot symbol is determined by the surface area of the symbol or surface defect [38,39], which can be increased or decreased depending on the desired volume of dispensed droplets.

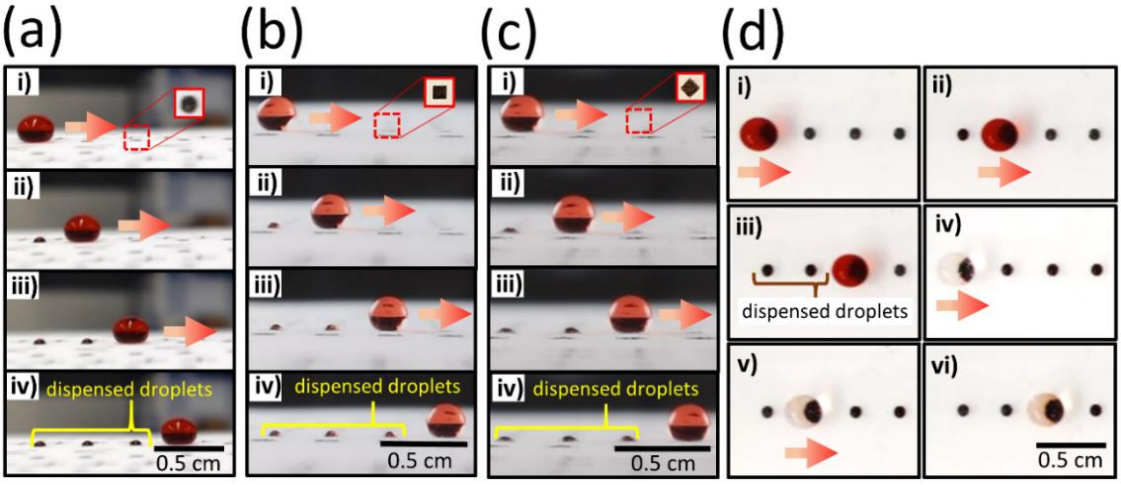

Figure 2.7 Droplet dispensing from a large droplet (volume = 10 µL): (a) A small red droplet is dispensed on each circular dot hydrophilic symbol. While a large droplet moves over the hydrophilic dots, each symbol attracts the droplet and a small volume is left on each symbol. (b) Small red droplets are dispensed on rectangular-shaped hydrophilic symbols. (c) Small red droplets are dispensed on diamond-shaped hydrophilic symbol. (d) After the dispensing operation on circular dot symbols, a clear water droplet is transported across the dot symbols, causing the red colour intensity to increase in the clear droplet. Scale bar = 0.5 cm.

Dispensing droplets from an external reservoir

Besides dispensing smaller droplets from a large droplet, it is beneficial to develop a mechanism to dispense finite droplets from an external liquid reservoir that may contain a much larger liquid volume (e.g. cartridges, tubes, and syringes) [7]. To achieve this method of dispensing, a syringe-based dispenser is realized. Here, the tip of a 20 mL syringe is cut, plugged by a 200 µL pipette tip, and then attached to a 1 mL syringe. The pipette tip is sealed with a cyanoacrylate adhesive along with a steel wire to extend the tip. This syringe-based dispenser is positioned above the plastic sheet on the stage (Figure 2.8a). As the syringe tip faces downwards, gravitational force prevents liquid from back-flowing through the 20 mL syringe. When the stage is rapidly tilted, the steel wire is momentarily pushed up (Figure 2.8b) to dispense a small droplet on the hydrophilic symbol underneath (Figure 2.8c). This step can be repeated several times to dispense a series of discrete droplets from the reservoir (Figure 2.8 d- f).

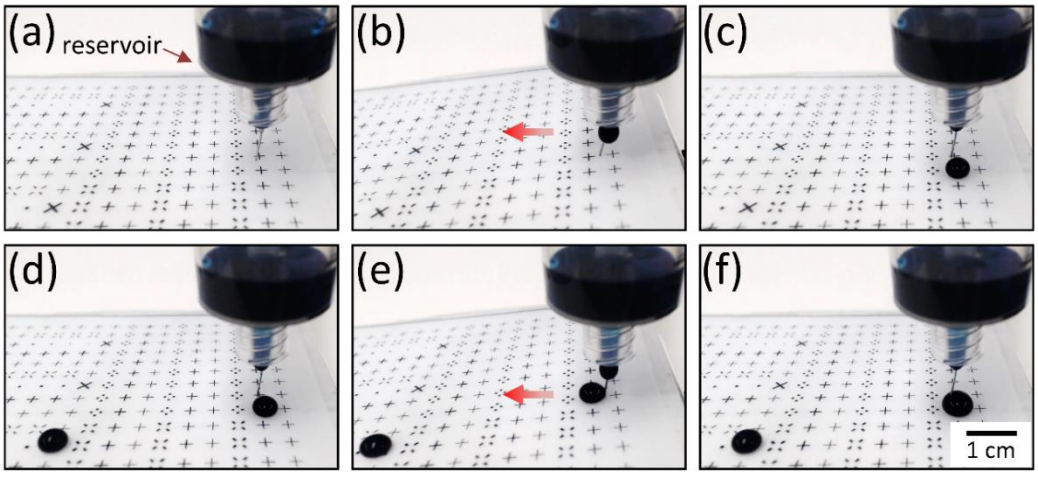

Figure 2.8 Dispensing droplets from an external reservoir : (a) The reservoir is placed along the edge of the stage. (b) A dispenser tip is pressed by tilting the stage. (c) While the tip is pushed up, liquid flows out through the opened entrance of the reservoir. (d) A dispensed droplet is transported to another symbol and the next droplet is dispensed. (e,f) By tilting the stage twice, a larger droplet is dispensed in the same location. Scale bar = 1 cm.

Glucose detection

As a proof-of-concept, the droplet actuation system is employed to determine the glucose concentration in sheep serum using a colorimetric enzymatic test. The following reaction details the chemical reactions involved in the colorimetric test for glucose [34].

$$\text{d-glucose} + H_2O + O_2 \xrightarrow{\text{glucose oxidase}} \text{d-gluconic acid} + H_2O_2 \quad (2.12)$$

$$H_2O_2 + \text{reduced o-Dianisidine} \xrightarrow{\text{peroxidase}} \text{oxidized o-Dianisidine} \quad (2.13)$$

In the presence of glucose oxidase, d-glucose is oxidized to d-gluconic acid and hydrogen peroxide. The colorless o-Dianisidine reacts with hydrogen peroxide, in the presence of peroxidase, to form a brown-coloured oxidized o-Dianisidine.

Initially, experiments are conducted in 24-well plates to characterize the colorimetric glucose assay. A standard glucose assay kit is used to prepare glucose solutions of different dilution factors. Around 250 µL of each solution is loaded into separate well plates, followed by 500 µL of assay reagent in each well. A webcam is used to record the colour of all well solutions for 30 minutes (frame rate: 29 frames per second). A Matlab script is written to extract the colour intensity of each well solution as a function of time. Specifically, the user selects different cropped areas in the first image. Then the script identifies the selected areas of all subsequent images in a video. The 3-channel (RGB) images are converted into 1-channel (i.e. grayscale) images using ITU-R Recommendation BT.601, and the average colour intensity values are estimated as a function of time. The colour intensity data are exported to a Microsoft Excel spreadsheet. The maximum slope for each solution (i.e. maximum change in colour intensity per second) is determined that correlates to the initial concentrations of glucose [34]. For each run with glucose samples, two control samples are used: deionized water with reagent and black food dye with reagent. The sheep serum is tested in a similar manner to give its

glucose concentration (i.e. 0.59 mg/mL), which is close to the value obtained from a microplate reader (i.e. 0.63 mg/mL).

After conducting the well plate experiments, we performed a similar set of experiments on the droplet actuation system. After preparing the same dilutions of glucose solution, 5 µL droplets are placed on the middle column of plus symbols (line width = 0.015 cm) as shown in Figure 2.9a. Another set of 10 µL glucose reagents are placed on the leftmost column of plus symbols (line width = 0.02 cm). When the stage is tilted to the right, the two columns of droplets (i.e. of glucose samples and reagents) merge on the middle column (Figure 2.9b). Upon further tilting the stage to the right, the merged droplets settle on the rightmost column of X-shaped symbols (Figure 2.9c) where they are agitated to be mixed thoroughly (Figure 2.9 d-g) and incubated for the chemical reaction (Figure 2.9 h-j). We found that agitating the stage reduces the mixing time of a merged droplet (using 5µL red droplet and 20µL yellow droplet) from 550 seconds with passive diffusion to 60 seconds with stage agitation (i.e. approximately a nine-fold reduction in mixing time). As shown in Figure 2.9h, the colour change is visible after around 10 seconds of incubation. The higher the glucose concentration, the darker is the colour of the incubated droplet. The Matlab script accurately determines the average colour intensity of the droplets (Figure 2.10a), which is later used to estimate the glucose concentrations in each droplet (Figure 2.10b). The sheep serum is also tested in parallel with other glucose samples. Using the standard curve equation, the unknown glucose concentration of sheep serum is calculated as 0.62 mg/mL, which is close to the readings from the microplate reader and well plate experiments.

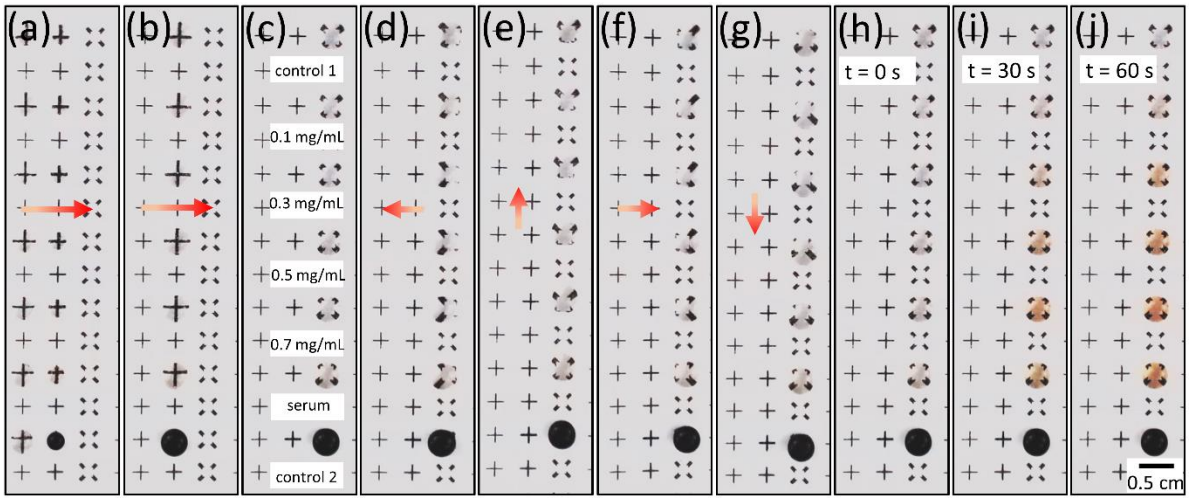

Figure 2.9 Glucose detection on the droplet actuation system (a) Glucose standards of different concentrations are placed on the middle column of plus symbols and the glucose reagents are placed on the leftmost column. (b) The stage is tilted to the right and the two columns of droplets merge on the middle column. (c) The merged droplets settle on the third column. (d-g) The stage is agitated in multiple directions to mix the combined droplets (h-j). The merged droplets are incubated for the chemical reaction and the colour change is visible after around 10 seconds of incubation. The colour intensity is darker for droplets having higher glucose concentrations. Scale bar = 0.5 cm.

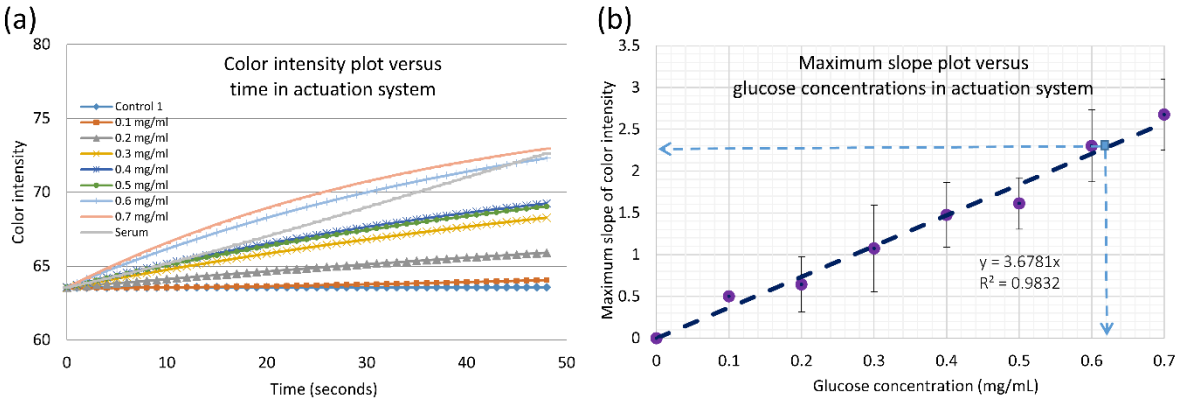

Figure 2.10 Determination of glucose concentrations in sheep serum. (a) The colour intensities of incubated droplets at different time points are shown. Each glucose concentration is tested three times (n = 3). (b) The maximum slope of each colour intensity graph at different glucose concentrations is plotted to obtain the standard curve equation and to determine the glucose concentration in sheep serum.

Table 2.2 summarizes the system parameters for the various droplet operations. Table 2.3 shows the flexibility of the system in transporting droplets having different fluid properties and different volumes. The three fluids tested are: water, milk, and ethylene glycol. Keeping the operating conditions fixed (i.e. motor speed = 100 r.p.m., number of steps= 14), we found that a wide range of droplet volumes (7 µL to 40 µL of water) can be transported on plus symbols (line width = 0.152 mm). However, under the same operating conditions, the range of droplet volumes transported on plus symbols decreases for a viscous liquid (12 µL to 26 µL of ethylene glycol).

Table 2.2 Values of the system parameters for the different droplet operations.

Droplet Operation	Figure number	Volume (µL)	Speed (r.p.m.)	Steps N	Line width (cm)	Inter-symbol spacing (cm)
Single droplet transport	2	10	100	14	0.02	0.335
Multiple droplets transport	3	10	100	14	0.02	0.335
Large droplet transport	4(a)	80	80	20	0.0178	0.68
	4(b)	300	60	25	0.0178	0.94
Merging and mixing	5(a,b): left 2 columns	10	80	14	0.015	0.37
	5(c-e): middle 2 columns	20	90	14	0.02	0.37
	5(f): right 2 columns	30	0	0	0.025	0.37
One-directional transport	6(a,b)	10	100	14	0.023	0.37 (+) 0.74 (>)
	6(c)	20	100	14	0.023	0.74
Dispensing droplets	7(a-d)	10	100	14	area =0.0097 cm^2	0.37
Glucose detection	9(a): left column	10	100	14	0.015	0.45
	9(a): middle column	5	100	14	0.02	0.45
	9(c): right column	15	100	14	0.038	0.45
	9(d-g): right column	15	40	25	0.038	0.45
	9(i,j): right column	15	0	0	0.038	0.45

Table 2.3 The range of droplet volumes that can be transported on plus symbols is shown. Three different fluids are tested: water, milk, and ethylene glycol. The operating conditions of the motors is fixed (speed = 100 r.p.m., number of steps = 14). Each experiment on the minimum and maximum droplet volume is conducted 5-7 times.

Fluid droplet	Fluid properties	Line width (mm)	Volume (µL)
Water	η = 0.001 Pa·sec	0.152	7 - 40
	ρ = 1 g/cm^3	0.203	8 - 38
	γ_w = 72.8 mN/m	0.254	10 - 36
Milk	η = 0.003 Pa·sec	0.152	7.5 - 38
	ρ = 1.032 g/cm^3	0.203	9 - 35
	γ_m = 52.4 mN/m	0.254	11 - 33
Ethylene Glycol	η = 0.0162 Pa·sec	0.152	12 - 26
	ρ = 1.11 g/cm^3	0.203	17 - 24
	γ_{EG} = 47.7 mN/m	0.254	20 - 22

Conclusion

We demonstrated a droplet actuation system where discrete droplets are manipulated on hydrophilic patterns printed on a superhydrophobic plastic surface. Gravitational forces and mechanical agitation of the stage enable the transport of droplets. The system is designed for low-cost, resource limited settings where large area, disposable plastic sheets can be printed from standard inkjet printers and portable 9V batteries power the motorized stage. We showed the possibility of transporting multiple droplets (volumes: 8 µL to 300 µL) in parallel and performing sequential fluidic reactions that will be beneficial to a variety of biological experiments. With the presented method, the design and layout of the hydrophilic symbols can be easily altered to specific functional requirements of an experiment. Lastly, the integration of smart image analysis tools with the droplet actuation system helps to automatically extract the parametric data, thereby minimizing human bias.

Acknowledgements

This work is partially supported by the U.S. National Science Foundation (NSF CBET-1150867 and NSF DGE1247194). In addition, T. K. is partially supported by a grant from the Defence Threat Reduction Agency (HDTRA1-15-1-0053).

References

1 K. S. Elvira, X. C. Solvas, R. C. Wootton and A. J. deMello, Nature Chemistry, 2013, 5, 905–915.

2 E. K. Sackmann, A. L. Fulton and D. J. Beebe, Nature, 2014, 507, 181–189.

3 M. J. Jebrail, M. S. Bartsch and K. D. Patel, Lab Chip, 2012, 12, 2452–2463.

4 M. G. Pollack, A. D. Shendorov and R. B. Fair, Lab Chip, 2002, 2, 96–101.

5 K. Choi, A. H. C. Ng, R. Fobel and A. R. Wheeler, Annu. Rev. Anal. Chem., 2012, 5, 413–440.

6 W. C. Nelson and C.-J. Kim, J. Adhes. Sci. Technol., 2012, 26, 1747–1771.

7 A. Ghosh, R. Ganguly, T. M. Schutzius and C. M. Megaridis, Lab chip, 2014, 14, 1538–1550.

8 S. Y. Park, M. A. Teitell and E. P. Y. Chiou, Lab Chip, 2010, 10, 1655–1661.

9 Z. Long, A. M. Shetty, M. J. Solomon and R. G. Larson, Lab Chip, 2009, 9, 1567–1575.

10 J. Seo, S. Lee, J. Lee and T. Lee, ACS Appl. Mater. Interfaces, 2011, 3, 4722–4729.

11 V. Jokinen, L. Sainiemi and S. Franssila, Adv Mater, 2008, 20, 3453-3456.

12 Z. Wang and J. Zhe, Lab Chip, 2011, 11, 1280–1285.

13 D. Foresti, M. Nabavi, M. Klingauf, A. Ferrari and D. Poulikakos, Proc. Natl. Acad. Sci. U. S. A., 2013, 110, 12494–12554.

14 H. Mertaniemi, V. Jokinen, L. Sainiemi, S. Franssila, A. Marmur, O. Ikkala and R. H. Ras, Adv Mater, 2011, 23, 2911-2914.

15 T. A. Duncombe, E. Y. Erdem, A. Shastry, R. Baskaran and K. F. Bohringer, Adv Mater, 2012, 24, 1545-1550.

16 J. Gong and C. J. Kim, J Microelectromech Syst, 2008, 17, 257-264.

17 C. Peng, Z. Zhang, C. J. Kim and Y. S. Ju, Lab Chip, 2014, 14, 1117-1122.

18 S. C. Shih, P. C. Gach, J. Sustarich, B. A. Simmons, P. D. Adams, S. Singh and A. K. Singh, Lab Chip, 2015, 15, 225-236.

19 S. Srigunapalan, I. A. Eydelnant, C. A. Simmons and A. R. Wheeler, Lab Chip, 2012, 12, 369-375.

20 M. Abdelgawad, S. L. Freire, H. Yang and A. R. Wheeler, Lab Chip, 2008, 8, 672-677.

21 C. J. Huang, W. F. Fang, M. S. Ke, H. Y. E. Chou and J. T. Yang, Lab Chip, 2014, 14, 2057-2062.

22 B. Hadwen, G. R. Broder, D. Morganti, A. Jacobs, C. Brown, J. R. Hector, Y. Kubota and H. Morgan, Lab Chip, 2012, 12, 3305-3313.

23 P. Y. Chiou, H. Moon, H. Toshiyoshi, C.-J. Kim and M. C. Wu, Sensors and Actuators A: Physical, 2003, 104, 222-228.

24 R. Renaudot, V. Agache, Y. Fouillet, G. Laffite, E. Bisceglia, L. Jalabert, M. Kumemura, D. Collard and H. Fujita,
Lab Chip, 2013, 13, 4517-4524.

25 Z. Guttenberg, H. Müller, H. Habermüller, A. Geisbauer, J. Pipper, J. Felbel, M. Kielpinski, J. Scriba and A. Wixforth, Lab Chip, 2005, 5, 308-317.

26 Z. Hua, J. L. Rouse, A. E. Eckhardt, V. Srinivasan, V. K. Pamula, W. A. Schell, J. L. Benton, T. G. Mitchell and M. G. Pollack, Anal. Chem., 2010, 82, 2310-2316.

27 H. Kim, M. S. Bartsch, R. F. Renzi, J. He, J. L. Van de Vreugde, M. R. Claudnic and K. D. Patel, J. Lab. Autom., 2011, 16, 405-414.

28 R. Sista, Z. Hua, P. Thwar, A. Sudarsan, V. Srinivasan, A. Eckhardt, M. Pollack, V. Pamula, Lab Chip, 2008, 8, 2091-2104.

29 N. A. Mousa, M. J. Jebrail, H. Yang, M. Abdelgawad, P. Metalnikov, J. Chen, A. R. Wheeler, R. F. Casper, Sci. Transl. Med., 2009, 1, 1ra2.

30 C. Arnaud, Chem. Eng. News, 2011, 89, 13-17.

31 R. S. Sista, A. E. Eckhardt, T. Wang, C. Graham, J. L. Rouse, S. M. Norton, V. Srinivasan, M. G. Pollack, A. A. Tolun, D. Bali, D. S. Millington, V. K. Pamula, Clin. Chem., 2011, 57, 1444-1451.

32 M. J. Jebrail, H. Yang, J. M. Mudrik, N. M. Lafreniere, C. McRoberts, O. Y. Al-Dirbashi, L. Fisher, P. Chakraborty, A. R. Wheeler, Lab Chip, 2011, 11, 3218-3224.

33 S. C. C. Shih, H. Yang, M. J. Jebrail, R. Fobel, N. McIntosh, O. Y. Al-Dirbashi, P. Chakraborty, A. R. Wheeler, Anal. Chem., 2012, 84, 3731-3738.

34 V. Srinivasan, V. K. Pamula and R. B. Fair, Anal. Chem. Acta, 2004, 507, 145-150.

35 C. Extrand and A. Gent, J. Colloid Interface Sci., 1990, 138, 431-442.

36 M. Elsharkawy, T. M. Schutzius and C. M. Megaridis, Lab Chip, 2014, 14, 1168-1175.

37 J. Chirife and M. P. Buera, Journal of Food Engineering, 1997, 33, 221-226.

38 J. Schneider, A. Egatz-Gomez, S. Melle, S. Lindsay, P. Dominguez-Garcia, M. A. Rubio, M. Marquez and A. A. Garcia, Colloids and Surfaces A: Physicochem. Eng. Aspects, 2008, 323, 19-27.

39 N. A. Patankar, Langmuir, 2003, 19, 1249-1253.

CHAPTER 3.

A FAST, RECONFIGURABLE FLOW SWITCH FOR PAPER MICROFLUIDICS BASED ON SELECTIVE WETTING OF FOLDED PAPER ACTUATOR STRIPS

Modified from our journal article, "A fast, reconfigurable flow switch for paper microfluidics based on selective wetting of folded paper actuator strips", Lab on a Chip, 16, 1861-1872, 2016.

Taejoon Kong,* Shawn Flanigan,* Matthew Weinstein, Upender Kalwa, Christopher Legner and Santosh Pandey
** Joint first authors*

Abstract

In paper microfluidics, the development of smart and versatile switches is critical for the regulation of fluid flow across multiple channels. Past approaches in creating switches are limited by long response times, large actuation fluid volumes, and use of external control circuitry. We seek to mitigate these difficulties through the development of a unique actuator device made entirely out of chromatography paper and incorporated with folds. Selective wetting of the fold with an actuation fluid, either at the crest or trough, serves to raise or lower the actuator's tip and thus engage or break the fluidic contact between channels. Here the actuator's response time is dramatically reduced (within two seconds from wetting) and very small volume of actuation fluid is consumed (four microliters). Using this actuation principle, we implement six switch configurations which can be grouped as single-pole single-throw (normally OFF and normally ON) and single-pole double-throw (with single and double break). By employing six actuators in parallel, an autonomous colorimetric assay is built to detect the presence of three analytes – glucose, protein, and nitrite – in artificial saliva. Finally, this work brings the concept of origami to paper microfluidics where multiple-fold geometries can be exploited for programmable switching of fluidic connections.

Introduction

Paper-based device technology is an established sub-class of microfluidics [1-6] that aims to rival Lateral Flow Test (LFT) assays [7-9] with their cheap costs, user friendliness, field-ready capability, and rapid time to result. A number of applications could immediately benefit from these field-deployable platforms, including those in healthcare [10], environmental monitoring [11], and food safety [12,13]. For instance, integrated paper-based platforms can be used to quickly detect food- and water-borne pathogens, early disease biomarkers from bodily fluids, and chemical contaminants or toxins in drinking water with the power to communicate the results wirelessly to related professionals [1-6, 10-15].

The scientific community has performed research in various areas of paper-based microfluidic technology, including device architectures, fabrication and printing methods, surface functionalization schemes, fluid flow control strategies, application-specific protocols, readout instrumentation and mobile apps, and modelling of fluid transport and surface chemistry [16-21]. The driving force behind this rapid progress can be rightly attributed to the need for technology commercialization and widespread adoptability. While technology commercialization necessitates large volume production, low manufacturing costs, long shelf life and transportability, widespread adoptability requires customer satisfaction through easy-to-build and easy-to-use methodologies, faster testing times, digital readout, and reliable accuracy [6,22]. Just as LFT assays have created a billion-dollar industry in at-home pregnancy testing, there is scope for paper-based devices to capitalize the diagnostics market with ingenious fluidic toolkits and "killer applications" (e.g. for low-cost gene identification from environmental and clinical samples, multiplexed point-of-care screening of potential threat biomarkers) [23,24]. A notable example of a paper-based microfluidic company is Diagnostics

For All (DFA) that has developed a range of capillary flow-based, colorimetric test platforms for use in resource-limited countries [1-4]

To target commercially-viable applications, paper-based platforms should be able to handle multiple steps of an experiment, such as preparing samples, performing chemical tests, and detecting output signals [25-34]. Even though a range of expensive instruments are available today to perform the steps in a diagnostic assay, a cheaper and all-integrated alternative in paper microfluidics could overcome the price barrier which is much needed in resource-limited settings. An important operation in realizing fully-functioning paper-based platforms is the regulation and switching of fluid flow in multiple channels [26]. The key metering parameters to regulate fluid flow in paper channels are: (i) fluid velocity, (ii) delay time, and (iii) switch configurations [16].

Fluid velocity in a porous paper substrate can be regulated by manipulating parameters of the Lucas-Washburn flow equation, such as the medium porosity, fluid surface tension, fluid viscosity, and contact angle [35,36]. The geometric design (i.e. length and width) of porous channels can be altered to help speed up or slow down the advancement of fluid within the channels [37,38]. To achieve higher changes in fluid velocity within individual channels, the porous medium can be removed to create hollow channels with the incorporation of barriers or trenches in the fluid path to accelerate or impede the fluid flow [39-41].

To regulate the *delay time of fluid flow* within a channel, fluidic delay timers have been realized by applying different concentrations [42] and colors of wax material [43] to the porous medium which modify the resistance or wettability of the channel and control the delay time. Another method to delay fluid flow involves the incorporation of dried dissolvable species (e.g. sucrose barriers) within the channel where the length of time delay is tunable and depends

on the concentration of dissolvable species [44]. Delay in fluid flow can also be accomplished by placing absorbent shunt pads parallel to the porous medium where the material properties and physical dimensions of the shunt determine the delay time [45].

The common *switch configurations* in paper microfluidics are 'normally OFF' and 'normally ON'. A 'normally OFF' switch (with no initial fluid flow) is actuated to permit fluid flow after a specific time while a 'normally ON' switch (with initial fluid flow) is actuated to block fluid flow after a finite time. User-activated, mechanical valves have been demonstrated in paper microfluidics to enable a 'normally OFF' channel to make contact with a reservoir (when desired by the user) and turn ON by the use of folding cards [46], sliding action [47] or push buttons [3]. Autonomous valves have been shown where the hydrophobicity of a 'normally OFF' channel is altered to become hydrophilic and turn on by methods, such as polarization-based switching of an enclosed dielectric coating [48], temperature-controlled manipulation of surfactant solubility [49], corona discharge treatment of coated channels [50], and melting of embedded wax barriers using on-chip heating elements [51]. On the other hand, fluid flow in a 'normally ON' channel can be switched off by using bridges composed of dissolvable material (e.g. sucrose, mannose or pullulan films) [52] or by physically lowering the relative height of the reservoir with respect to the channel's inlet [53].

This work presents a novel valving concept for paper microfluidics where reversible switching between OFF and ON states is accomplished. The basic idea of using a paper-based device component both as a 'normally OFF' and 'normally ON' switch has recently been presented in two publications [26,54] In the first example [54], a magnetic timing valve was fabricated by screen-printing silver ink electrodes on laser-cut paper strips and attaching a bridge of ferrous nanoparticle–PDMS blend. An ionic resistor triggered a power switch IC

chip to activate an electromagnet and open/close the magnetic valve. Using the magnetic paper bridge, both 'normally ON' and 'normally OFF' switches were shown with a proof-of-concept demonstration of alkaline phosphate-based colorimetric reaction. One drawback of the magnetic timing valve is the need for an electromagnet and an electrical circuit (with power switch IC) which creates an extra cost burden. In the second example [26], an actuator channel is made of high permeability glass fiber and the actuator is a compressed cellulose sponge adhered at the end of the actuator channel. The presence of actuation fluid causes expansion of the compressed sponge actuator that physically connects the input channel to the output channel. Three switch configurations have been demonstrated (i.e. 'normally OFF', 'normally ON', and diversion switches) along with control over the time for actuation and fluid flow volume by varying the wick lengths and size of absorbent pads, respectively. In this sponge actuation method [26], there is scope to reduce the fluid absorption time by the sponge material (from 1.9 minutes) and volume of actuation fluid (from 500 μL).

Building on the above literature on switches for paper microfluidics and origami in paper-based devices [55,56], we introduce an all-paper actuator that functions to reversibly control fluid flow from input channel(s) to output channel(s). The actuator is made entirely of chromatography paper – the same material used to make the flow channels. There are no external components adhered onto the paper actuator, unlike the previous examples of reversible switches which employ magnetic PDMS or sponge pads [26,54]. There is no external control circuitry or instrumentation to trigger the actuator. The actuator strip consists of uniquely-sized folds and is fastened at one end with tape. By dropping a small volume of fluid (~ 4 μL) on the crest (or trough) of a fold, the actuator tip is raised (or lowered) to engage (or break) a physical contact between the input and output channels (Figure 3.1a). Using this

basic principle, we realized the following two switch configurations: single-pole single-throw (SPST) and single-pole double-throw (SPDT). The SPST and SPDT terminology is commonly used in the classification of commercial switches. The 'pole' refers to the number of inter-channel fluid connections being controlled by the actuator at a given time, while the 'throw' refers to the extreme (i.e. ON) position of the actuator. We show a SPST switch (similar to 'normally OFF' and 'normally ON' modes) that has one ON position and controls fluid flow across one inter-channel interface (Figure 3.1b). The SPDT switches are also shown where two ON positions are possible and only one inter-channel interface is turned on at a given time. By actuating combinations of the fold's crests and troughs, four configurations of the SPDT switches have been realized (Figure 3.1c, d). Lastly, a colorimetric assay is realized to detect the presence of three analytes – glucose, protein, and nitrite – in artificial saliva in an integrated platform. Control tests are run in parallel on the same platform. The assay is operated by six actuators which are activated by two delay timer paper strips and the time for actuation is automatically controlled by the wicking of actuation fluids.

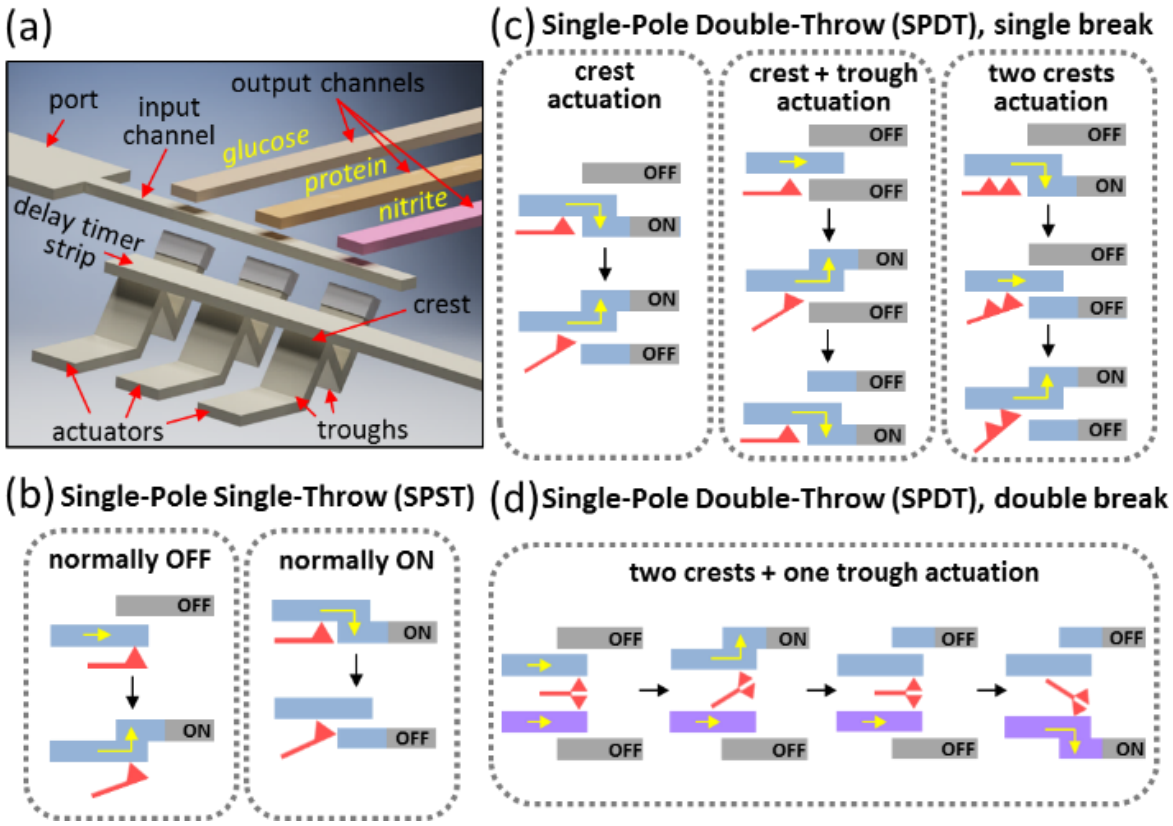

Figure 3.1 All-paper actuator is presented where physical connection from the input channel to multiple output channels is established by activating the actuator. Water is added either directly on the folds or through a delay time strip to lift (or lower) the actuator tip. (a) CAD model of the actuator-controlled fluid flow is shown. Three actuators are activated by wetting their respective folds through a delay time strip. The output channels contain dried reagents to test the presence of glucose, protein, and nitrite in the test fluid applied at the port of the input channel. Upon activating the actuators, test fluid flows into the three output channels, and a color change occurs in the three output channels indicating the presence of the analytes. (b) Schematic of the single-pole single-throw (SPST) switch is shown. In the 'normally OFF' configuration, the output channel is initially separated by a vertical distance from the input channel and there is no fluid flow to the output channel. Upon activating the actuator, the input channel makes contact with the output channel and fluid flow is established. In the 'normally ON' configuration, both the input and output channels are in contact. Upon activating the actuator, the input channel is lifted and fluid flow is blocked to the output channel. (c) Schematic of the single-pole double-throw (SPDT), single-break switch is shown. Fluid flow from one input channel to two output channels is controlled by the actuator. The 'normally OFF' and 'normally ON' switches are combined together and the vertical position of the actuator tip is controlled by wetting the crest and/or trough of the actuator's fold. (d) Schematic of the single-pole double-throw (SPDT), double-break switch is shown. Fluid flow from two input channels to two output channels is controlled by the actuator. Fluidic connections are independently established by activating the crests and troughs of the actuator's fold.

Experimental

Materials and chemicals

200 mm × 200 mm sheets of chromatography paper (Whatman™, 1 CHR) are cut using a paper trimmer (Fiskars SureCut™) to form the flow channels, actuators and delay timer strips. Single-sided tape (Scotch™) is applied at the actuator tip to block any fluid flow from the channels to the actuator. A webcam (Logitech™) is used to image the fluid front in paper. Artificial saliva is purchased from Pickering Laboratories™ and pH test paper strips are purchased from Micro Essential Laboratory. The artificial saliva is spiked with 50 mM glucose, 200 μM BSA protein, and 2000 μM nitrite. Three different colorimetric assays are realized to detect the presence of glucose, nitrite and protein in the spiked artificial saliva samples. All chemicals for the colorimetric assay are purchased from Sigma Aldrich™. Experiments are conducted at room temperature (T = 22°C).

Glucose assay:

Phosphate buffer solution (PBS, pH = 6.0) is prepared by adding sodium phosphate dibasic heptahydrate (33 mg) and potassium phosphate monobasic anhydrous (105.25 mg) in distilled water (1 mL). The PBS is stirred for 5 minutes. For every 1 mL of reagent solution, 120 units of glucose oxidase and 30 units of horseradish peroxidase are mixed into PBS. Once the two enzymes are mixed in PBS, 2.27 mg of trehalose is added that serves to stabilize the enzymes' performance and stability in the solution [57]. The dye chemical for the glucose assay is fulfilled with 99.6 mg/ml of potassium iodide and mixed for 10 minutes. For every cm^2 unit area of paper, 15 μL of the prepared reagent is applied to form the testing area. The chemical reaction is as follows: glucose is oxidized to δ-gluconolactone in the presence of glucose oxidase which is reduced to $FADH_2$ (reduced Flavin Adenine Dinucleotide). Later,

$FADH_2$ is re-oxidized to produce FAD and hydrogen peroxide. With horseradish peroxidase serving as a catalyst, the hydrogen peroxide reacts with the potassium iodide to produce a yellow-brown color.

Nitrite assay:

A mixture of 69.3 mg/mL citric acid monohydrate is prepared in methanol. Then 8.61mg/mL sulfanilamide (SA) and the dye chemical N-napthyl- ethylenediamine (NED) are added. The resultant solution is mixed for 10 minutes [58]. For every cm^2 unit area of paper, 15 µL of reagent is applied to form the testing area. The chemical reaction is as follows: nitrite is converted to nitrous acid in the presence of citric acid monohydrate and methanol. The resulting nitrous acid reacts with SA to form a diazo compound which turns colorless NED into a magenta color.

Protein assay:

The priming solution and dye reagent solution are prepared separately and applied to the testing area [59,60]. The priming solution is formed by adding 51 mg/mL of 4.0 pH citrate buffer to a solution of 8% ethanol. To lower the pH of the solution to a more acidic level (i.e. 1.8 pH), 1300 µL of 1M hydrochloric acid is added and the solution is mixed together for 5 minutes. For every cm^2 unit area of paper, 15 µL of priming solution is applied to form the testing area. The dye reagent solution consists of 8.87 mg/mL tetrabromophenol blue mixed into a solution of 95% Ethanol. The resultant is mixed for 5 minutes. For every cm^2 unit area of paper, about 15 µL of dye reagent is applied to form the testing area. The chemical reaction is as follows: the acidic media causes tetrabromophenol blue to bind with protein in the sample. Ionic bonds form between the dye and protein, and the resulting complex creates a visible color change from orange to blue.

Design of the paper actuator

The chromatography paper is cut into 30 mm × 7 mm individual strips and each strip is folded into four pieces at spacing of 7.5 mm. A load (200 mg) is placed on the folded paper strips for 5 seconds. A single sided tape is applied at the tip of the paper strip to prevent any backflow of fluid from the channels. One end of the paper strip is physically taped to a flat surface. This forms a simple actuator, and further improvisations are possible (Figure 3.1). Upon dropping a small volume of actuation fluid (i.e. water) on the crest of the folded section, the actuator is activated and its tip is raised. Conversely, wetting the trough of the folded section, the actuator tip is lowered. This principle is used to make or break the physical connection between an input channel (30 mm × 3 mm) and output channel (30 mm × 3 mm). The actuator's response time is within 1–2 seconds of wetting the crest or trough.

Theoretical model of paper actuator

At the molecular level, the cellulose of the paper is organized into bundles of crystalline and amorphous orders. As water is dropped on the actuator's fold, the water molecules penetrate in between the cellulose fibers and form a network of hydrogen bonds at the water–cellulose interface [61]. A layered structure develops along the thickness of paper where the top surface is wet and the bottom surface is dry. This produces differential swelling causing the crease to relax and the fold angle to increase until the paper saturates with water [62]. The dynamics of relaxation at the fold can be modelled as a logarithmic two-step process with a quick, transient unfolding followed by a progressive, Arrhenius-like slow relaxation [63].

We estimate of the actuation height achieved due to the wetting of the fold crease. A representative sketch of the actuator model is depicted in Figure 3.2. A single fold comprises a crest and the two troughs as labelled in Figure 3.2a. The left trough is taped in position while

the rest of the actuator is free to move. The length of each side is L and the initial fold angle at the crest is 2θ (Figure 3.2a). Upon wetting and activating the crest, the fold angle at the crest relaxes to 2α and the right trough is raised to a vertical height 'hC' given by equation (1). The unfolding of paper at the crest is illustrated in Figure 3.2b.

$$C = 2L\sin(\alpha)\sin(\alpha - \theta) \tag{3.1}$$

Upon wetting and activating the left trough, the initial fold angle at this trough (i.e. 90°+ θ) relaxes to β and the right trough is lowered to a vertical height 'hT' given by equation (2). The unfolding of paper at the left trough is shown in Figure 3.2c.

$$T = 2L\sin(\theta)\sin(\beta - \theta - \tfrac{\pi}{2}) \tag{3.2}$$

We measured the model parameters during two sets of experiments; crest activation and trough activation (n = 4 for each set using fresh actuators for each trial). The plane of the taped left trough is used as reference. The initial fold angle at the crest 2θ is 51° ± 2.5° and the initial fold angle at the left trough is 115° ± 2.9°. After dropping 4 μL of water on the crest to activate the actuator, the fold angle at the crest increases to 2α = 111.5° ± 1.7° and the right trough is raised to a height hC = 6.9 ± 0.5 mm. After wetting the left trough with 4 μL of water to activate the actuator, the fold angle at the trough increases to β = 153° ± 1.9° and the right trough is lowered to a height hT = 3.8 ± 0.2 mm. To check the validity of the proposed model, we calculated the two heights from eqn (3.1-3.2). Using L = 7.5 mm, the values obtained from the theoretical model are: hC = 6.23 mm and hT = 3.93 mm.

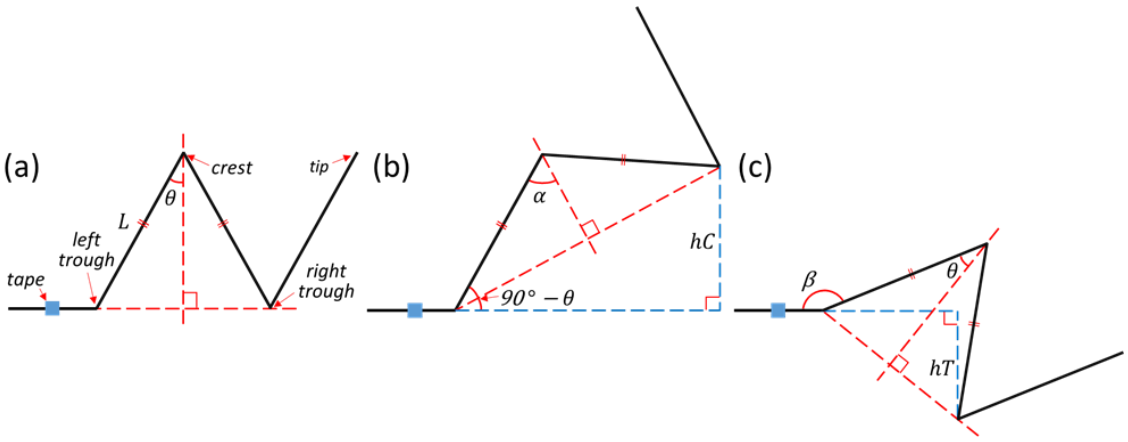

Figure 3.2 Proposed actuation model to estimate the actuation height achieved by wetting the fold. (a) Initial position of the single-fold actuator is illustrated. The crest and the two troughs are labelled. The left trough is taped and rest of the paper is free to move. The length of each side is L. The initial fold angle at the crest is 2θ. (b) After crest activation, the fold angle at the crest relaxes to 2α and the right trough is raised to a height 'hC'. (c) After activating the left trough, the initial fold angle at this trough (i.e. 90°+ θ) relaxes to β and the right trough is lowered to a height 'hT'. The expressions for the height raised (hC) and lowered (hT) are given by eqn (3.1) and (3.2), respectively.

Results and discussion

Single-Pole Single-Throw (SPST) normally OFF switch

The device comprises two channels (input channel and output channel) that are initially separated by a vertical distance (2 mm) to prevent fluid flow between the two channels. An actuator with a single fold is placed vertically below (1 mm) the input channel. The CAD model and actual device are shown in Figure 3.3a-i and Figure 3.3a-ii, respectively. Upon activating the actuator, physical contact is established between two channels, thus allowing unrestricted fluid flow from the input channel to the output channel. The switching procedure is illustrated in the left panel (Figure 3.3b, CAD model) and right panel (Figure 3.3c, actual device). Around 225 μL of blue-colored water is dropped on the port of input channel. We found that this volume (i.e. 225 μL) is sufficient to saturate the input channel. Through wicking, the input channel absorbs the blue-colored water until it is saturated with the liquid

(Figure 3.3b-i, 3.3c-i). No fluid flow is permitted in the output channel because of its physical separation from the input channel. This configuration represents the OFF state of the device. To switch the state of the device, 4 μL of red-colored water is dropped on the crest of actuator's fold. This raises the actuator tip that, in turn, lifts the edge of the input channel to make contact with the output channel (Figure 3.3b-ii, 3.3c-ii). The volume of actuation fluid used here (i.e. 4 μL) is sufficient to selectively wet the chosen crest without wetting the adjacent troughs. Thereafter, the blue-colored water flows from the input channel to the output channel (Figure 3.3b-iii, 3.3c-iii). This configuration represents the ON state of the device. Because the top surface of the actuator tip is protected with tape, there is no observable cross-contamination between the red-colored actuation fluid and blue-colored sample fluid. This is an advantage over magnetic timing valves [54] and sponge actuators [26]. The flow rate of fluid front in the two channels is imaged and plotted in Figure 3.3d.

Single-Pole Single-Throw (SPST) normally ON switch

The device comprises two channels (input channel and output channel) that are initially in physical contact, thereby allowing unrestricted fluid flow from the input to the output channel. An actuator with a single fold is placed vertically below (1 mm) the input channel. The CAD model and actual device are shown in Figure 3.4a-i and Figure 3.4a-ii, respectively. Upon activating the actuator, the tip of the input channel is lifted and physically separated (1 mm) from the output channel. This prevents any further fluid flow from the input channel to the output channel. The switching procedure is illustrated in the left panel (Figure 3.4b, CAD model) and right panel (Figure 3.4c, actual device). Around 225 μL of blue-colored water is dropped on the port of input channel. Through wicking, the input channel absorbs the blue-colored water until it is saturated with the liquid (Figure 3.4b-i, 3.4c-i). The fluid now flows

into the output channel because of the physical contact between the two channels (Figure 3.4b-ii, 3.4c-ii). This configuration represents the ON state of the device. To activate the actuator, 4 μL of red-colored water is dropped on the crest of actuator's fold. The actuator tip is raised vertically that subsequently lifts the edge of the input channel. A physical separation (1 mm) is created between the two channels that inhibit any fluid flow from the input channel to the output channel (Figure 3.4b-iii, 3.4c-iii). The flow rate of fluid front in the two channels is imaged and plotted in Figure 3.4d.

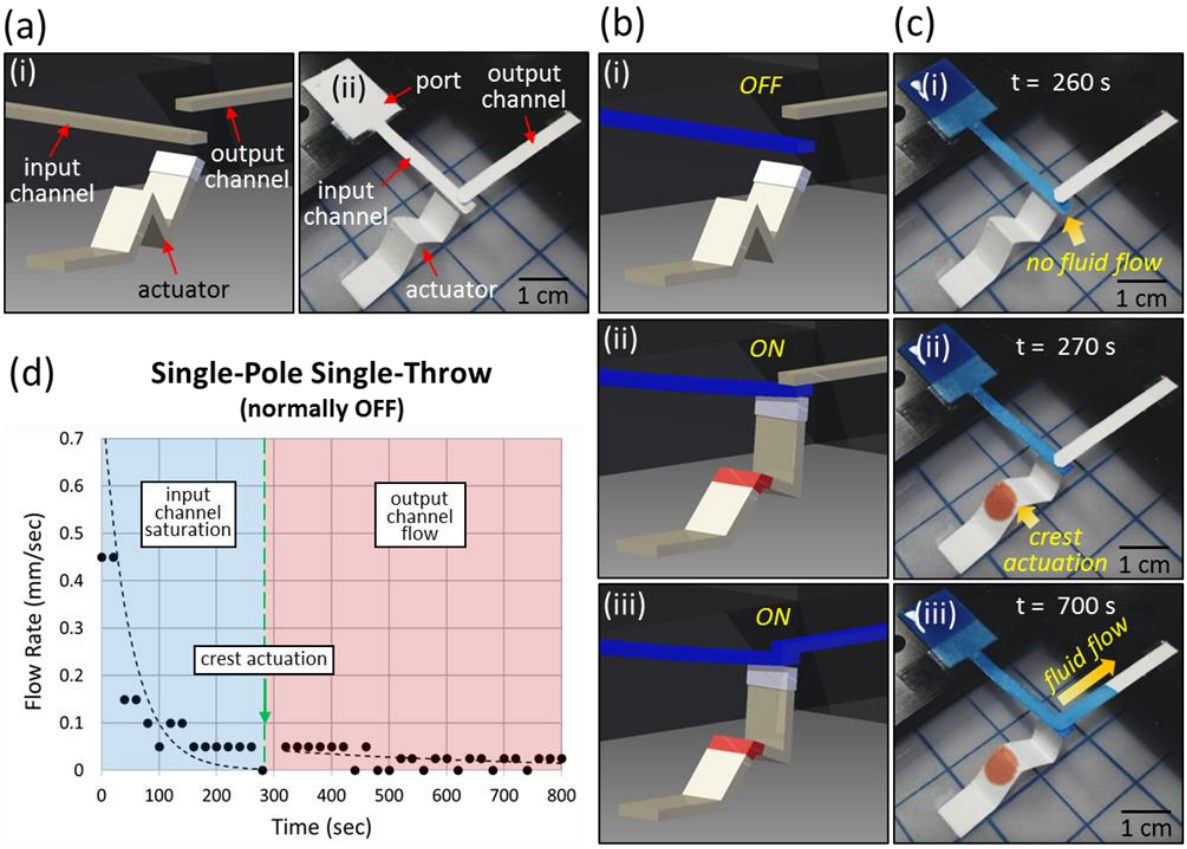

Figure 3.3 Single-pole single-throw (SPST) 'normally OFF' switch.(a) CAD model (i) and actual image (ii) of the 'normally OFF' switch are shown. The input channel is separated by a vertical distance (2 mm) from the output channel. An actuator with a single fold is placed such that its tip is positioned vertically below the edge of the input channel. (b, c) Figures in panel (b) and panel (c) show the device in CAD model and actual experiment, respectively. Blue-colored water is dropped on the port of the input channel that eventually saturates it (b-i, c-i). No fluid flow is permitted in the output channel because of its physical separation from the input channel. Red-colored water is then dropped on the crest of the actuator's fold that raises the tip and brings the input channel in contact with the output channel (b-ii, c-ii). The blue-colored water now flows into the output channel (b-iii, c-iii). (d) Flow rate of the fluid front is plotted in the input channel before actuation and in the output channel after crest actuation.

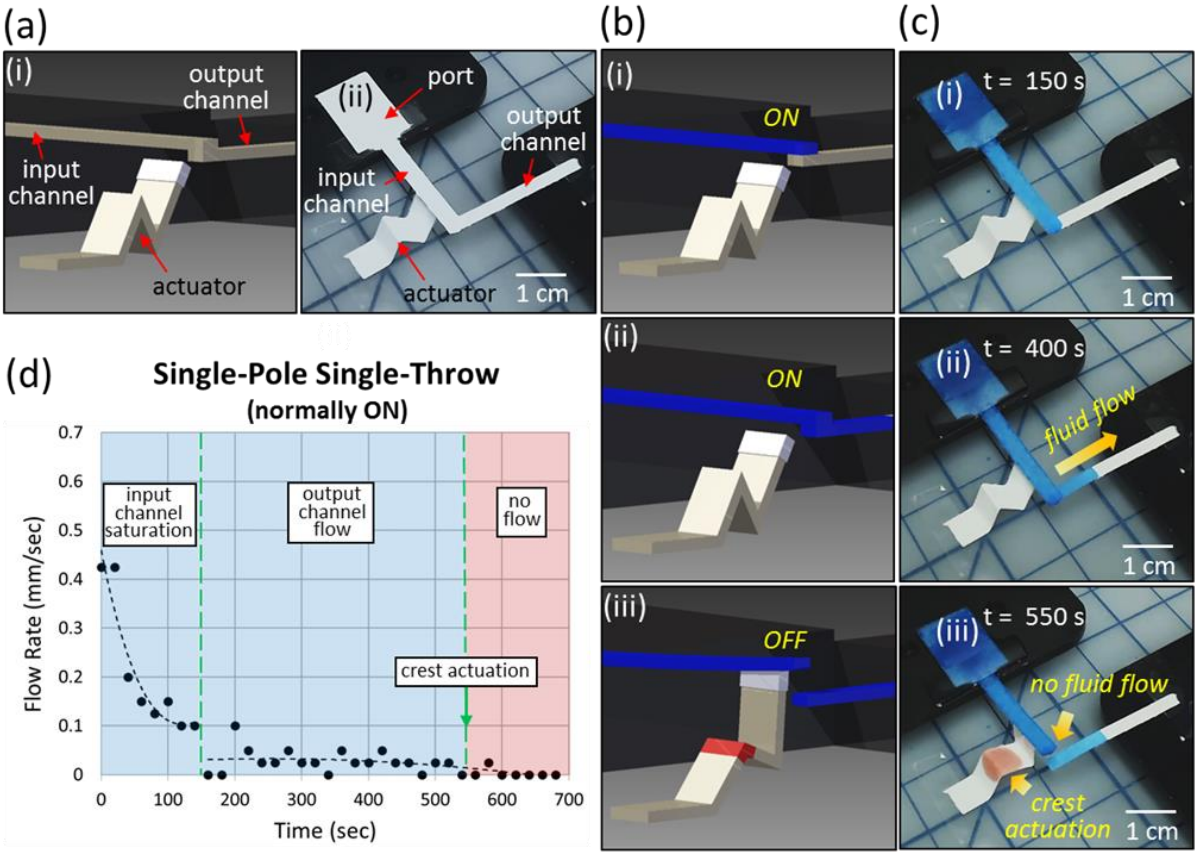

Figure 3.4 Single-pole single-throw (SPST) 'normally ON' switch. (a) CAD model (i) and actual image (ii) of the switch are shown. Initially, the input channel is in contact with the output channel and fluid flow occurs between the two channels. An actuator with a single fold is placed such that its tip is positioned vertically below the input channel. (b, c) Figures in panel (b) and panel (c) show the device in CAD model and actual experiment, respectively. Blue-colored water is dropped on the port of the input channel that eventually saturates it (b-i, c-i). Fluid flow is permitted to the output channel (b-ii, c-ii). Red-colored water is then dropped on the crest of the actuator's fold that raises the tip of the actuator and lifts the input channel to physically separate from the output channel. (b-iii, c-iii). (d) Flow rate of the fluid front is plotted in the input and output channels before actuation and in the output channel after crest actuation.

Single-Pole Double-Throw (SPDT), single-break switch

Crest actuation of a single-fold actuator

The device comprises three channels (input channel and two output channels). Initially, the input channel is in physical contact with output channel 1, thereby allowing unrestricted fluid flow from the input to the output channel 1. Output channel 2 is vertically separated (2 mm) from the input channel. An actuator with a single fold is placed vertically below (1 mm) the input channel. The CAD model and actual device are shown in Figure 3.5a-i and Figure 3.5a-ii, respectively. Upon activating the actuator, the tip of the input channel is lifted to separate from output channel 1 and make contact with output channel 2. This switches the input channel's fluid flow from output channel 1 to output channel 2. The switching procedure is illustrated in the left panel (Figure 3.5b, CAD model) and right panel (Figure 3.5c, actual device). Around 225 μL of blue-colored water is dropped on the port of input channel. Through wicking, the input channel absorbs the blue-colored water and the fluid flows into output channel 1 (Figure 3.5b-i, 3.5c-i). This configuration represents the ON state for output channel 1 and OFF state for output channel 2. To switch the fluid flow between the two output channels, the actuator is activated by dropping 4 μL of red-colored water on crest of actuator's fold (Figure 3.5b-ii, 3.5c-ii). The actuator tip lifts the edge of the input channel to separate from output channel 1 while establishing contact with output channel 2. Thereafter, the blue-colored water flows from the input channel to output channel 2 (Figure 3.5b-iii, 3.5c-iii). This configuration represents the OFF state for output channel 1 and ON state for output channel 2. The flow rate of fluid front in the three channels is plotted in Figure 3.5d.

Crest and trough actuation of a single-fold actuator

In previous examples of our toggle switches (Figure 3.3-3.5), wetting the crest of the actuator's folded section lifted its tip to regulate fluid flow from the input channel to the output channel(s). We also found that wetting the trough of the actuator's folded section lowered its tip. As shown in Figure 3.6, the choice of differential wetting of the crest or trough can be employed to turn on and switch fluid flow from the input channel to output channels. The input channel is vertically placed between the two output channels with a physically separation (1 mm) between all the channels. An actuator with a single fold is placed vertically below (1 mm) the input channel. The CAD model and actual device are shown in Figure 3.6a-i and Figure 3.6a-ii, respectively. Around 225 μL of blue-colored water is dropped on the port of input channel. Through wicking, the input channel absorbs the blue-colored water but there is no fluid flow into the output channels (Figure 3.6b-i, 3.6c-i). This configuration represents the OFF state for both the output channels. By dropping 4 μL of red-colored water on the crest of the actuator's fold, the tip is lifted to establish contact between the input channel and output channel 1 (Figure 3.6b-ii, 3.6c-ii). This configuration represents the ON state for output channel 1 and OFF state for output channel 2. By dropping another 4 μL of red-colored water on the right trough of the actuator's fold, the tip drops down and the input channel makes contact with the output channel 2 placed vertically below it. Fluid flows from the input channel to output channel 2 (Figure 3.6b-iii, 3.6c-iii). This configuration represents the OFF state for output channel 1 and ON state for output channel 2. The flow rate of fluid front in the three channels is plotted in Figure 3.6d.

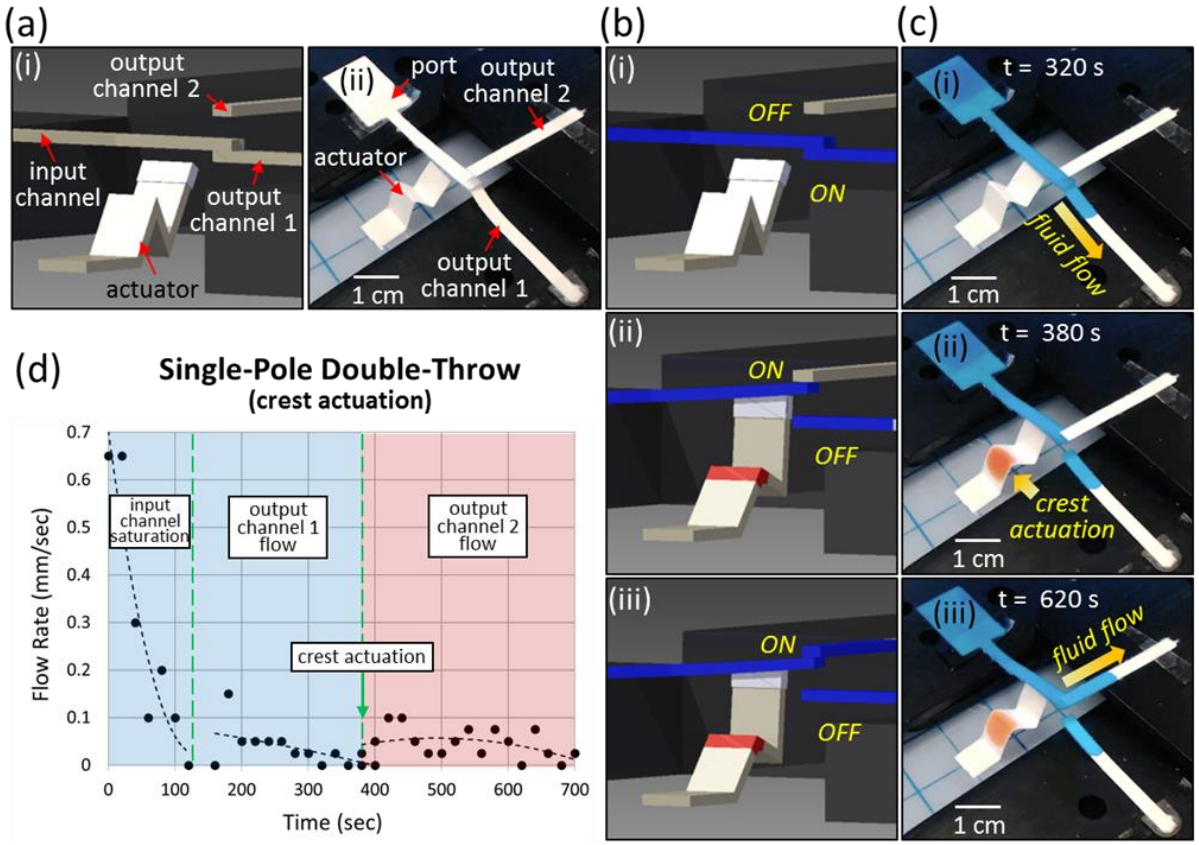

Figure 3.5 Single-pole double-throw (SPDT), single-break switch with crest actuation. (a) CAD model (i) and actual image (ii) of the switch are shown. Initially, the input channel is in contact with output channel 1 while output channel 2 is vertically separated from them. An actuator with a single fold is placed such that its tip is positioned vertically below the input channel. (b, c) Figures in panel (b) and panel (c) show the device in CAD model and actual experiment, respectively. Blue-colored water is dropped on the port of the input channel that eventually saturates it and flow is permitted to output channel 1 (b-i, c-i). Red-colored water is then dropped on the crest of the actuator's fold that raises the actuator tip and lifts the input channel to physically separate from output channel 1 and touch output channel 2 (b-ii, c-ii). Fluid flow is now established in output channel 2 (b-iii, c-iii). (d) Flow rate of the fluid front is plotted in the input and output channel 1 before actuation and in the output channel 2 after crest actuation.

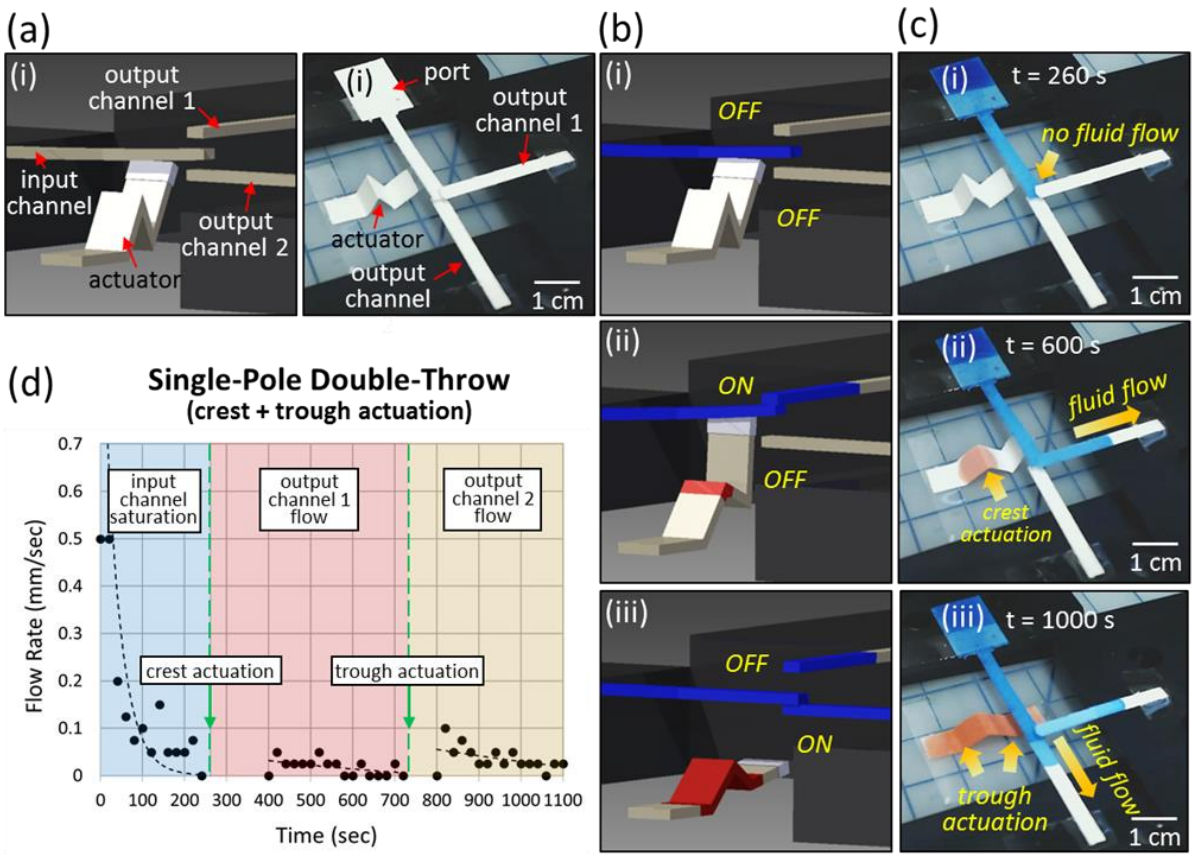

Figure 3.6 Single-pole double-throw (SPDT), single-break switch with crest and trough actuation. (a) CAD model (i) and actual image (ii) of the switch are shown. Initially, the input channel is placed in between the two output channels and vertically separated from them. An actuator with a single fold is placed such that its tip is positioned vertically below the input channel. (b, c) Figures in panel (b) and panel (c) show the device in CAD model and actual experiment, respectively. Blue-colored water is dropped on the port of the input channel that eventually saturates it (b-i, c-i). No fluid flow is permitted in the two output channels because of their physical separation from the input channel. Red-colored water is then dropped on the crest of the actuator's fold that raises its tip and brings the input channel in contact with output channel 1 and the blue-colored water now flows into this output channel (b-ii, c-ii). Another round of red-colored water is dropped near the trough of the actuator's fold that lowers the actuator tip and brings the input channel in contact with output channel 2 (b-iii, c-iii). (d) Flow rate of the fluid front is plotted in the input channel before actuation, in output channel 1 after crest actuation, and in output channel 2 after trough actuation.

Two crests' actuation of a multiple-fold actuator

The basic concept of raising the actuator tip by wetting the crest is extended to structures having multiple folds where flow between vertically-aligned channels is controlled by the sequential wetting of individual folds. Figure 3.7 demonstrates the switching procedure where the left panel (Figure 3.7a) and right panel (Figure 3.7b) represent images from the CAD model and actual device, respectively. Initially, the input channel is placed in contact with output channel 1 while output channel 2 is separated by a vertical distance (4 mm) from them. An actuator with two folds is placed vertically below (1 mm) the input channel. Around 225 μL of blue-colored water is dropped on the port of input channel. Through wicking, the input channel absorbs the blue-colored water and flows into output channel 1 (Figure 3.7a-i, 3.7b-i). This configuration represents the ON state for output channel 1 and OFF state for output channel 2. The actuator is activated by dropping 4 μL of red-colored water on the crest section of its left fold. This raises the actuator tip and dislodges the input channel from output channel 1. In this configuration, both output channels are in the OFF state (Figure 3.7a-ii, 3.7b-ii). By dropping another 4 μL of red-colored water on the crest section of the actuator's right fold, the actuator tip lifts up and forces the input channel to make contact with output channel 2 placed vertically above it (Figure 3.7a-iii, 3.7b-iii). At this instance, fluid flows from the input channel to output channel 2 (Figure 7a-iv, 7b-iv). This configuration represents the OFF state for output channel 1 and ON state for output channel 2.

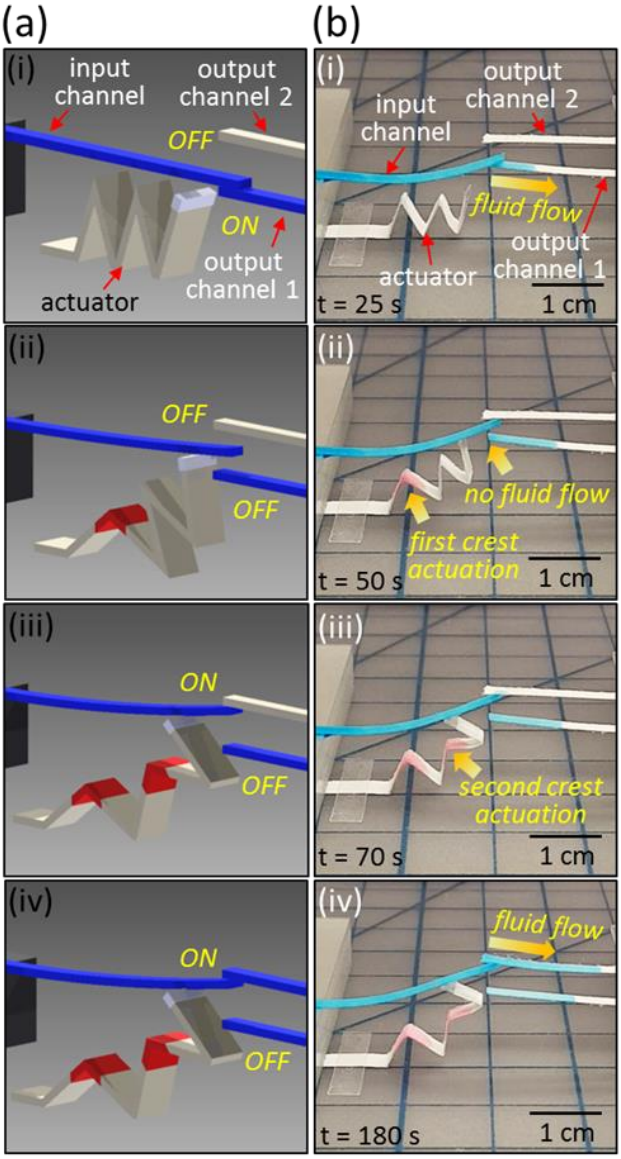

Figure 3.7 Single-pole double-throw (SPDT), single-break switch with actuation of two crests. (a, b) Figures in panel (a) and panel (b) depict the device in CAD model and actual experiment, respectively. Initially, the input channel touches output channel 1 but is vertically separated from output channel 2. An actuator with two folds is placed such that its tip is positioned vertically below the input channel. Blue-colored water is dropped on the port of the input channel that eventually saturates it and flow is permitted to output channel 1 (a-i, b-i). Red-colored water is then dropped on the crest of the actuator's left fold that raises the actuator tip and lifts the input channel to physically separate from output channel 1 (a-ii, b-ii). Another round of red-colored water is dropped on the crest of the actuator's right fold that brings the input channel in contact with output channel 2 (a-iii, b-iii). Fluid flow is now established into output channel 2 (a-iv, b-iv).

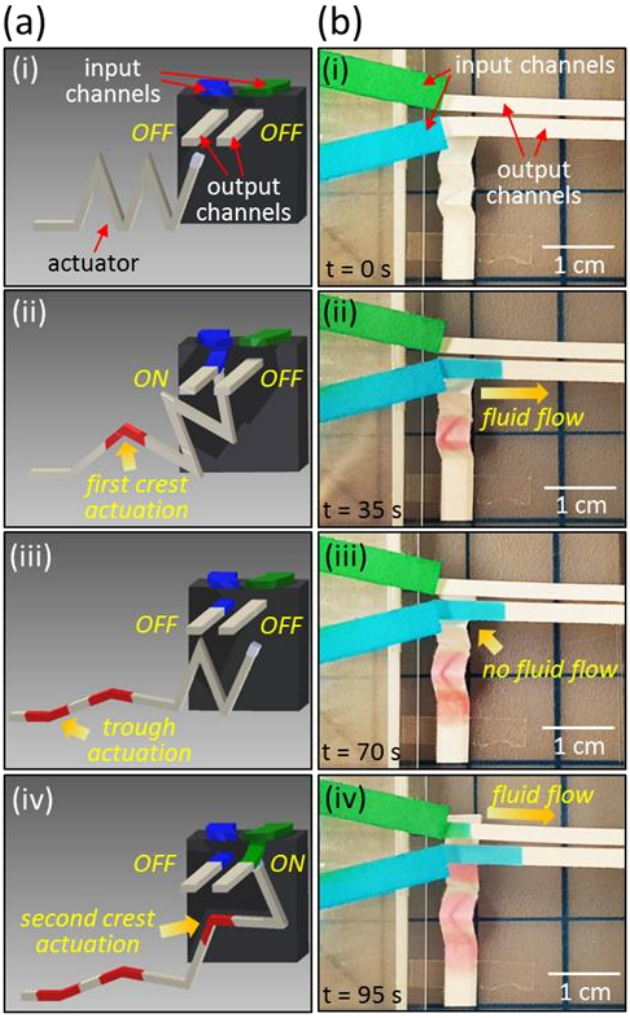

Figure 3.8 Single-pole double-throw (SPDT), double-break switch to control two pairs of input and output channels. (a, b) Figures in panel (a) and panel (b) depict the device in CAD model and actual experiment, respectively. Initially, two input channels are placed vertically above their respective output channels but are vertically separated from their output channels. An actuator with two folds is placed such that its tip is positioned vertically below the left input channel. Blue-colored and green-colored water are dropped on the ports of the two input channels which eventually saturate them. Fluid flow is blocked to the output channels (a-i, b-i). Red-colored water is then dropped on the crest of the actuator's left fold that raises the actuator tip and lifts the (left) input channel to touch the (left) output channel (a-ii, b-ii). Another round of red-colored water is dropped on the trough of the actuator's left fold that lowers the tip and removes the previously established connection (a-iii, b-iii). Final round of red-colored water dropped on the crest of the actuator's right fold brings the (right) input channel in contact with the (right) output channel (a-iv, b-iv).

Single-Pole Double-Throw (SPDT), double-break switch

The device comprises four channels (two input channels and two output channels). Initially, both input channels are placed above their respective output channels and separated by a horizontal distance (2 mm). An actuator with two folds is placed vertically below (1 mm) the left input channel. Figure 3.8 demonstrates the switching procedure where the left panel (Figure 3.8a) and right panel (Figure 3.8b) represent images from the CAD model and actual device, respectively. Around 225 μL of blue-colored water and 225 μL of green-colored water are dropped on ports of the two input channels. Through wicking, the input channels absorb the colored water but both output channels are in the OFF state due to the physical separation from their respective input channels (Figure 3.8a-i, 3.8b-i). Next, 4 μL of red-colored water is dropped on the crest section of the left fold which lifts the actuator tip and brings the blue-colored input channel in contact with its output channel (Figure 3.8a-ii, 3.8b-ii). Another 4 μL of red-colored water is dropped on the trough of the left fold which causes the actuator tip to drop and dislodge from the blue-colored output channel (Figure 3.8a-iii, 3.8b-iii). In this configuration, both output channels are in the OFF state. By dropping 4 μL of red-colored water on the crest of the right fold, the tip is raised. This engages the green-colored input channel to its output channel and enables fluid flow at the juncture (Figure 3.8a-iv, 3.8b-iv).

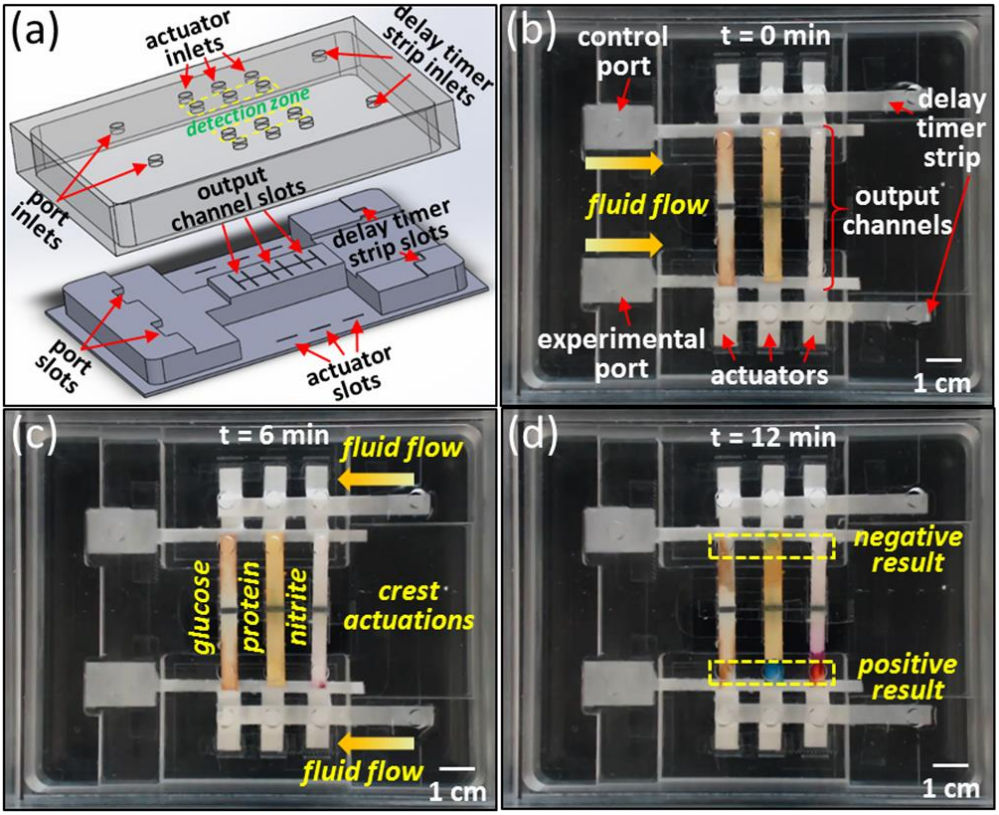

Figure 3.9 Colorimetric assay for the simultaneous detection of glucose, protein, and nitrite from artificial saliva. (a) The two-part mold design for the enclosure setup consists of a base and a cover. The base contains slots to place the two input channels, six output channels, six actuators, and two delay timer strips. The cover contains inlets to drop the test and control samples, three reagents, and actuation fluid. The output channels are wicked with the three reagents and dried at room temperature. The channels, actuators, and delay timer strips are taped in their respective slots. (b) Artificial saliva spiked with analytes is dropped on the experimental port while unspiked artificial saliva is used at the control port. By wicking, fluid flows and saturates the two input channels. (c) After a pre-defined delay, distilled water is dropped on the delay time strips. As water travels through a timer strip, the crests of three actuators are activated to raise their respective tips. Thereafter, the experimental fluid flows into the bottom three output channels while the control fluid flows into the top three output channels. (d) A positive color change is confirmed for the experimental case indicating the presence of glucose, protein, and nitrite. A negative color change is shown in the control case.

Simultaneous detection of glucose, protein, and nitrite from artificial saliva

As a proof-of-concept application, we demonstrate a functional assay to detect the presence of three analytes (i.e. glucose, nitrite, and protein) in artificial saliva. A delay timer strip controls the wetting of three actuators, thereby enabling fluid flow from the input channel to three output channels. Two parallel tests (i.e. control and experimental) are conducted in the assay. A Plexiglas enclosure setup is constructed to hold the paper strips and provide access points to the user (Figure 3.9a). The base of the enclosure (11 cm × 13.5 cm × 1.6 cm) contains slots to hold the two input channels (i.e. control and experimental inputs) and six output channels (i.e. one pair each of three test strips). In addition, there are slots for six actuators where each actuator connects an input channel to three output channels. For timed programming of actuation, two delay timer strips are used that activate the two sets of three actuators. The cover of the enclosure contains access holes to drop fluid sample and reagents on the respective paper strips.

The output channels are saturated with the three test reagents and allowed to dry at room temperature. One end of all the paper strips (i.e. channels, actuators, and delay timer strips) is taped in their allocated slots. Spiked artificial saliva (250 µL) is dropped in the experimental port while unspiked artificial saliva (250 µL) is used in the control port. By wicking, fluid flows in the two input channels until saturation which takes around 6 minutes (Figure 3.9b). Thereafter, distilled water is dropped on the ports of the two delay timer strips (Figure 3.9c). The actual delay and flow rate in the timer strips can be manipulated by their geometry and surface chemistry. As water travels through a timer strip, the three actuator crests are wetted and activated which, in turn, lifts the input channel to make contact with the three output channels. After chemical reactions occur in the reagent strips, color changes are

observed in the detection zones (Figure 3.9d). The positive color changes indicate the presence of analytes in spiked artificial saliva. Control test strips do not show the intended color change.

In another application, we demonstrate the use of paper actuators with fluidic systems incorporating user-defined delays. A motorized droplet actuation system [64] controls the movement of three discrete droplets (15 µL) on hydrophilic symbols printed on a super-hydrophobic plastic sheet. Each droplet has a distinct pH value (pH = 8.0, pH = 5.5, and pH = 7.0 (control)). Three pH test paper strips are placed next to the motorized actuation system and supported by three SPST (normally OFF) switches. Upon tilting the stage of the motorized actuation system in sequential steps, each droplet reaches its respective pH test paper strip and is absorbed by actuating the trough of the paper actuator. The time delays in droplet movement and absorption in the pH test paper strip are controlled by the motorized actuation system and paper-based switches, respectively. The produced color changes of the pH test paper strips are compared with the manufacturer's reference table to infer the droplets' pH levels.

Conclusion

We demonstrated a reconfigurable actuator device for paper microfluidics to regulate fluid flow between input channel(s) and output channel(s). The actuator is made of paper and requires no extra fabrication steps, coatings, materials or electrical/magnetic stimulation. The actuation principle relies on selectively wetting the crease of a previously-folded paper strip which, in turn, relaxes the crease and increases its fold angle. The actuation height achieved by wetting the crest and trough of the actuator's fold is measured to be 6.9 ± 0.5 mm and 3.8 ± 0.2 mm, respectively. The actuator's response time is within 2 seconds of wetting. A number of switch configurations are realized using the folded paper actuator, such as single-pole single-throw (normally OFF and normally ON) and single-pole double-throw (with single and double break). A colorimetric assay is presented where the presence of glucose, protein, and

nitrite are detected in spiked artificial saliva. The assay integrates the parallel operations of multiple actuators, delay timer strips, and flow channels in a portable enclosure. The advantages of this actuation method include easy preparation steps by paper cutting and folding, very fast actuator response time, choice between different switch configurations, no observable contamination of the flow channels by the actuation fluid, ability to integrate and scale multiple actuators, and significantly reduced cost of materials and labor.

Acknowledgements

This work is partially supported by the U.S. National Science Foundation (NSF IDBR-1556370 and NSF CBET-1150867). In addition, Taejoon Kong is partially supported by the Defense Threat Reduction Agency (HDTRA1-15-1-0053).

References

1 W. Martinez, S. T. Phillips, M. J. Butte and G. M. Whitesides, Angew. Chem., Int. Ed., 2007, 46, 1318–1320.

2 W. Martinez, S. T. Phillips and G. M. Whitesides, Proc. Natl. Acad. Sci., 2008, 105, 19606–19611.

3 W. Martinez, S. T. Phillips, Z. Nie, C.-M. Cheng, E. Carrilho, B. J. Wiley and G. M. Whitesides, Lab Chip, 2010, 10, 2499–2504.

4 W. Martinez, S. T. Phillips, G. M. Whitesides and E. Carrilho, Anal. Chem., 2010, 82, 3–10.

5 Li, W. Zhang, L. Chen and B. Lin, Electrophoresis, 2013, 34, 2162–2168.

6 K. Yetisen, M. S. Akram and C. R. Lowe, Lab Chip, 2013, 13, 2210–2251.

7 R. Park, Lateral-flow POC tests to grow, http://ivdtechnology. com/article/lateral-flow-poc-tests-grow, (accessed June 2013).

8 G. A. Posthuma-Trumpie, J. Korf and A. Amerongen, Anal. Bioanal. Chem., 2009, 393, 569–582.

9 R. Wong and H. Tse, Lateral Flow Immunoassay, Humana Press, Totowa, NJ, 2009.

10 T. Acharya, A. S. Daar, E. Dowdeswell, P. A. Singer and H. Thorsteinsdottir, Genomics and Global Health, University of Toronto Joint Centre for Bioethics, Toronto, Ontario, Canada, 2004.

11 Water Quality for Ecosystem and Human Health, GEMS/ Water Programme Office, UN, Burlington, Ontario, Canada, 2008.

12 Global Strategy for Food Safety: Safer Food for Better Health, F. S. Department, Food Safety Department, WHO, Geneva, Switzerland, 2002.

13 Foodborne Disease Outbreaks: Guidelines for Investigation and Control, WHO, France, 2008.

14 J. Saldanha, A. Parashar, S. Pandey and J. Powell-Coffman, Toxicological Sciences, 2013, 135(1), 156–168.

15 A. Beeman, Z. Njus, S. Pandey and G. Tylka, Phytopathology, 2016, 106(12), 1563–1571.

16 E. Fu and C. Downs, Lab Chip, 2017, 17, 614–628.

17 X. Li, D. R. Ballerini and W. Shen, Biomicrofluidics, 2012, 6, 11301–1130113.

18 D. R. Ballerini, X. Li and W. Shen, Microfluid. Nanofluid., 2012, 13, 769–787.

19 D. D. Liana, B. Raguse, J. J. Gooding and E. Chow, Sensors, 2012, 12, 11505–11526.

20 C. Parolo and A. Merkoci, Chem. Soc. Rev., 2013, 42, 450–457.

21 P. Shah, X. Zhu and C. Z. Li, Expert Rev. Mol. Diagn., 2013, 13, 83–91.

22 T. Kong, R. Brien, Z. Njus, U. Kalwa and S. Pandey, Lab Chip, 2016, 16(10), 1861-1872.

23 In vitro Diagnostics (IVD) Market (Applications, End-users & Types) Trends & Global Forecasts (Major & Emerging Markets - G7, Japan & BRIC), Markets and Markets, 2011.

24 J. Marchant, Innovations in Diagnostics (Next Generation Molecular & Point of Care Diagnostics Driving Personalised Healthcare), Business Insights Ltd, 2006.

25 E. Fu, P. Yager, P. N. Floriano, N. Christodoulides and J. Mcdevitt, IEEE Pulse, 2011, 2, 40–50.

26 B. J. Toley, J. A. Wang, M. Gupta, J. R. Buser, L. K. Lafleur, B. R. Lutz, E. Fu and P. Yager, Lab Chip, 2015, 15, 1432–1444.

27 J. Carr, R. Lycke, A. Parashar and S. Pandey, Appl. Phys. Lett., 2011, 98(14), 143701.

28 S. Pandey, A. Joseph, R. Lycke and A. Parashar, Advances in Bioscience and Biotechnology, 2011, 2, 409–415.

29 R. Lycke, A. Parashar and S. Pandey, Biomicrofluidics, 2013, 7(6), 064103.

30 K. N. Han, J. S. Choi and J. Kwon, Sci. Rep., 2016, 6, 25710.

31 B. D. Grant, C. A. Smith, K. Karvonen and R. Richards-Kortum, Anal. Chem., 2016, 88, 2553–2557.

32 S. Ramachandran, E. Fu, B. Lutz and P. Yager, Analyst, 2014, 139, 1456–1462.

33 J. Saldanha, S. Pandey and J. Powell-Coffman, Life Sciences in Space Research, 2016, 10, 38–46.

34 R. Gerbers, W. Foellscher, H. Chen, C. Anagnostopoulos and M. Faghri, Lab Chip, 2014, 14, 4042–4049.

35 E. W. Washburn, Phys. Rev., 1921, 17, 273–283.

36 R. Lucas, Kolloid-Z., 1918, 23, 15–22.

37 S. Mendez, E. M. Fenton, G. R. Gallegos, D. N. Petsev, S. S. Sibbett, H. A. Stone, Y. Zhang and G. P. Lopez, Langmuir, 2010, 26, 1380–1385.

38 E. Fu, B. Lutz, P. Kauffman and P. Yager, Lab Chip, 2010, 10, 918–920.

39 A. C. Glavan, R. V. Martinez, E. J. Maxwell, A. B. Subramaniam, R. M. D. Nunes, S. Soh and G. M. Whitesides, Lab Chip, 2013, 13, 2922–2930.

40 C. Renault, X. Li, S. E. Fosdick and R. M. Crooks, Anal. Chem., 2013, 85, 7976–7979.

41 D. L. Giokas, G. Z. Tsogas and A. G. Vlessidis, Anal. Chem., 2014, 86, 6202–6207.

42 H. Noh and S. T. Phillips, Anal. Chem., 2010, 82, 8071–8078.

43 C. H. Weng, M. Y. Chen, C. H. Shen and R. J. Yang, Biomicrofluidics, 2014, 8, 066502.

44 B. Lutz, T. Liang, E. Fu, S. Ramachandran, P. Kauffman and P. Yager, Lab Chip, 2013, 13, 2840–2847.

45 B. J. Toley, B. McKenzie, T. Liang, J. R. Buser, P. Yager and E. Fu, Anal. Chem., 2013, 85, 11545–11552.

46 E. Fu, T. Liang, P. Spicar-Mihalic, J. Houghtaling, S. Ramachandran and P. Yager, Anal. Chem., 2012, 84, 4574–4579.

47 K. N. Han, J. S. Choi and J. Kwon, Sci. Rep., 2016, 6, 25710.

48 C. Koo, F. He and S. Nugen, Analyst, 2013, 138, 4998–5004.

49 L. F. Cai, M. H. Zhong, H. L. Li, C. X. Xu and B. Y. Yuan, Biomicrofluidics, 2015, 9, 046503.

50 Y. Jiang, Z. X. Hao, Q. H. He and H. W. Chen, RSC Adv., 2016, 6, 2888–2894.

51 L. K. Lafleur, J. D. Bishop, E. K. Heiniger, R. P. Gallagher, M. D. Wheeler, P. Kauffman, X. H. Zhang, E. C. Kline, J. R. Buser, S. Kumar, S. A. Byrnes, N. M. J. Vermeulen, N. K. Scarr, Y. Belousov, W. Mahoney, B. J. Toley, P. D. Ladd, B. R. Lutz and P. Yager, Lab Chip, 2016, 16, 3777–3787.

52 J. Houghtaling, T. Liang, G. Thiessen and E. Fu, Anal. Chem., 2013, 85, 11201–11204.

53 B. R. Lutz, P. Trinh, C. Ball, E. Fu and P. Yager, Lab Chip, 2011, 11, 4274–4278.

54 X. Li, P. Zwanenburg and X. Liu, Lab Chip, 2013, 13, 2609–2614.

55 H. Liu and R. M. Crooks, J. Am. Chem. Soc.,2011, 133, 17564–17566.

56 W. Liu, C. L. Cassano, X. Xu and Z. H. Fan, Anal. Chem.,2013, 85, 10270–10276.

57 K. J. Paz-Alfaroa, Y. G. Ruiz-Granadosb, S. Uribe-Carvajalb and J. G. Sampedro, Journal of Biotechnology, 2009, 141, 130-136.

58 J. Sun, X. Zhang, M. Broderick and H. Fein, Sensors, 2003, 3, 276-284.

59 M. M. Bradford, Analytical Biochemistry, 1976, 72, 248-254.

60 B. B. Kim, H. A. Kadir and S. Tayyab, Pakistan Journal of Biological Sciences, 2008, 11(20), 2418-2422.

61 A. C. Khazraji and S. Robert, Journal of Nanomaterials, 2013, 2013, Article ID 409676.

62 E. Reyssat and L. Mahadevan, EPL Journal, 2011, 93, 54001.

63 B. Thiria and M. Adda-Bedia, Physical Review Letters, 2011, 107, 025506.

64 T. Kong, R. Brien, Z. Njus, U. Kalwa and S. Pandey, Lab Chip, 2016, 16, 1861.

CHAPTER 4.

MICROFLUIDIC CONTROL OF CRISPR-dCAS9 EXPRESSION TO IDENTIFY SUBTLE PHENOTYPES ASSOCIATED WITH NOVEL GENES IN CELL DIVISION

Abstract

The emergence of bacterial resistance to available antibiotics is a well-recognized problem to the health and well-being of our society. As we need to discover new and better antibiotics to combat resistant bacteria, there is a search for engineered platforms that can rapidly test and evaluate the effectiveness of test antibiotics to bacterial cultures. An ideal assay to detect antibiotic resistance should be low-cost, easy-to-fabricate and easy-to-use with high throughput and resolution. Here we designed a microfluidic device that attempts to incorporate the features mentioned previously. The non-polymeric chip design avoids much of the fabrication complexities of silicon and polymeric devices, while still allowing us to observe bacterial populations at single-cell and population levels. The incorporation of agarose membrane as the resting substrate, along with a temperature controlled chamber, allows us to grow the cells for over 10 hours with automatic recording of bacterial growth or inhibition. The morphological changes in the bacterial cells upon application of an antibiotic, ampicillin, have been characterized from the recorded images which reveals the minimum inhibitory concentration. Finally, the device has been used to test the effectiveness of a gene-editing technique in controlling cell division.

Introduction

Bacteria are being exposed to elevated amounts of antibiotics to combat diseases in humans and livestock, which has resulted in their increased tolerance to available antibiotics. Antimicrobial resistance (AMR) or the increased inefficiency of antibiotics in killing bacterial pathogens is an alarming threat to global public health [1-3]. The prevalence of antibiotic resistance is accelerated by the human activities like the abuse or misuse of antibiotics, a practice which also increases the cost for treatment [3]. It is estimated that 10 million people in the world will die of bacterial disease by 2050 as a result of AMR [1, 2]. While is difficult to stop the evolution of bacteria and tailor existing antibiotics from losing its ability to disable a function of the cell, an effective antibiotic regiment and its proper dosage needs to be prescribed to treat infectious bacteria [2, 4-6]. To accomplish this task, there is a need to develop platforms to quickly discern antibiotic susceptibility that characterize and identify bacterial sensitivities to known and unknown antibiotic treatments [1, 5, 7, 8]. The conventional method to test the effectiveness of antibiotics on bacterial colonies involves the use of plate assays (typically 3-inch plates with a layer of agarose gel over which bacterial colonies are incubated) that employ diffusion and dilution methods, along with manual scoring of bacterial growth. Unfortunately, plate assays require considerable human effort and a large amount of chemical and biological resources, thereby making it formidable to test many experimental conditions [2, 3, 7-10].

To address the problem of low throughput in plate assays, microfluidics has come to the forefront as an enabling technology where the user can accurately control the chemical microenvironment around bacterial cells [11-14]. Microfluidic devices reduce the amount of chemical and biological resource, decrease the incubation times for observable cell growth, provide continuous and accurate screening at the single cell level, and offer high-throughput

analysis [3, 11, 15, 16]. However, there are physical limits to the number of chemical inputs available for a single test. Although existing microfluidic systems have improved antibiotic susceptibility testing, they still have some inherent issues in commercializing the technology for mass production and usage. For example, most microfluidic chips are made using PDMS which is an expensive polymer, especially for mass production [3, 17-20]. The bacterial cells cultured inside microfluidic channels may be subjected to shear stress and deformation [11-13, 21]. Long-term monitoring of bacterial growth has not been reported in the literature (typically less than 6 hours) because of problems with fluid evaporation and cell viability. In addition, the fabrication process to create silicon wafer molds increases the complexity and cost of microfluidics for AMR testing.

There is a need to design microfluidic devices to monitor bacterial behavior and gene expression without requiring silicon-based fabrication steps [2, 22, 23]. Here we develop a novel microfluidic chip made from double-sided tape and transparency film, eliminating the micromachining steps of lithography, spin-coating, and etching. Our device consists of a glass substrate, double-sided tape, transparency film, an agarose membrane, and coverslips. The agarose membrane is patterned to create extruding surfaces that function to separate the bacterial colonies. The bacterial cells are cultured on these agarose membrane surfaces and absorb the liquid solution through the permeable agarose membrane. The configuration of our system enables us to establish a concentration gradient by harnessing the diffusion characteristics of the porous hydrogel. Such a design allows for observation of the morphological changes in the bacteria over a long time (~2 days).

To accommodate long-term experiments where bacterial colonies are imaged at single-cell level, the user needs to perform regular adjustment of the microscope's focus. If not, the

bacterial cells may go out of focus, resulting blurred images. The focal plane can change as a result of the weight of the microscope and environmental conditions such as humidity, temperature, and substrate type. To overcome this cumbersome manual microscope adjustment, we implemented a software-based autofocusing system. The autofocusing feature is designed to reduce manual intervention, while generating high-quality videos of bacterial growth over extended time periods. Our autofocusing feature employs image processing algorithms to monitor the image quality and adjust the microscope (by an attached motor) to reflect any changes to the focal plane location. By adjusting the depth map (the distance between the objects and the optical lens) object focus can be maintained under these conditions.

In this chapter, we describe our double-sided tape based microfluidic system to successfully observe bacterial growth and phenotypic changes under different chemical conditions. The morphological changes in bacterial cells are characterized to deduce the minimum inhibitory concentration (MIC) value of a common antibiotic, ampicillin. The system has then been used to implement some steps of a popular gene editing technique (i.e. Clustered Regularly Interspaced Short Palindromic Repeats interference) at the single cell level. We believe the application of our system in gene editing is promising and can reveal new insights into bacterial physiology through precise modulation of gene expression.

Material and Method

Chemicals and equipment

Tryptone, yeast extract, NaCl and fluorescein (M.W. 332 mol^{-1}) are purchased from Sigma-Aldrich. Lysogeny broth (10 g of Tryptone, 5 g of Yeast extract, 10 g of NaCl and deionized water for the total volume of 1 L) is prepared for cell culture and the experiments. A polydimethylsiloxane (PDMS) pre-polymer and a curing agent are obtained from Dow Corning. A high melting temperature agarose is purchased from Alfa Aesar™. A student

microscope (Leica™ DM 500), a stereo fluorescent microscope (Leica™ MZ 16) with a 470 nm GFP filter cube, an external light source (Leica™ EL 6000), and a CCD camera (QImaging™ QICAM Fast 1394) are employed for the imaging system. The temperature controller (TC-1-100s), heating plate, and an objective heater are purchased from Bioscience Tools. The microscope chamber is designed using AutoCAD™ and manufactured by Country Plastics. A fan heater (INCUKIT™) is purchased from Incubator Warehouse. The syringe pump is obtained from KD Scientific Inc.

Sample preparation

An *Escherichia coli* K12 MG1655 derivative strain (BW30270), containing a chromosomally integrated dCas9 gene under the control of a tetracycline inducible promoter and a single-guide RNA gene constitutively expressed from a colE1-like plasmid, was obtained from the laboratory of Dr. Greg Phillips (College of Veterinary Medicine, Iowa State University). A single colony was selected to inoculate 5mL of LB broth (Fisher Scientific™) in a sterile culture tube and incubated at 37 °C for 12-18 hours with shaking at 250 r.p.m by benchtop incubator (Corning™). After incubation, 100 µL of *E. coli* was extracted from the tube and diluted in 5 mL of LB broth in a 15mL culture tube (1:50 ratio). The tube was mixed thoroughly by vortex and incubated again at 37 °C with agitation for 2 hours for maintenance of healthy cells. The bacterial sample was then logarithmically diluted prior to being used in the experiments.

Microfluidic device design and fabrication

The microfluidic device has three separate layers: a glass slide (Fisher Scientific™), a double-sided tape (3M™) and a transparency film (Staples Inc.™) (Figure 4.1a). The microfluidic channels are drawn in Silhouette Studio and Silhouette cutting machine cuts the double sided tape along the line of the design to create the channels of engraving pattern

(Figure 4.1c). The cut tape is attached to a glass slide and covered by a transparency film containing the input, output, and fluidic holes (Figure 4.1b). The channel width is 0.76 mm and the dimension of each fluidic hole, placed on a top of the channel, is 0.76 mm x 1.5 mm. Solidified PDMS is punched with a 4 mm biopsy punch (HealthLink^{TM}) and each cylindrical PDMS piece is further punched with a 1.5 mm dispensing needle (Howard Electronic Instrument Inc.) to create input ports. The fluidic connectors are placed on top of the inlet and outlet, and 5 µL of liquid PDMS was poured on the edge of the connectors. Later, the chip is baked for 5 hours on a hotplate at 80 °C to fix the connectors and remove the air gap between each layer to create strong bonding. The microfluidic device is stored in a Petri dish and sterilized prior to performing an experiment.

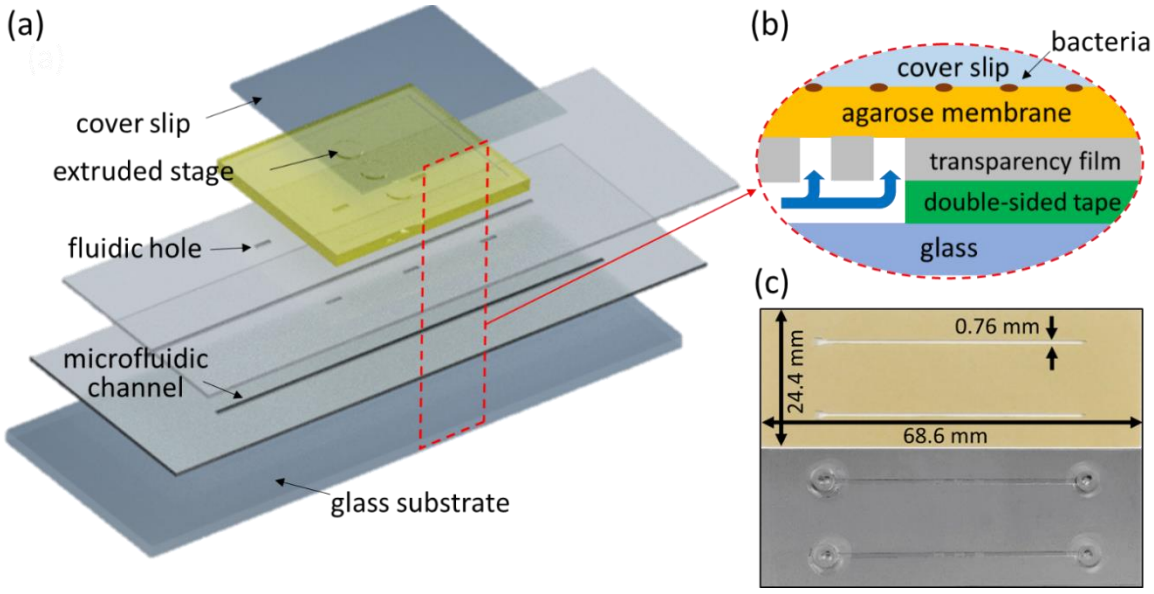

Figure 4.1 Schematic illustration of the 3D microfluidic device (a) The microfluidic chip comprised glass substrate, double-sided tape, and a transparency film. A patterned agarose membrane is positioned on top of the transparency film. The bacterial cells are cultured on each extruded stage and covered by a coverslip. (b) The cross sectional view of the device (red dotted line). A liquid solution reaches to the agarose membrane through the channel created on the double-sided tape and the fluidic holes on the transparency film. Brown circular dots represent bacteria. (c) Photograph of the actual fabrication process of our microfluidic device.

Patterning in agarose membrane

The key advantage of patterning the extruded stage on the agarose membrane was to isolate bacterial samples from undesirable influences. In addition, the membrane's monolayer design encourages the dispensed bacterial solution to spread out along the flat surface while the agar stage improves sample cohesion at the surface. Meanwhile, the wall of the stage isolates each bacterial colony. The circular micro stage (d= 1.1 mm) on the agarose membrane was fabricated with the help of a PDMS mold. For this purpose, the mask design is drawn in Microsoft Power Point and printed on transparency film using wax printer (Xerox™ ColorQube 8570). Then, unsolidified PDMS mixture is prepared and poured over the mask and cured on hot plate at 80 °C for 5 hours to create the PDMS mold. Later, 2 cm x 2 cm hollow square made of double-sided tape is attached to the glass slide to create the square well. Around 2 mg of high melting temperature agarose powder is melted in 100 mL of deionized water and poured into the square well resulting in a uniform membrane thickness. While the agarose solution is in aqueous state, the prepared PDMS mold is placed on top of the tape to create the pattern. After 5 minutes, the PDMS mold is removed leaving behind extrusions on the surface of the agarose membrane.

Autofocusing system

The hardware of our autofocusing system consists of a microscope camera (QICAM™), workstation, microcontroller (Arduino™), a stepper motor, a motor driver, and a custom gear. The microscope camera is connected to the workstation which enables capturing microscopic images. The microcontroller board control the stepper motor using a motor driver. The custom gear is used to couple the fine focusing knob of the microscope with the shaft of the motor. The microcontroller is programmed to receive serial instructions through USB (universal serial

bus) connection. The autofocusing script is written in Matlab that performs tasks mentioned in Figure 4.3. The program initially captures images at different focal planes.

The task of moving to different focal planes is achieved by sending the instruction to the microcontroller which rotates the stepper motor. Then, the focus *F* measure of these images is calculated using the following formula [24]:

$$F = \sum_{xy} g(x,y)g(x+1,y) - \sum_{xy} g(x,y)g(x+2,y) \quad (4.1)$$

where $g(x,y)$ the grayscale image with M×N pixels. Representative single cell images for focused and unfocused scenarios are shown in 4.3a. The *F* value is maximum when there is sharper contrast between the boundary of the cells and background which is the case for focused images (Figure 4.3a). The maximum *F* value is identified and corresponding number of steps to adjust the focus knob is sent to the microcontroller. Finally, the program captures and saves the focused image. This whole procedure takes approximately two minutes and is repeated at each time-lapsed interval set by the user initially when starting the program. Since a typical time-lapse imaging interval for bacterial cell growth is roughly 20 to 30 minutes, this procedure does not affect the experimental results.

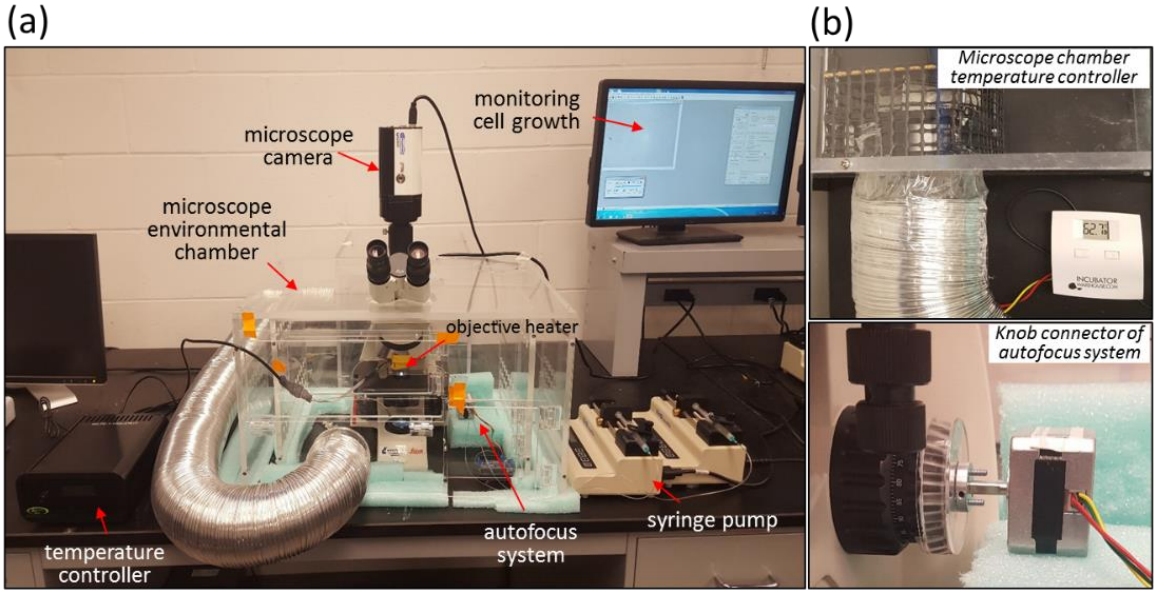

Figure 4.2 Photograph of the environmental chamber for live cell imaging (a) A phase contrast optical microscope is placed inside of the acrylic chamber combined with a microscope camera, temperature controller, objective heater, syringe pump and autofocus system. A user can adjust the focus knob remotely and monitor the bacterial growth on the screen. (b) A heated fan with a temperature controller is installed in a separate chamber, and connected to the microscope environmental chamber where the cells are cultured to prevent rapid changes in ambient temperatures. A stepper motor is attached to the focus knob and rotates it automatically until the image comes into focus.

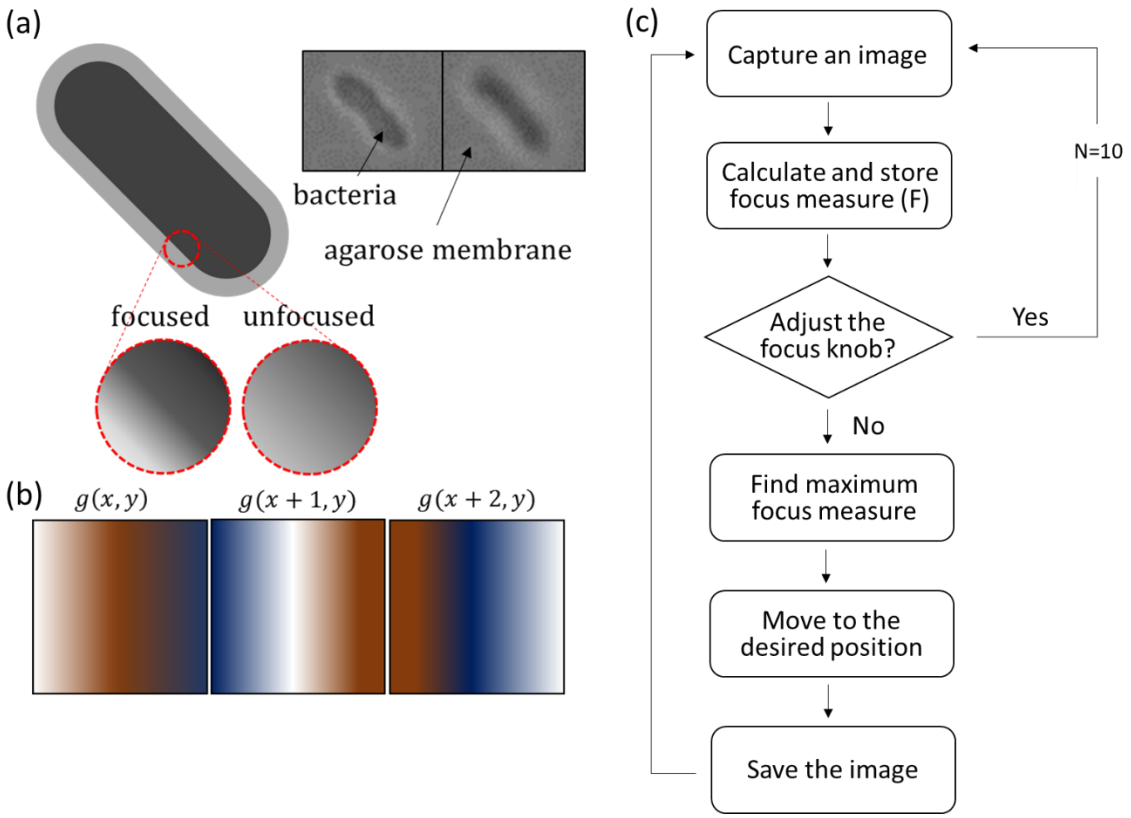

Figure 4.3 The working principle of the autofocusing feature for a microscope. (a) The real and cartoon images of the bacterial cell magnification when seen through a phase contrast microscope at 100x is illustrated. The red circle discerns the difference in the cell wall under focused and unfocused conditions. (b) The principle to calculate the focus measure (F) is shown [24]. Here, $g(x,y)$ represents the intensity of the grayscale image at position (x,y). Similarly $g(x,y)$and $g(x+2,y)$ at $(x+1,y)$ and $(x+2,y)$. The focus measure is calculated by calculating the auto-correlation values of the original $g(x,y)$ and pixel shifted images ($g(x+1,y)$, $g(x+2,y)$) and subtracting them. If an object in an image is in focus, this measure yields a high value when compared to an unfocused object. (c) The flowchart describing the autofocus algorithm. Initially an image is captured from the camera attached to the microscope and its focus measure is calculated. Then the focus knob is incremented by sending commands to a microcontroller. Then another image is captured. This is repeated 10 times and the F values are stored. The position at which the maximum occurs is calculated and the necessary commands are sent to move the focal plane to the desired position. An image is captured at this focal plane and saved. This procedure repeats for the duration of the experiment.

Results and discussion

Cell growth on the microfluidic device

For the proof of concept, the device is utilized to provide a continuous nutrient supply to the cells. 0.1 µL of the bacterial sample (CFU = 1,000) are dispensed on top of the extruded layer using a micro syringe (Hamilton™) and wait for 5-10 minutes for the liquid to be absorbed by the membrane to immobilize the bacterial cells on the surface. After the cells are immobilized on the stage, the agarose membrane is covered by a coverslip. A sealant (SciGene™) is poured on the edge of the coverslip to fix it in place and prevent evaporation. The bacterial growth is monitored and time-lapse images are recorded under the optical microscope with a phase contrast 100x objective lens within the closed chamber. A fan and objective heaters are used to maintain a temperature between 34 – 35 °C for all experiments. A growth medium is continuously provided to the microfluidic channel at a stable flow rate (0.04 mL h^{-1}). A single *E. coli* cell on the agarose membrane multiplied and grew into a large colony over a 10-hour period. The number of cells are counted every 25 minutes (Figure 4.4a). As only fresh liquid solutions are supplied to the inlet and flown continuously to the outlet carrying out the metabolic waste, no observable channel contamination or clogging occurs. The bacterial growth experiments were performed in triplicates and all results are compared statistically.

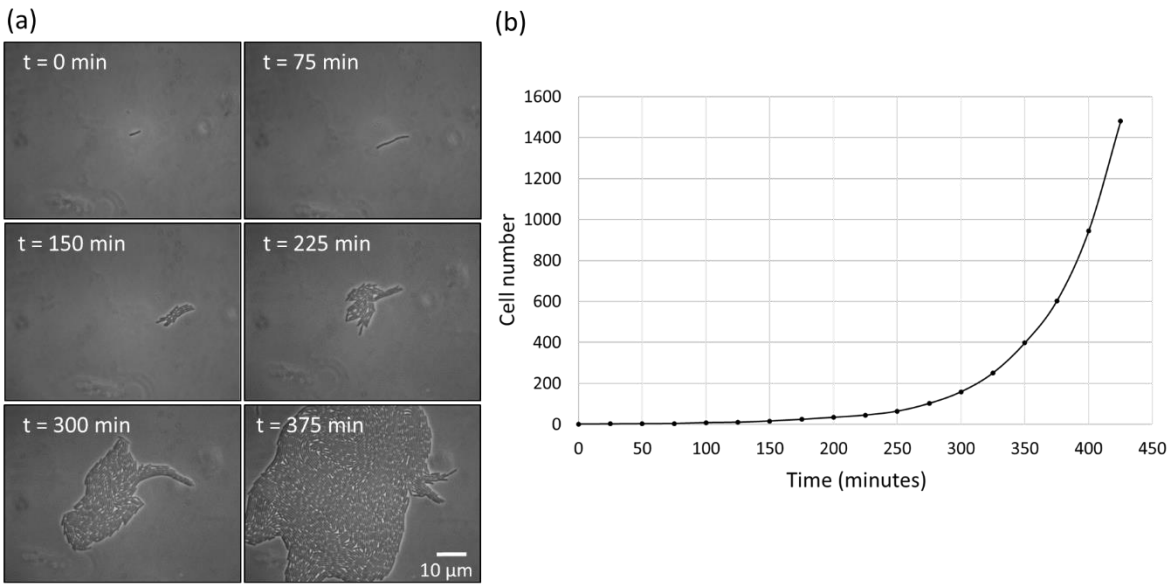

Figure 4.4 *E. coli* growth on-chip (a) Time lapse image of a single cell growing on the microfluidic chip for 8 hours. A growth medium is continuously provided to the agarose membrane through the channel. An autofocus imaging system adjusts the focus knob and takes images regularly. (b) The bacterial growth curve at 35 °C. To count the number of cells easily, they are immobilized on the agarose surface. The experiments are repeated three times and the results are matched.

Morphological dynamics of cell colonies in the presence of antibiotic

Beta-lactam antibiotics have been widely used to kill bacteria which inhibit cell wall biosynthesis [25]. To investigate the physical process of cell lysis after exposure to antibiotics, we utilize our microfluidic device and automated imaging system to provide the antibiotic solution while monitoring the morphological changes of the cells. To provide optimal environmental conditions for bacteria, a growth medium is continuously delivered to the agarose membrane for 3 hours. After the cells grow into a large colony, we test two antibiotic solutions (5 mg/L of Amoxicillin and 5mg/L of Ampicillin) to detect different changes in cell morphology including elongation, bulge formation, and cell lysis. When we switch the input to supply Amoxicillin solution to the bacterial population, the growth has stagnated. As we continue to provide the solution, the cells elongate and eventually explode as can be seen in Figure 4.5a. For the next experiment, a large bacterial colony is treated with Ampicillin

solution. After providing the solution for 4 hours, the bulge formations are observed and eventually burst (Figure 4.5b).

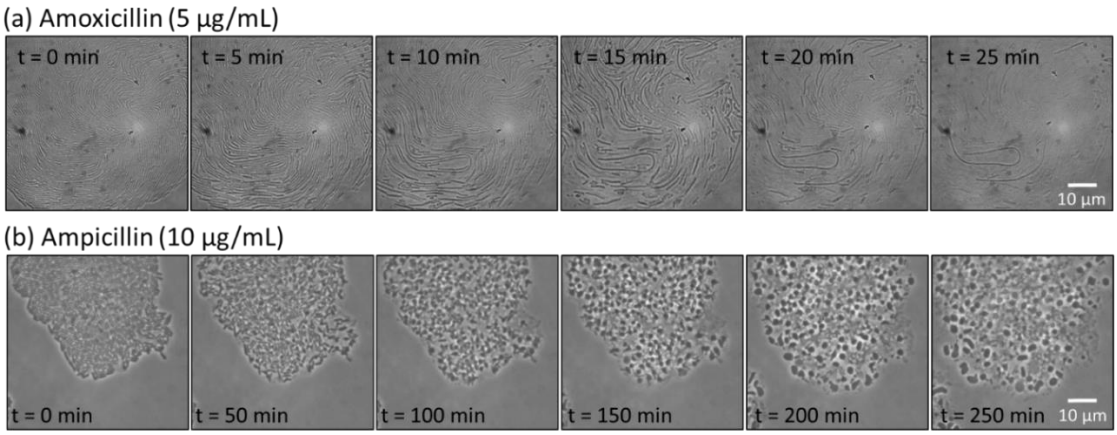

Figure 4.5 Phase contrast image of bacterial colonies exposed to antibiotic solutions. (a) A large bacterial population is exposed to an amoxicillin solution for 2 hours. After about 30 minutes, cell filamentation (elongation with constant width) is observed and explosive cell lysis is detected. (b) An ampicillin solution is applied to the bacterial colony via the microfluidic channel for 2 hours. As a result, a large number of bulge formations and cell explosions are observed.

Gradient concentration experiment

The design of the microfluidic channels was modified to generate a concentration gradient of chemicals to observe cell behavior when exposed to varying concentration of chemicals. To use the microfluidic chip for gradient concentration experiments, liquid solution is needed to diffuse into the agarose membrane slowly. To verify establishment of a chemical gradient on the agarose membrane, a fluorescent solution (30 μM) and LB medium are introduced into the two parallel channels respectively at a flow rate of 0.02 mL h^{-1}. A thin membrane is placed on top of the channel holes and the experiment is performed at 34 – 35 °C. The device is positioned on a heating plate to maintain the temperature and fluorescence images are obtained every hour under a microscope for 12 hours. Each solution diffuses into the porous membrane and a steady concentration gradient is generated. Fluorescence intensities of the images were measured using Image J and plotted in Figure 4.6b.

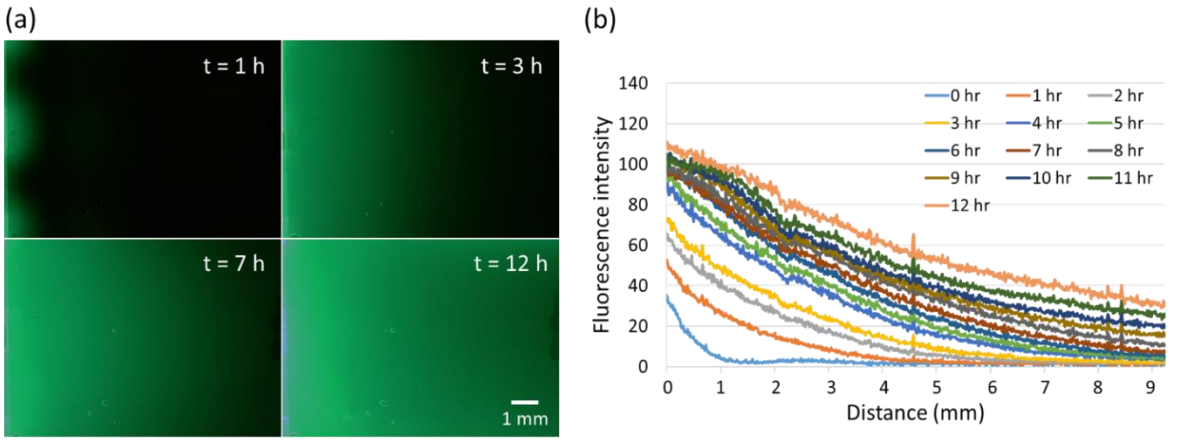

Figure 4.6 Diffusion test on the agarose membrane. (a) The concentration gradient is gradually generated between two parallel microfluidic channels. The fluorescence solution is continuously supplied from the left channel and slowly diffuses into the agarose membrane through the three fluidic holes for 12 hours. (b) The image is captured every hour and the fluorescence intensities over the agarose membrane are measured in Image J. Fluorescence intensity versus the distance from the left channel are plotted.

Antibiotic susceptibility test using microfluidic chip

Ampicillin is considered an effective and safe antibiotic for killing bacteria by inhibiting cell wall synthesis. Since the molecular weight of ampicillin is similar to that of fluorescein, we expect their diffusion rates to be comparable which allows us to back-calculate and estimate the drug concentration in the agarose membrane. LB medium and an ampicillin solution are pumped through two parallel channels containing three fluidic holes spaced 1.2 cm apart from each other. A known concentration of cells (1000 CFU) was dispensed on each extruded stage of the agarose membrane. As shown in Figure 4.7a, any evident phenotypic changes of the bacterial colonies were detected under a 10x microscope objective lens for 5 hours. The inhibition of bacterial growth on three different stages was tracked over 4 hours using oil emersion lens (100x) to access detailed morphological changes in the bacteria. The phenotypic changes of bacteria are continuously monitored at three different sections (top, middle, and bottom) to exploit the device as a sophisticated indicator of the antibiotic concentration. The initial concentration of antibiotic solution was 32 µg/ml and is supplied to

the agarose membrane through the top channel. Figure 4.7b shows that all bacteria on the top stage elongate and explode. On the middle stage (Figure 4.7c), a small portion of the bacterial colony is observed to contain balloon-like cells in the first section. The further away from the top channel (d>5.73 cm) the bacteria are fewer abnormal morphological changes are detected (Figure 7c, d). Using the distance from the top channel and the diffusion rate, a concentration of antibiotic solution is estimated for each section. Three different concentrations of antibiotic solution (32 μg/mL) are used to perform the antibiotic susceptibility test. The elongated and swollen or balloon-like cells are detected when the antibiotic concentration reaches 9.28 μg/mL on average. When the drug concentration is higher than 16.45 μg/mL, cell explosions are observed (Figure 4.7b).

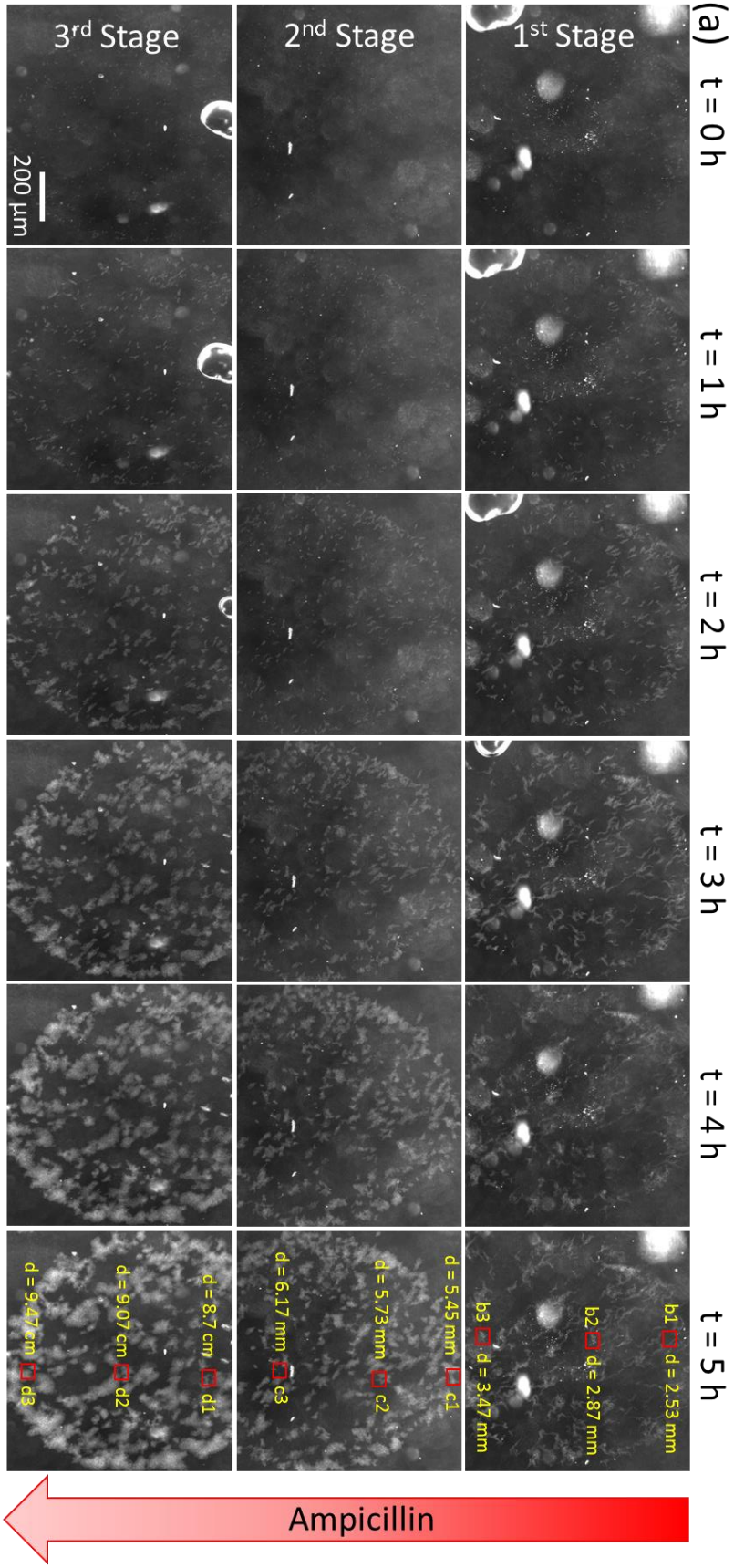

(b) 1st Stage

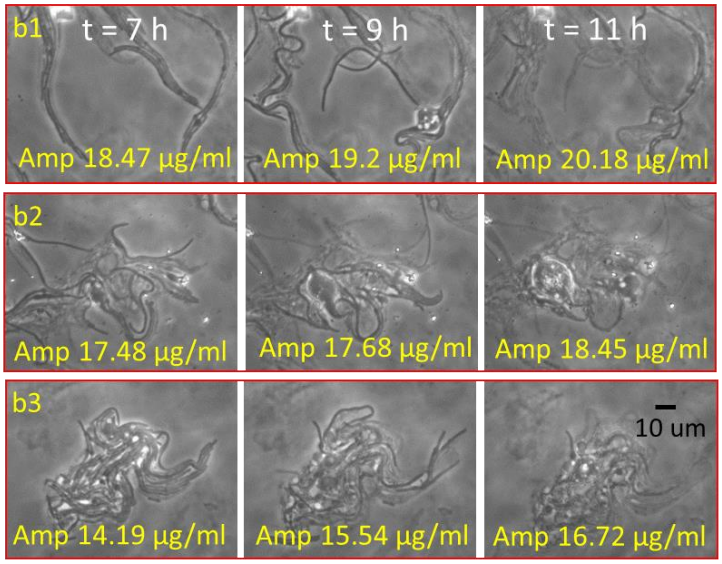

(c) 2nd Stage

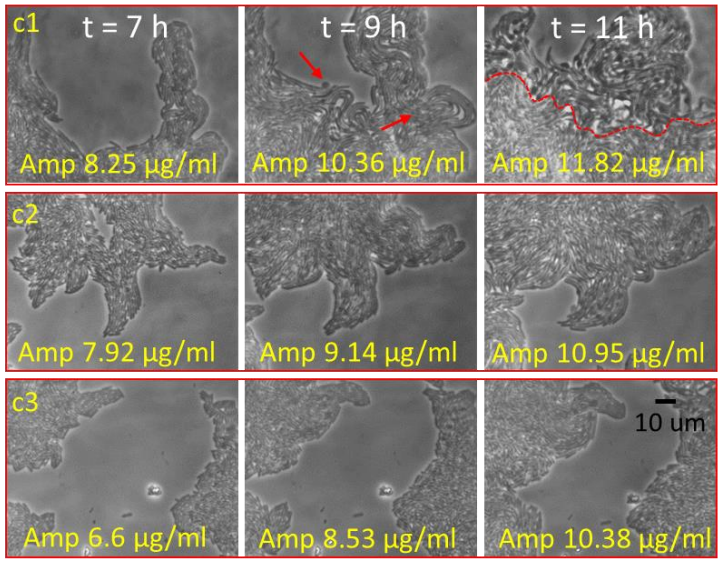

(d) 3rd Stage

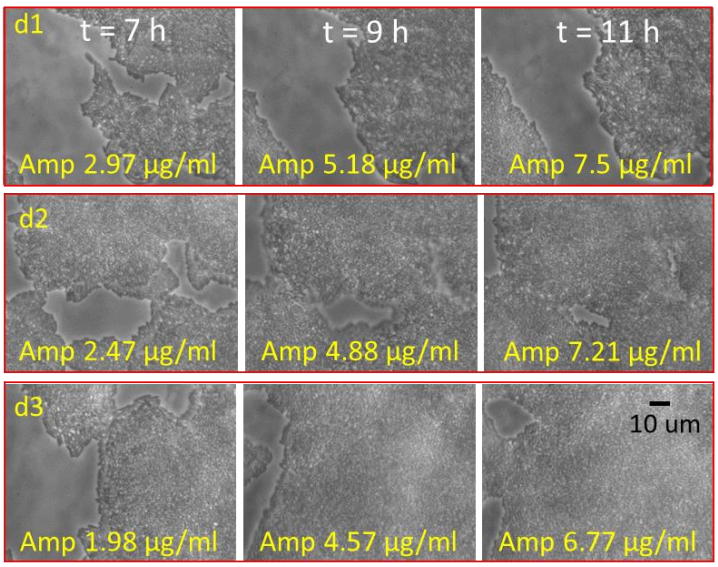

Figure 4.7 The inhibitory effect of the ampicillin on bacteria proliferation is tested on the microfluidic device. The same type of bacteria is cultured on each extruded stage of the agarose membrane. An ampicillin solution (32 μg/mL) is supplied through the top channel and a growth medium is supplied via the bottom channel, creating the ampicillin concentration gradient. (a) After the bacteria is treated with the ampicillin solution for 5 hours, distinct differences in the bacterial growth rate are observed. A 10X objective lens is used to monitor the bacterial growth and an image is captured every hour. (b-d) To obtain the ampicillin concentration related to the abnormal morphological changes in the bacteria, a 100X oil immersion objective lens is used. The elongated and swollen cells are detected when the antibiotic concentration reaches 9.28 μg/mL on average. When the drug concentration is higher than 16.45 μg/mL, cell explosions are observed.

Use of CRISPRi in microfluidics

Clustered Regularly Interspaced Palindromic Repeats (CRISPR) describe a natural bacterial and archaeal adaptive immunity system that can provide cellular defense against invasive DNA or RNA elements as shown in Figure 4.8 [26, 27]. The well characterized Streptococcus pyogenes Type II CRISPR locus is located within the chromosome and composed of repetitive DNA sequences separated by unique DNA fragments obtained from past invasion events, which encode for RNA that can specifically base-pair to its foreign counterpart. Also within the locus are CRISPR associated (Cas) genes including Cas9, an endonuclease capable of targeted dsDNA breaks. During a bacteriophage infection of the cell, the CRISPR system expresses a two-component RNA complex (crRNA and tracrRNA) that guides Cas9 to recognize and destroy the phage DNA [28].

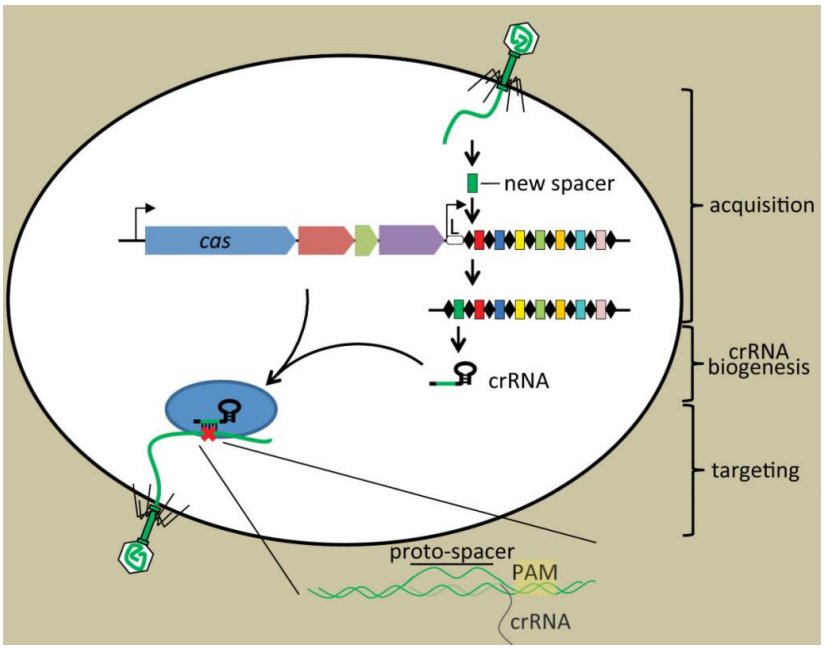

Figure 4.8 The CRISPR-Cas immune system to protect the bacterium against invading viruses. ([26])

In the recent past, researchers have repurposed Type II CRISPR systems for precise, targeted genome editing in eukaryotes and prokaryotes [29]. The system has been simplified, relying only on the Cas9 and guide-RNA components, which were modified to be expressed as a single-guide RNA (sgRNA). The modular design of sgRNA engineering allows for rapid programming by simple cloning of a 20bp fragment complimenting the sequence of choosing. The 20bp target sequence must directly precede an NGG nucleotide Protospacer-adjacent Motif (PAM) site located on the host DNA for effective Cas9 binding and nuclease activity. Upon transformation of plasmids harboring CRISPR-Cas9 elements into the bacterial cell, targeted dsDNA cleavage by the Cas9-guide RNA complex and the addition of a DNA fragment repair template can result in engineered chromosome deletions, additions, and single nucleotide substitutions [30].

CRISPR interference (CRISPRi) is a new variant of CRISPR-Cas9 technology that utilizes a nuclease-defective Cas9 protein (dCas9) for targeted binding of DNA [31]. dCas9

can be used as a programmable repressor in CRISPRi to alter gene expression by physically blocking regulatory elements of genes, preventing transcription by RNA polymerase. We have improved CRISPRi as a tool for gene silencing in bacteria by constructing a series of genetic elements to tightly regulate dCas9 expression from the *E. coli* chromosome. Pairing this technology with microfluidic devices potentially allows for an unprecedented ability to conditionally repress and modulate essential gene expression in bacteria.

For proof of concept, we utilized our gradient microfluidic chip to monitor morphological changes in *E. coli* at the single cell level by targeting the essential cell division gene ftsZ [32] by using CRISPRi. dCas9 is regulated by the inducible tet promoter element, and in the absence of anhydrotetracycline (aTc), constitutively expressed TetR bound to the tet operator sequence tightly controls expression. Introduction of aTc through a microfluidic concentration gradient results in incremental allosteric binding to TetR and subsequent inactivation, allowing for increasing expression of dCas9 along the gradient. When paired with a sgRNA targeting dCas9 to the promoter region of ftsZ, fine-tuned depletion of the FtsZ protein impaired the ability for normal cell division to occur, resulting in an increasing elongated phenotype. 10 μg/mL of aTc solution was supplied to the bottom channel and a growth medium containing ampicillin was provided to the top channel. After the cells were exposed to the different solutions, distinct morphological changes were observed (Figure 4.9). Precise control of cell length and morphology was achieved by varying the levels of aTc inducer within a defined chemical concentration gradient.

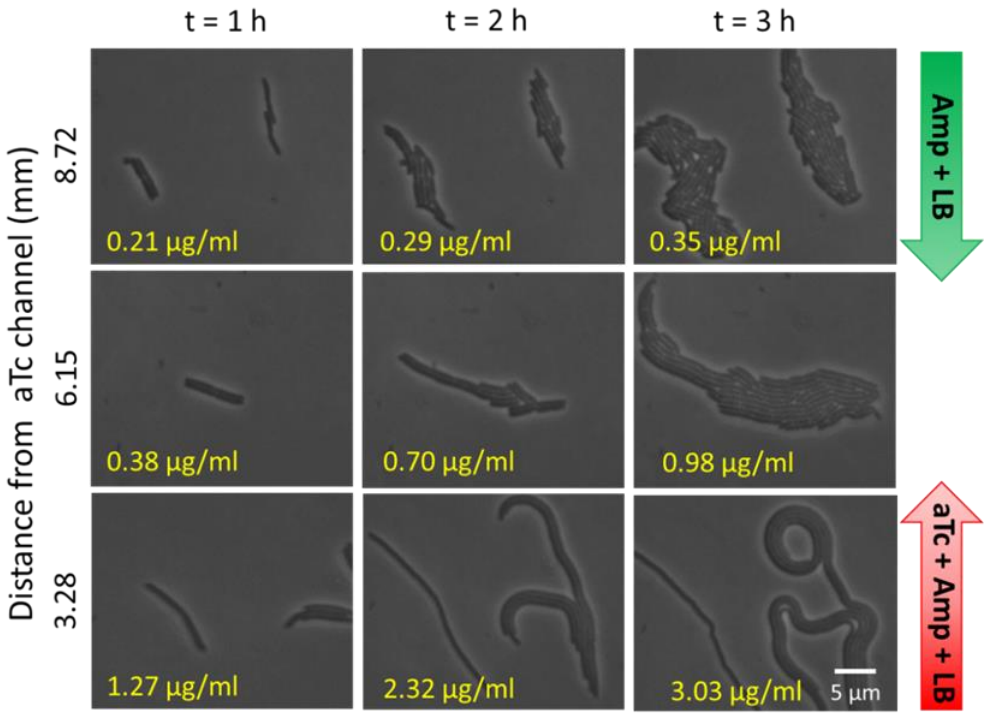

Figure 4.9 Implementation of CRISPRi to visualize morphological changes of the *ftsZ* gene. The gradient microfluidic device is used to conduct single cell level CRISPRi tests. The ampicillin solution (ampicillin and growth medium) is injected to the top channel and the inducer solution (aTc, ampicillin, and growth medium) is applied to the bottom channel. The filamented bacteria is observed when the concentration of aTc was higher than 0.7 µg/mL. As the concentration of the inducer increases (> 1.2 µg/mL), cell divisions are no longer observed.

Conclusion

We demonstrated a double-sided tape based microfluidic device that enables continuous bacterial culturing, gradient establishment, and long-term monitoring of bacteria. Our microfluidic design eliminates the need for complicated fabrication procedures reducing the potential for fabrication related errors. In addition, this microfluidic system is easy to use, inexpensive, and is suitable to both single-cell and population-based studies of bacteria. Multiple solutions can be supplied to the agarose membrane without affecting the quality of recorded images. An auto-focusing system was integrated with the microscope to auto-correct the focusing involved during the imaging process. We also showed the application of the device in growing bacteria, observing morphological dynamics of cells, measuring MIC

values, and controlling gene expression. We believe our system represents a low-cost platform for studying phenotypic and morphologic changes in bacterial cultures for AMR and antibiotic susceptibility studies.

Acknowledgement

We are grateful to Professor Greg Phillips and Nick Bakes for their collaboration on this project over the past 4 years. We are also thankful to Defense Threat Reduction Agency for funding this project and our Program Manager, Dale Taylor for motivating me throughout the course of this project.

Reference

1 H. Leonard, S. Halachmi, N. Ben-Dov, O. Nativ and E. Segal, ACS Nano, 2017, 11, 6167-6177.

2 Z. Liu, N. Banaei and K. Ren, Trends Biotechnol., 2017, 35, 1129-1139.

3 Z. Liu, H. Sun and K. Ren, Chempluschem, 2017, 82, 792-801.

4 W. Sun, R. A. Weingarten, M. Xu, N. Southall, S. Dai, P. Shinn, P. E. Sanderson, P. R. Williamson, K. M. Frank and W. Zheng, Emerg. Microbes Infect., 2016, 5, e116.

5 K. P. Kim, Y. G. Kim, C. H. Choi, H. E. Kim, S. H. Lee, W. S. Chang and C. S. Lee, Lab Chip, 2010, 10, 3296-3299.

6 R. Mohan, A. Mukherjee, S. E. Sevgen, C. Sanpitakseree, J. Lee, C. M. Schroeder and P. J. A. Kenis, Biosens. Bioelectron., 2013, 49, 118-125.

7 C. C. Chung, I. F. Cheng, W. H. Yang and H. C. Chang, Biomicrofluidics, 2011, 5, 021102.

8 J. Dai, M. Hamon and S. Jambovane, Bioengineering, 2016, 3, 25.

9 C. H. Chen, Y. Lu, M. L. Y. Sin, K. E. Mach, D. D. Zhang, V. Gau, J. C. Liao and P. K. Wong, Anal. Chem., 2010, 82, 1012-1019.

10 J. Choi, Y. G. Jung, J. Kim, S. Kim, Y. Jung, H. Na and S. Kwon, Lab Chip, 2013, 13, 280-287.

11 J. R. Moffitt, J. B. Lee and P. Cluzel, Lab Chip, 2012, 12, 1487-1494.

12 Z. Long, E. Nugent, A. Javer, P. Cicuta, B. Sclavi, M. Cosentino Lagomarsino and K. D. Dorfman, Lab Chip, 2013, 13, 947-954.

13 A. Groisman, C. Lobo, H. J. Cho, J. K. Campbell, Y. S. Dufour, A. M. Stevens and A. Levchenko, Nat. Methods, 2005, 2, 685-689.

14 S. Jang, B. Lee, H. H. Jeong, S. H. Jin, S. Jang, S. G. Kim, G. Y. Jung and C. S. Lee, Lab Chip, 2016, 16, 1909-1916.

15 Y. J. Eun, A. S. Utada, M. F. Copeland, S. Takeuchi and D. B. Weibel, ACS Chem. Biol., 2011, 6, 260-266.

16 P. Sun, Y. Liu, J. Sha, Z. Zhang, Q. Tu, P. Chen and J. Wang, Biosens. Bioelectron., 2011, 26, 1993-1999.

17 Y. Li, X. Yan, X. Feng, J. Wang, W. Du, Y. Wang, P. Chen, L. Xiong and B.-F. Liu, Anal. Chem., 2014, 86, 10653-10659.

18 B. Li, Y. Qiu, A. Glidle, D. McIlvenna, Q. Luo, J. Cooper, H. C. Shi and H. Yin, Anal. Chem., 2014, 86, 3131-3137.

19 H. W. Hou, R. P. Bhattacharyya, D. T. Hung and J. Han, Lab Chip, 2015, 15, 2297-2307.

20 M. H. Wu, S. Bin Huang and G. Bin Lee, Lab Chip, 2010, 10, 939-956.

21 I. Peitz and R. Van Leeuwen, Lab Chip, 2010, 10, 2944-2951.

22 T. Kong, R. Brien, Z. Njus, U. Kalwa and S. Pandey, Lab Chip, 2016, 16,1861-1872.

23 T. Kong, S. Flanigan, M. Weinstein, U. Kalwa, C. Legner and S. Pandey, Lab Chip, 2017, 17, 3621-3633.

24 J. H. Price and D. A. Gough, Cytometry, 1994, 16, 283-297.

25 Z. Yao, D. Kahne and R. Kishony, Mol. Cell, 2012, 48, 705-712.

26 R. Barrangou and L. A. Marraffini, Molecular Cell, 2014, 54, 234-244.

27 R. Barrangou, C. Fremaux, H. Deveau, M. Richards, P. Boyaval, S. Moineau, D. A. Romero and P. Horvath, Science, 315, 1709–1712.

28 L. A. Marraffini, Nature, 2015, 526, 55–6.

29 M. Jinek, K. Chylinski, I. Fonfara, M. Hauer, J. A. Doudna and E. Charpentier, Science, 2012, 337, 816-821.

30 Y. Jiang, B. Chen, C. Duan, B. Sun, J. Yang and S. Yang, Microbiol., 2015, 81, 2506-2514.

31 L. S. Qi, M. H. Larson, L. A. Gilbert, J. A. Doudna, J. S. Weissman, A. P. Arkin and W. A. Lim, Cell, 2013, 152, 1173–1183.

32 P. Zhou and C. E. Helmstetter, Journal of Bacteriology, 1994, 176, 6100-6106.

CHAPTER 5.

CONCLUSION

The thesis discussed new methods of liquid handling and transport with related experiments to evaluate performance of each method. The motorized actuation system provided an interesting way to perform droplet manipulations on an open microfluidic setup. We showed the potential of using arrays of discrete droplets for the detection of common biomarkers in biological samples. The all-paper actuator provided a unique method of switching and regulating fluid flow in paper microfluidic devices. These actuators have the potential to improve the versatility of paper microfluidics where multiple sequence of tests can be performed within a single assay. The tape-based microfluidic device with automated imaging provided a valuable means of growing bacterial colonies, imaging at a single cell resolution, and flexibility of interchanging fluids. The microfluidic device has the potential to be used in a range of experiments in microbiology where morphological changes can be tracked in response to antibiotic drugs and inducer chemicals. In summary, the thesis navigates into emerging areas of healthcare and point-of-care diagnostics and highlights the importance of skills acquired in multiple disciplines of engineering and life sciences.